Predictions of atmospheric icing and winter precipitation

Emilie Claussen Iversen

Dissertation for the degree of Philosophiae Doctor (PhD)

Section for Meteorology and Oceanography

Department of Geosciences

University of Oslo

August 2021

Series of dissertations submitted to the
Faculty of Mathematics and Natural Sciences, University of Oslo
No. 2572

ISSN 1501-7710

Print production: Graphics Center, University of Oslo.

:Preface

This synthesis and collection of papers are submitted for the degree of pilosophiae doctor (PhD) in atmospheric physics at the Section for Meteorology and Oceanography (MetOs), Department of Geosciences, University of Oslo. The work has been performed from August 2018 to August 2022, interrupted by a maternity leave. The research has been supervised by Trude Storelvmo (MetOs), Bjørn Egil Nygaard (Kjeller Vindteknikk/Norconsult) and Gregory Thompson (National Center for Atmospheric Research). This work is a part of the Statnett initiated project Icebox, funded by Statnett and the Norwegian Research Council, grant 282403. The thesis consists of an introduction part and the following papers. Summaries of all three papers, including author contributions, are included in Chapter 4 of the thesis part.

Paper I: **Emilie C. Iversen**, Gregory Thompson, Bjørn Egil Nygaard (2021), 'Improvements to melting snow behavior in a bulk microphysics scheme', Atmospheric research, 253, pp. 105471.

Paper II: **Emilie C. Iversen**, Bjørn Egil Nygaard, Øivind Hodnebrog, Maria Sand, Kristian Ingvaldsen (2022), 'Future projections of atmospheric icing in Norway', Cold Region Science and Technology, *in review.*

Paper III: **Emilie C. Iversen,** Øivind Hodnebrog, Lise Seland Graff, Bjørn Egil Nygaard, Trond Iversen (2022), 'Future winter precipitation decrease associated with an extreme North Atlantic warming hole and reduced convection', JGR Atmospheres, *in prep.*

Conference paper publications from the PhD period (not peer reviewed) that are not included in the thesis:

I. **Emilie C. Iversen**, Gregory Thompson, Bjørn Egil Nygaard, and Matteo Lacavalla (2019), 'Improved prediction of wet snow', International Workshop on Atmospheric Icing on Structures (IWAIS), Rekjavik, Iceland, June 23-28.

II. **Emilie C. Iversen**, Bjørn Egil Nygaard, Øivind Hodnebrog, Kristian Ingvaldsen, Maria Sand, Øyvind Welgaard (2022), 'Future changes of atmospheric icing in Norway', International Workshop on Atmospheric Icing on Structures (IWAIS), digital conference, June 19-23.

III. **Emilie C. Iversen**, Bjørn Egil Nygaard, Øivind Hodnebrog, Maria Sand, Kristian Ingvaldsen, Maria Sand (2022), 'Design of overhead lines in a changing climate', Cigre, Paris, France, Aug 29 – Sept 02.

IV. Kristian Ingvaldsen, Bjørn Egil Nygaard, **Emilie C. Iversen** (2019), 'Validation of Modelled In-cloud Ice Accretion on Overhead Power Lines at Exposed High Altitude Sites in Norway', International Workshop on Atmospheric Icing on Structures (IWAIS), Rekjavik, Iceland, June 23-28.

:Acknowledgements

First and foremost, I would like to thank my team of supervisors, Bjørg Egil Nygaard, Greg Thompson and Trude Storelvmo, for guidance and support. Bjørn Egil is both a colleague and a supervisor, and he was the one taking me under his wing when I was starting my first real job as a consultant, and taught me everything I know about atmospheric icing and WRF modeling. I would like to specially thank him for this, and for being a solid rock for me through the ups and downs of a PhD, with his deep and vast knowledge of the subjects, always seeming to have the answer to everything, always with a calm presence, positive mindset and great sense of humor. Thank you to Greg, who so warmly welcomed me to Boulder, to work with him at NCAR. His guidance while working together has been invaluable for my work, and I highly appreciate this as well as the time I got to spend with him and his wonderful family while I was there. Last, but not least, thank you to Trude who has been an authority to seek advice and guidance from, and who has kept me on my track throughout this race, even when things were going a little off-track.

I would also like to thank my co-authors and colleagues Øivind Hodnebrog, Kristian Ingvaldsen and Maria Sand for the bi-weekly scientific and not-so-scientific chats, with fruitful discussions, support and a lot of laughter. And all my colleagues at Kjeller Vindteknikk for their ever-good moods and encouraging words, and particularly Øyvind Byrkjedal for closely following my progress and helping me out in times of crisis. And the research group I've been a part of at UiO, for valuable feedback on my work. Also thank you to the other PhD girls I've shared a room with working at UiO, for useful discussions and sharing of frustrations and victories.

I'm grateful for my friends, who have been patient and supporting, and who have listened to my complaints in rough times, cheered me on, and let me forget all about this PhD for a few moments.

Lastly, I want to thank my family, especially partner Bjørn, son Theo, mum Bente, dad Yngve, 'bonus mum' Christine, and sisters Kaia and Julie, for being my rock-solid support system, I couldn't have done it without you. A special thank you to Bjørn, who has been very patient and supportive through all of this, and to Theo for always lighting up my day and giving me unconditional love.

Oslo, August 10, 2022

Emilie Claussen Iversen

Contents

Part I :Thesis

Chapter 1 :Introduction

1.1 Motivation

Atmospheric icing is a major weather hazard in many mid- to high-latitude regions in the winter, including central and northern Europe, North America, China, and Japan. Icing has been known to cause significant problems for many sectors of society, in particular for power transmission lines, wind turbines, aviation, telecommunication towers and transportation. In Norway, overhead transmission lines are particularly vulnerable to weather hazards as they are transmitting power across complex topography, including elevated mountains and the long and exposed coastline.

Norway has experienced some of the highest recorded ice loads on overhead power lines, with values exceeding 300 kg/m cable (Fikke et al., 2008). There are two types of atmospheric icing that mainly impact the transmission lines in Norway; rime icing due to supercooled liquid cloud droplets that freeze once in contact with the cable; and wet snow icing, which is caused by precipitation in the form of wet snow at temperatures just above freezing that sticks to the cable (Fikke et al., 2008). Experiences of damage on power lines due to atmospheric icing, both in Norway (Kleppe, 1984; Nygaard et al., 2017a) (see Figure 1.1) and internationally (Chang et al., 2007; Li et al., 2008; Makkonen & Wichura, 2010; Sakamoto, 2000), have illustrated the need to take atmospheric icing carefully into account in the planning and design phase, as well as in the operational phase of power line projects. Studies have demonstrated successful usage of the Numerical Weather Prediction (NWP) model, Weather Research and Forecasting (WRF) (Skamarock et al., 2019), with the Thompson microphysics scheme (Thompson et al., 2008; Thompson et al., 2004), in combination with an ice accretion model, in simulating realistic ice loads on power lines (Elíasson et al., 2015; Haldar, 2016; Nygaard et al., 2017a; Nygaard et al., 2011; Nygaard et al., 2013; Thompson et al., 2009). These tools allow for the calculation of extreme ice loads with a high spatial resolution, enabling a detailed line design in variable terrain. There is however a large potential to further develop these objective methods.

Figure 1.1: Photo of collapsed shield wire at 'Ålvikfjellet' 1070 m.a.s.l. in the Hardanger area, Norway, January 9, 2014. (Photo: Ole Berg, Statnett).

A lot of research has been focused on rime icing occurring in high altitude regions in Norway (Nygaard et al., 2017a). However, the majority of the Norwegian transmission grid is located at lower altitudes where the predominant icing type is associated with wet snow. The use of NWP model output to calculate wet snow loads has been increasingly utilized in recent years (Nygaard et al., 2017b). However, experiences from simulations of wet snow icing events using the WRF model and Thompson microphysics scheme in regions of complex terrain (e.g., Norway and Iceland) have shown limitations in the ability to give realistic values in some areas, particularly lee side terrain where wet snow loads have been severely overestimated. Lee side overprediction of precipitation has also been noted by other authors (Colle et al., 2005). This is related to the treatment of melting snow in the microphysical scheme. This limitation needs to be addressed in order to use these tools for calculation of extreme ice loads for the design of the power network in Norway, as well as other countries.

Considering that power transmission lines, and also other ground structures, are designed with an expected lifetime on the order of tens to hundreds of years, climate change impacts on the design parameters should be taken into account. To date, few studies have investigated future changes in atmospheric icing, and particularly rime icing. Ohba and Sugimoto (2020) studied the future change in heavy wet snowfall in Japan using a regional climate model (see Chapter 2.2.3) with 20 km grid spacing, downscaled from six different models from the Coupled Model Intercomparison Project Phase 5 (CMIP5) with a high greenhouse gas emission scenario (see Chapter 2.2.2), with the perspective of changes in atmospheric circulation and weather patterns. Faggian et al. (2021) used the outputs of 11 Euro-CORDEX models (spatial resolution of ~12 km) (Giorgi & Gutowski Jr, 2015) also with a high emission scenario to assess changes in extreme wet snow loads in Italy, and found a general decrease due to increased temperature,

except in the highest Alpine regions. Bulygina et al. (2015) used observations from 958 Russian stations for the period 1977-2013 and found statistically significant decreasing trends in the occurrence of icing. Rögnvaldsson and Ólafsson (2005) studied the change in wet snow icing potential (criteria for temperature, precipitation intensity and wind speed) using a regional climate model and two future scenarios, and found decreases in the lowlands and increases at higher elevations. Another icing type which is not focused on in this study is freezing rain, which is a major weather hazard in for example North America (NA). Jeong et al. (2019) found an increase in future freezing rain ice loads for most of northern NA and decreases for most of southern NA and some northeastern coastal regions, using a 50-member initial-condition ensemble from a regional climate model with a high emission scenario. As atmospheric icing is very regionally dependent, specific climate change studies are needed for all icing prone regions in order to take this into account in structural design planning.

Climate projections in the North Atlantic region generally suffer from great uncertainties. Part of this uncertainty is related to the large natural climate variability of the region, which is difficult to distinguish from an anthropogenic warming signal. The natural variability is to a large extent connected to the variability of dominant atmospheric pressure systems and the jet stream, modulating the position of the Arctic front and the path, frequency, and intensity of storms (Hurrell et al., 2003). Another part of the uncertainty in projections is related to important ocean circulation features and sea surface temperature (SST) gradients they produce (Brayshaw et al., 2008; Gervais et al., 2019; Nakamura et al., 2004). The North Atlantic Warming Hole (NAWH) is an area in the North Atlantic Ocean projected with an SST warming deficit in the future by climate models, linked to a slowdown of the Atlantic Meridional Overturning Circulation (AMOC) (Drijfhout et al., 2012; Keil et al., 2020; Liu et al., 2020) (see Chapter 2.3). This SST anomaly and associated SST gradients affect the intensity, frequency and position of the North Atlantic jet stream and storm tracks, and hence also precipitation (Brayshaw et al., 2008; Gervais et al., 2019, 2020; Hand et al., 2019; Inatsu et al., 2003; Nakamura et al., 2004; Wilson et al., 2009; Woollings et al., 2012). Precipitation is also affected by the altered surface heat fluxes (Gervais et al., 2020; Hand et al., 2019). The NAWH strength, extent and location are projected with a large spread among climate models, where a few models even project a cooling relative to historical conditions. Consequently, AMOC/NAWH constitutes a source of large uncertainty in projections of North Atlantic climate, where projections of clouds and precipitation, and hence also atmospheric icing, are greatly affected.

Future changes in precipitation have substantial consequences for society at a regional and local scale, for example for water storage for hydropower, drinking water, irrigation, industry, and structural design, and winter precipitation is of particular importance due to occurrences of icing and because snowpacks acts as natural reservoirs (Barnett et al., 2008). Therefore, it is essential to improve our understanding of the physical mechanisms of the responses at this scale, to improve and constrain the projections (Trenberth et al., 2003). As stratiform and convective precipitation are produced by different physical mechanisms, these should be investigated separately to better understand the responses. In Norway, or Scandinavia in general, mountains contribute substantially to the distribution and amount of precipitation received through orographic effects, and so this precipitation type should also be considered

separately. The responses in stratiform, convective and orographic precipitation in relation to the NAWH have not been directly addressed in the literature to date.

1.2 Objectives

The overall objective of this thesis is to improve predictions of atmospheric icing and winter precipitation, and project the future occurrence in Norway by the use of numerical weather prediction (NWP) and downscaling of climate models and future scenarios. The improvement is with respect to wet snow and the microphysical scheme representation of melting snow in an NWP model. More specifically, the NWP model is the WRF model with the Thompson microphysics scheme (see Chapter 3.1). This model and microphysics scheme with the implemented changes are further used for downscaling of two global climate models and three future scenarios, to obtain projections of future atmospheric ice loads in Norway (both wet snow and rime ice).

During the progression of this work, a surprising finding emerged; the downscaled projections of winter precipitation differed greatly between our chosen climate models, with generally opposite signs of change, hypothesized to be connected to their differing projections of the NAWH. Specifically, the Community Earth System Model version 2 (CESM2) (Danabasoglu et al., 2020), which projects one of the strongest and most spatially extensive NAWHs among current climate models, showed relatively large decreases in winter total precipitation, in contrast to the general scientific consensus of 'wet regions get wetter' (Held & Soden, 2006; Ranasinghe et al., 2021).

Another objective is therefore to investigate and understand the physical mechanisms behind this winter precipitation response, which has implications for the future wet snow load projections. In order to fully understand these mechanisms, stratiform, convective and orographic precipitation are investigated separately.

The objectives can be divided into three specific objectives which each are met in a paper:

Paper I

This paper presents the improvements made to the Thompson microphysics scheme (part of the WRF model) with respect to melting snow behavior. This includes validations against observations from the Olympic Mountain Experiment (OLYMPEX) (Houze et al., 2017) in Washington state, as well as a demonstration of the effects of the implemented changes on the spatial precipitation distribution (snow and rain) across the Olympic Mountain. The improved scheme will contribute to improved precipitation forecasts and predictions of wet snow icing.

Paper II

To project the future occurrence of atmospheric icing in Norway, two climate models and three future scenarios are dynamically downscaled using the WRF model with the microphysical improvements presented in Paper I. The chosen models are CESM2 and the high resolution

version of the Max Plank Institute for Meteorology Earth System Model (MPI-ESM1-2-HR) (Müller et al., 2018). Maps of future projected 10-year return period ice loads for wet snow and rime ice are presented, for three different future time periods (up to 2100).

Paper III

The objective of this paper is to investigate the physical mechanisms explaining the winter precipitation decrease projected by the CESM2 model, which contrasts sharply to the precipitation projections of the MPI-ESM1-2-HR model in Paper II, as well as the general scientific consensus ('wet gets wetter'). The downscaled data presented in Paper II is used, and the response is investigated separately for stratiform, convective and orographic precipitation. Connections between the strong NAWH and the different precipitation types are highlighted, which have not previously been brought attention to in the literature.

The work of this thesis is part of the R&D project, Icebox, initiated and partly funded by the Norwegian transmission grid operator, Statnett, also partly funded by the Norwegian Research Council. The main objective of Icebox is to develop a toolbox for the prediction, projection, monitoring and removal of atmospheric ice loads on overhead power lines.

Chapter 2 :Background

2.1 Numerical Weather Prediction

The Norwegian Vilhelm Bjerknes is often called the father of modern numerical weather prediction (NWP), because already in 1904 he suggested that predicting the state of the atmosphere is a fundamentally deterministic initial-value problem of mathematical physics (Bauer et al., 2015; Bjerknes, 1904). In NWP, equations describing the behavior of the atmosphere are numerically solved to forecast the weather (Coiffier, 2011). The equations are the governing partial differential equations of fluid motion, including conservation of momentum, mass and energy, and the ideal gas law. NWP models can be either hydrostatic or nonhydrostatic. In hydrostatic models, the vertical momentum equation is replaced by the hydrostatic approximation, implying that vertically propagating waves cannot form, which is a good approximation for synoptic scale motion, but not for circulation occurring on the mesoscale. For high-resolution modeling, nonhydrostatic models should be utilized, which captures circulation features such as mountain gravity waves and cumulus convection. Traditional NWP discretizes the equations by dividing the atmosphere into grid boxes, defined by a horizontal grid and a number of vertical levels (see Figure 2.1), so that atmospheric quantities are represented by their grid box means. For NWP this is most often performed for a limited area model domain (also referred to as Limited Area Model). The higher the resolution of the model grid (more grid boxes), the higher the computational cost of running the model.

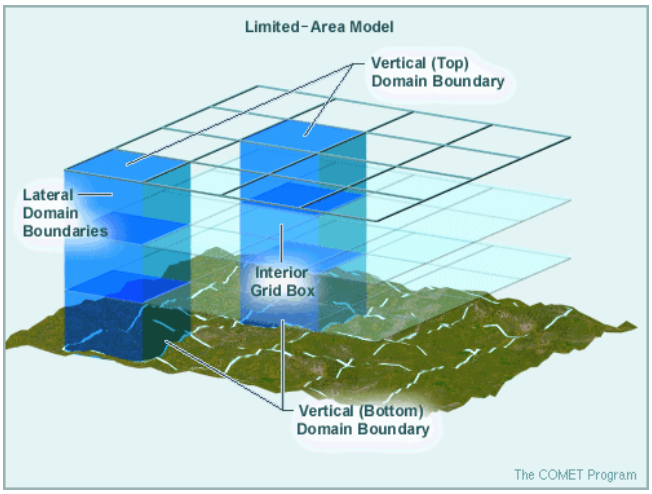

Figure 2.1: An illustration of an NWP Limited Area Model domain showing how it is discretized into a horizontal grid and vertical layers (which near the surface are terrain following, but become more even with height). Domain boundaries are highlighted. (Courtesy of the UCAR COMET program).

Important physical processes affecting the evolution of the atmosphere exist on smaller scales than represented by the model grid, typically referred to as sub-grid scale processes. As such, these processes must be parameterized. A process might also be too complex and hence computationally costly to be handled directly, and so requires parameterization. These additional computations form the model physics, and are introduced into the numerical processing of the equations of fluid motion, which forms the model dynamics (the dynamical core) (Coiffier, 2011). Physical parameterizations include convection, microphysics, boundary layer, radiation and land-surface processes (Warner, 2010b). Realistic representations of these processes are crucial for the prediction of virtually all of the model's prognostic variables.

The predictions start from initial values (initial conditions) and are forced on the boundaries of the grid (boundary conditions). Such conditions typically stem from reanalysis data (Hersbach et al., 2018) or other operational analysis created by data assimilation methods. Data assimilation is a method that use numerical models to assimilate information from the global observing system, including satellite instruments, weather stations, ships, buoys, and other components (Ghil & Malanotte-Rizzoli, 1991). This creates a dynamically consistent, observationally based set of data.

2.1.1 Microphysics parameterization

Microphysics parameterization represents processes involving hydrometeors in the atmosphere on scales of microns to millimeters (Warner, 2010b). The hydrometeors are cloud droplets, cloud ice, snow, graupel, hail and rain, all of which are important for the formation and fallout of precipitation. The processes include condensation, evaporation, melting, freezing, deposition (snow or ice growing by vapor deposition), accretion or riming (snow or ice collecting cloud water), aggregation (collision and coalescence of snowflakes and ice crystals) and collision-coalescence (of cloud or rain drops) (Pruppacher & Klett, 1997). A key aspect of so-called bulk microphysical parameterizations used in most NWP models is the representation of a hydrometeor's size distribution by an analytical function, e.g., exponential (Kessler, 1969) or gamma (Walko et al., 1995) distribution, and the use of their moments to predict their evolution. The first microphysics schemes were single moment, in which only the hydrometeor mixing ratios are predicted. As computational power has increased, double-moment schemes, predicting both mixing ratio and number concentration of the hydrometeors, have been increasingly utilized. Some schemes are also partially double-moment, where only a few of the represented hydrometeors are double-moment, to save computational time (Thompson et al., 2008). Triple moment schemes also include radar reflectivity as a prognostic variable. Schemes also vary in complexity with the number of hydrometeors predicted and their associated interactions. Treatment of the fallout of hydrometeors as precipitation reaching the ground is termed sedimentation, and is dependent on the hydrometeor terminal fall speed. Examples of widely used microphysical schemes for NWP are Milbrandt and Yau (2005), Morrison and Milbrandt (2015), Thompson et al. (2008).

2.1.2 Convective parameterization

Precipitation from convective clouds is the dominant form of precipitation in many regions of the world, particularly the tropics, and contributes to a large degree to precipitation extreme events. In the mid-latitudes, convection and associated precipitation is also common in association with cyclones when cold air is advected over warmer surfaces with the passage of cyclone frontal boundaries (Houze Jr., 1993; Kuettner, 1959), which is particularly prominent in winter over a relatively warm ocean surface. Convective precipitation is a key component of the hydrological cycle, and is important also for tropospheric vertical mixing and radiative forcing (Prein et al., 2015).

As convective processes occur on the sub-grid scale, the goal of a convective parameterization is to predict the collective effects of convective clouds within a grid box, as a function of the grid scale conditions (Stensrud, 2007). The grid scale processes force the convective scheme through low-level convergence and destabilization (convective triggers, which vary in definition between schemes), and the sub-grid scale parameterized convective processes feed back to the grid scale through latent heating effects (Warner, 2010b). The convection scheme produces grid box average values of convective precipitation, which typically end up as a separate model output in addition to all precipitation.

Moist convection is said to be ‘permitted’ on model grid scales less than 5 km. When running a model with a grid resolution larger than 10 km, normal practice is to parameterize convection to incorporate the important sub-grid scale processes. The scale range between about 4 – 10 km is often called the ‘convective grey zone’, as clouds and the vertical turnover circulation are only partly resolved, and it depends on the application and user whether convective parameterization is turned on or off.

Convective parameterizations are typically associated with large errors (Déqué et al., 2007; Hohenegger et al., 2008; Kendon et al., 2020; Li et al., 2019; Tang et al., 2021; Tomassini et al., 2017; Trenberth et al., 2003; Wilcox & Donner, 2007), although improvements are continuously being made. Common errors include misrepresentation of the diurnal cycle, overestimation of low-precipitation event frequency, underestimation of hourly precipitation intensities (Prein et al., 2015), and inability to advect convective elements, for example in cases of ocean triggered convection cells advected over land (Kendon et al., 2020).

2.2 Climate modeling

'The term climate modeling refers to the use of a model to define the state of Earth's physical system on time scales of seasons to centuries' (Warner, 2010a).

2.2.1 Global climate projection

Global climate models function very much like NWP models. However, whereas NWP is mostly used for high resolution, limited-area, short-term weather prediction (days to a few weeks), global climate models are used for lower resolution, global scale, long-range climate projection (years to centuries). However, as weather science and high-performance computing are evolving, model resolutions are becoming increasingly high also at the global scale, and this is the future for both NWP and climate modelling (Bauer et al., 2015).

For NWP, the sea-surface temperature, vegetation, permafrost, glaciers, sea ice and emissions can be specified as initial and boundary conditions from observational data, and for short-term forecasting assumed to be invariant during the model integration (Warner, 2010a). Global climate models are integrated for long, continuous time periods where the weather is freely evolving, without any forcing from meteorological input conditions. Hence, they must also include many additional physical processes related to the ocean, land- and sea ice, and the land surface, as well as emissions and aerosols. All of these processes, in addition to the atmospheric processes, must interact as they are all part of the complex global climate system. This interaction between different components of the climate system is referred to as coupling.

For the application of climate change modeling, normal practice is to simulate a recent and a future climate period, in order to investigate changes. Both periods are simulated with freely evolving weather, as one must when simulating global future weather and climate, hence the term used is climate 'projection' and not 'prediction'. Consequently, the past period weather cannot be compared to the observed historical weather, but the idea is that the average weather – namely the climate – will be realistically represented. Normal practice is also to firstly evaluate and validate the model performance of simulated past or present climate and highlight potential biases and errors.

2.2.2 CMIP6 and Scenarios

The Coupled Model Intercomparison Project's (CMIP) main objective is to improve our understanding of the climate system and climate changes, by coordinating the design and distribution of global climate model simulations (Eyring et al., 2016). An important goal of CMIP is to make these simulation outputs publicly available in a standardized format. The CMIP began its work 20 years ago, and has since undergone five phases – now in its present

phase six, involving a large number of international modelling groups and experiments. The climate models involved are updated and improved with each phase. One common experiment performed identically by all modelling groups is the historical simulation (1850 to present). These simulations include observationally based, evolving, externally imposed forcings such as solar variability, volcanic aerosols, and changes in atmospheric composition (emissions and aerosols) caused by human activities. Another set of experiments performed are within the so-called ScenarioMIP (O'Neill et al., 2016). Here multi-model climate projections based on a range of scenarios for future emissions and land use changes are made available, and provide the primary basis for impacts, adaptation and vulnerability studies. The design consists of eight different 21st century scenarios with spatially explicit emissions and land use changes generated with integrated assessment models, based on alternative future societal development pathways – 'the Shared Socioeconomic Pathways' (SSPs). The future scenarios (SSPs) given as CO_2 concentrations are shown in Figure 2.2.

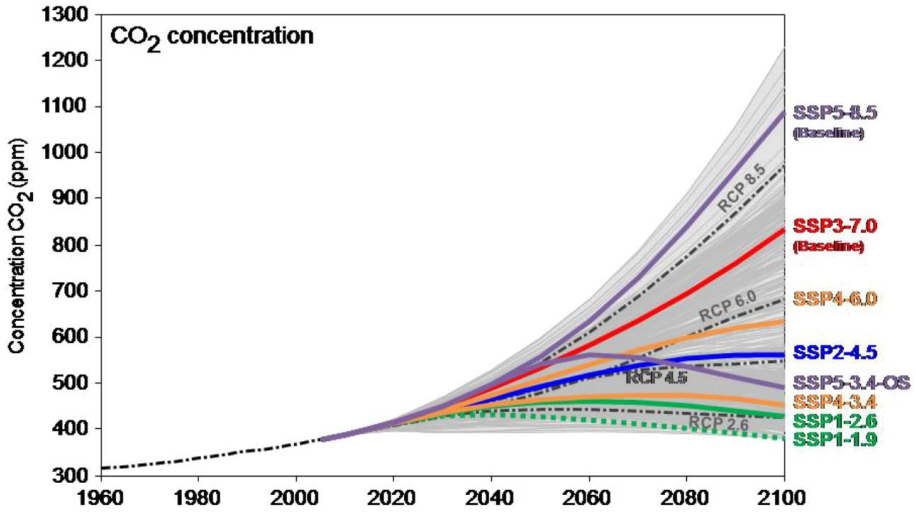

Figure 2.2: CO_2 concentrations for the 21st century scenarios (the Shared Socioeconomic Pathways, SSPs) in the ScenarioMIP design, from Riahi and al. (2017), as presented in O'Neill et al. (2016). The RCP lines are the Representative Concentration Pathways used in CMIP5. Gray areas represent the range of scenarios in the scenarios database for the Intergovernmental Panel on Climate Change Fifth Assessment Report (IPCC AR5).

2.2.3 Regional climate modeling and downscaling

The grid resolution of present state global climate models is relatively coarse, on the order of a hundred kilometers. This implies that regional climatic variables are homogeneous for large areas, where in reality there is great regional variability. Topography exerts a strong impact on climate, especially in regions with complex orography, which is poorly resolved and significantly smoothed in the global models. We also know that climate change can be highly regionally dependent, with relevant change processes occurring on scales smaller than that of global models. This is especially true for extremes (Warner, 2010a). For these reasons, regional climate modeling offers the opportunity for more detailed predictions and to better understand

climate change processes down to the regional level. This is particularly valid for precipitation, which is one of the most difficult variables to simulate with global climate models due to small scale phenomena, which have very large impacts (e.g., extremes, convective systems, orographic precipitation) (Gutowski Jr et al., 2016).

Regional climate modeling utilizes limited area models, also called regional climate models (RCMs), which basically are NWP models run for climatic timescales. A frequently used methodology is dynamical downscaling, where the regional model is used to downscale coarser scale global climate model simulations to a smaller scale, by using this data as initial and lateral boundary conditions. In this way the synoptic scale weather systems of the global climate model are modulated by local scale forcing through physically consistent processes. Biases in the global model will however be transferred to the regional model.

The CMIP6 has its own MIP on downscaling, the Coordinated Regional Climate Downscaling Experiment (CORDEX) (Gutowski Jr et al., 2016). Regional climate downscaling is also performed independently of the CMIP by various international modeling groups (e.g., ENSEMBLES (Hewitt & Griggs, 2004), NARCCAP (Mearns et al., 2009), NARCliM (Evans et al., 2014), UKCP09 (Murphy et al., 2010)), with increasing focus on higher resolution down to the convection-permitting scale (~1 – 4 km) (Ban et al., 2014; Fosser et al., 2015; Kendon et al., 2019; Leutwyler et al., 2016; Liu et al., 2017). On these scales a convective parameterization is typically not applied, and the convective transport is explicitly represented by the dynamics and convective cloud processes by the microphysical scheme of the regional model, with indications of improvement over convective parameterizations (Ban et al., 2021; Hohenegger et al., 2008; Kendon et al., 2020; Kendon et al., 2012; Lind et al., 2020; Meredith et al., 2015; Prein et al., 2020; Rasmussen et al., 2011). Due to the high computational cost of running such models at climate time scales, such simulation output is still relatively scarce.

2.3 North Atlantic climate variability, interactions and change

In this subchapter a brief introduction to North Atlantic climate variability is given, with respect to the aspects and interactions of the climate system relevant for the work of this thesis, and with a focus on northern Europe. Projected future changes to North Atlantic climate with these aspects and interactions in focus are also briefly discussed.

2.3.1 The North Atlantic Oscillation

The North Atlantic Oscillation (NAO) is the leading mode of atmospheric variability in the North Atlantic region (Hurrell et al., 2003). It represents the variability of the relative strengths of the dominant atmospheric pressure systems in the region, namely the Icelandic low and Azores high pressure systems. This pressure difference modulates the path, frequency and intensity of extratropical cyclones forming over The North Atlantic Ocean. The organized bands of extratropical cyclones are referred to as 'storm tracks' (Hoskins & Valdes, 1990), and the correlation between the NAO and the storm tracks is strong. When there is a large pressure difference between the Icelandic low and Azores high (positive NAO), these systems are strong, generating relatively intense and frequent cyclones, which typically take on a track directed towards central and northern Europe (see Figure 2.3 left). This is correlated with more clouds, precipitation and wind, and mild temperatures in this region (Chiacchio & Wild, 2010; Hurrell et al., 2003; Iversen & Burningham, 2015; Uvo, 2003; Wibig, 1999). When the pressure difference is small (negative NAO), reflecting weaker pressure systems, the cyclones tend to be weaker and less frequent, and the storm tracks are typically positioned further south, leaving northern Europe north of the polar front with dry and cold weather (see Figure 2.3 right). As the pressure systems are strongest and most active in winter, the NAO is most prominent this time of year.

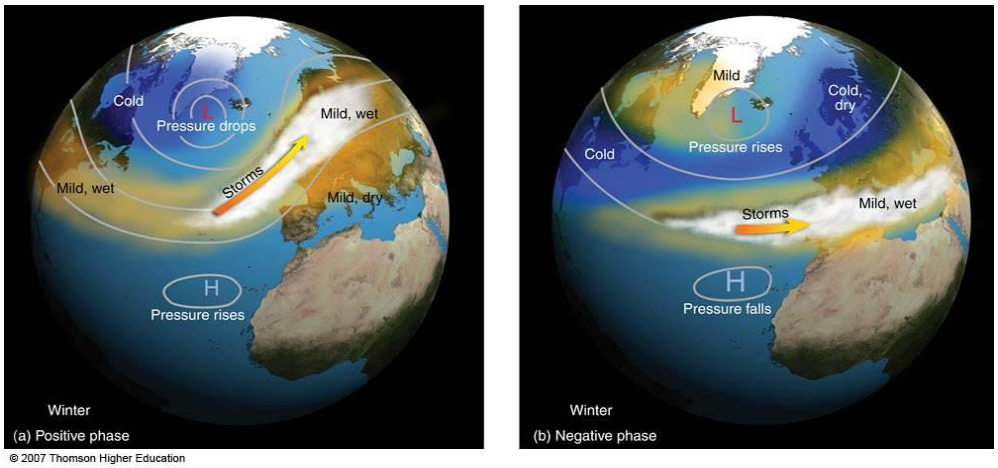

Figure 2.3: Schematic of the positive (left) and negative (right) phase of the North Atlantic Oscillation (NAO) and associated changes in storm tracks and winter weather conditions.

2.3.2 The jet stream

One cannot talk about the NAO and the storm tracks without mentioning the jet stream. The jet stream is a stream of strong westerly winds near the altitude of the tropopause, located at the boundary between warm tropical air masses to the south and cold polar air masses to the north. The polar jet in the northern hemisphere is driven by this sharp meridional temperature gradient at the polar front. This so-called 'baroclinic' region of large horizontal temperature differences leads to the growth of cyclones (Charney, 1947; Eady, 1949), the paths of which are steered by the jet stream, but which also reinforce the jet through wave–mean flow interaction (Hall et al., 2015; Hoskins et al., 1983). As the equator to pole temperature gradient is strongest in winter, the jet stream and storm tracks are strongest and most active in this season. The variability of the jet stream is strongly correlated with the variability of the NAO (Vallis & Gerber, 2008). During a positive (negative) NAO the jet is stronger (weaker) and shifts poleward (equatorward) (Benedict et al., 2004).

2.3.3 Marine cold air outbreaks

Marine cold air outbreaks (MCAOs) in the North Atlantic are associated with the advection of very cold air originating from polar ice-covered areas, over a relatively warm ocean surface (Kolstad et al., 2009). This causes destabilization of overlying airmasses, large fluxes of latent heat from the ocean to the atmosphere, and consequently strong convection (Brümmer, 1997, 1999; Papritz & Spengler, 2017). MCAOs may cause severe weather such as polar lows (Bromwich, 2004; Mansfield, 1974) and strong surface winds (Kolstad, 2017), and the large atmosphere-ocean heat exchange impacts the formation of deep-water in the Nordic Seas (Buckley & Marshall, 2016; Isachsen et al., 2013). Atmospheric temperature variability is governing the seasonal and the inter-annual variability of MCAOs (Kolstad et al., 2009). MCAOs in the Nordic Seas is closely linked to the path of cyclones (Papritz & Grams, 2018), typically formed in the cold, dry Arctic air behind the cold front.

2.3.4 The Atlantic Meridional Overturning Circulation

The Atlantic Meridional Overturning Circulation (AMOC) is a major system of ocean currents (Schmittner et al., 2007). The Gulf Stream and North Atlantic current transport warm water from the tropics into the North Atlantic Ocean. The cold and salt water at its northern edges in the Nordic Seas is dense and sinks deep into the ocean, before being transported southward. In this way the current system acts as an overturning conveyor belt to redistribute temperature in the ocean. Consequently, sea surface temperature (SST) and climate variability in the Atlantic sector are closely related to fluctuations in the AMOC (Rahmstorf, 1995), typically occurring on multidecadal to centennial timescales. The AMOC is very sensitive to small fluctuations in freshwater fluxes, which over the historic record has caused abrupt shifts in climate due to

transitions between different AMOC states. Global warming has raised the concern that increased melting of the Greenland ice sheet will lead to a slowdown of the overturning circulation with potentially severe consequences for global climate (Caesar et al., 2018). Research on the AMOC is therefore a very active field (Fox-Kemper et al., 2021).

2.3.5 Climate changes and the North Atlantic Warming Hole

Climate projections do indeed confirm a weakening of the AMOC with global warming due to increased influx of heat and freshwater (Rahmstorf, 1995; Rahmstorf et al., 2015; Stocker & Wright, 1991). Such a weakening will cause cooling of SSTs in the subpolar North Atlantic due to reduced heat transport, which is supported by observations (Caesar et al., 2018; Rahmstorf et al., 2015), and has been termed 'the North Atlantic warming hole' (NAWH). The observations are however based on a short record (since 2004) and consequently cannot confirm whether this is a long-term negative trend or a recovery from earlier strengthening of the AMOC (Jackson et al., 2016), and hence this is the big question to be answered.

In future projections, the SST cold anomalies of the NAWH cause an increase in the meridional surface temperature gradient, as global warming simultaneously causes increased temperatures in the tropics. This leads to increased baroclinicity, and the potential for enhanced storm activity over the North Atlantic and Europe (Brayshaw et al., 2008; Gervais et al., 2019; Hand et al., 2019; Inatsu et al., 2003; Nakamura et al., 2004; Wilson et al., 2009; Woollings et al., 2012). Changes in the jet stream and storm tracks are sensitive to the location of the SST gradient relative to the mean jet position, where a poleward (equatorward) shift is produced when SST gradients are located poleward (equatorward) of the subtropical jet. Consequently, the AMOC strength and NAWH strength, extent and location in climate models play a crucial role in their projections of future North Atlantic climate, which to date shows a significant spread among climate models. This is an active field of research, and far from all connections and implications are fully understood.

2.4 Precipitation

Precipitation and its part in the hydrological cycle, its mechanisms of generation, spatial and temporal variability, and future change is a vast and comprehensive field of research, ranging from the microscale to the global scale. This subchapter does only aim at describing the aspects relevant for the work of this thesis.

2.4.1 Precipitation generation mechanisms

Precipitation can be generated by two distinctly different physical mechanisms; stratiform and convective. Orography might enhance this precipitation, or act to generate precipitation from impinging clouds, which is then called orographic precipitation. Their different mechanisms of generation are here described, and the resulting precipitation is sometimes referred to as 'precipitation types' through this thesis.

Stratiform precipitation

Stratiform precipitation is generated within nimbostratus clouds, which are produced by nearly thermodynamically stable air and widespread vertical air motions, typical of the warm conveyor belt of the warm front of a low-pressure system (Browning, 1990). Stratiform precipitation is generally mostly associated with these widespread systems (Houze Jr., 1981). Most stratiform precipitation falls from nimbostratus clouds that reach far above the melting level and contain ice particles aloft, and particle growth for precipitation formation depends on the sedimentation of the ice particles. Houze (2014) defines precipitation to be stratiform if the mean vertical velocity of the air averaged over a vertical volume ($\overline{w}$) is much lower than the typical fall velocity of ice crystals and snow (~1 – 3 m/s) (v_{ice}), so that their downward motion through the cloud is not disrupted:

$$0 < |\overline{w}| \ll v_{ice}$$

$\overline{w}$ might still be overall upward, which is typical for an active stratiform region. The upward motion maintains supersaturation with respect to ice, so that ice particles grow by vapor deposition, while drifting downwards due to their weight. A schematic of the typical vertical structure of a stratiform cloud and its precipitation process is shown in Figure 2.4 (a). A horizontally oriented melting layer is typically present, observed as a band of enhanced reflectivity seen in radar echos called the 'bright band' (Fabry & Zawadzki, 1995). Within about 1 km above the melting layer aggregation is frequent. Aggregation is when snow crystals collide and form larger, irregularly shaped snowflakes, which melt into larger raindrops.

Convective precipitation

Convective precipitation is generated within cumulus and cumulonimbus clouds which display a vertically oriented structure as opposed to the more horizontally uniform stratiform clouds (Figure 2.4 b). Convective precipitation is produced within strong, vertical updrafts caused by

atmospheric static instability. Static instability may for example be caused by heating of air from a warmer ground or ocean surface beneath, causing this surface-layer air to be warmer than the air above. In the convective updrafts, ice is carried upward, growing by accretion of liquid cloud droplets (riming), until they are heavy enough to fall downward. With the definition of Houze (2014), precipitation is convective if $\overline{w}$ exceeds v_{ice}:

$$\overline{w} > v_{ice}$$

The updrafts are strong enough to support condensation of large amounts of liquid water which is available for the growth by accretion of the suspended particles. The updrafts are less than 2 km in width and produce well defined vertically structured clouds.

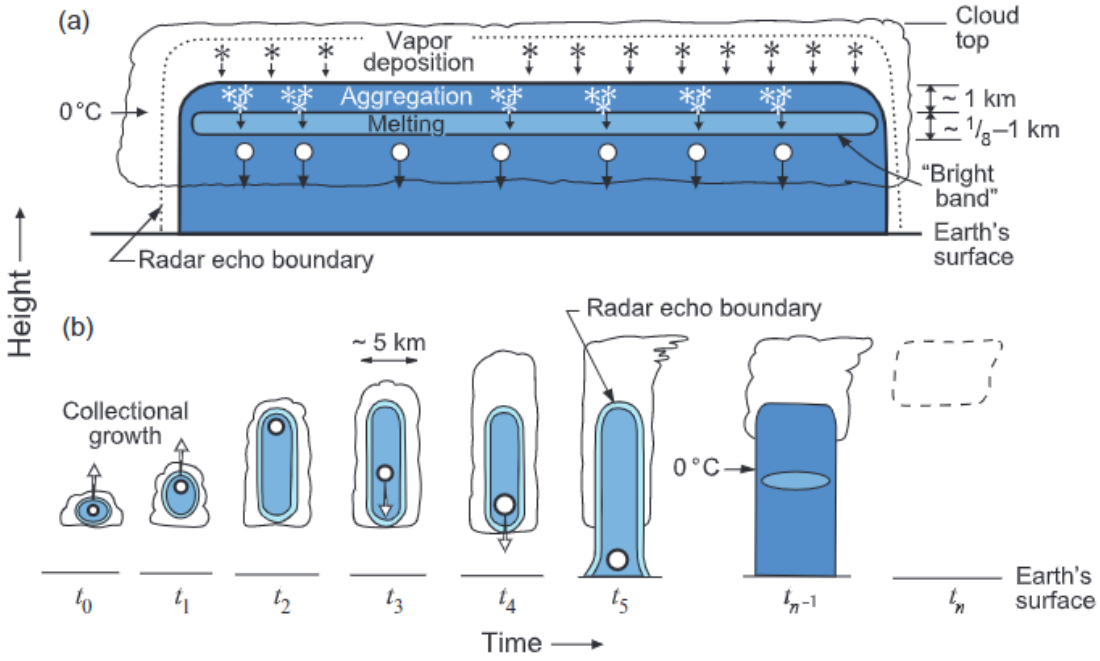

Figure 2.4: Characteristics of stratiform (a) and convective (b) precipitation. From Houze (2014).

Orographic precipitation

Orographic precipitation is associated with the flow over mountains, as the orographic lifting creates air saturation, clouds and precipitation. The mechanisms may act to initiate the generation of precipitation or act to intensify the precipitation in incoming cloud systems (orographic precipitation enhancement), where the latter occurs most frequently. In statically stable flows, the airflow may either rise over the mountain or experience some degree of blocking and deflection. This response depends on the nondimensional mountain height:

$$M = Nh_m/U,$$

where N is the Brunt-Väisälä frequency, h_m is the mountain height, and U the cross-barrier wind speed (Kirshbaum et al., 2018). The larger the M (> 1), the larger the tendency for flow blocking. Hence the higher the static stability, and the lower the cross-barrier wind speed, the

stronger the blocking. This acts to artificially move the influence of the mountain upstream due to the dense, blocked air at the mountain foot and shift the zone of orographic lift and precipitation fallout upstream (Houze, 2014). 'Unblocked flows' tend to exhibit larger vertical displacement of air and precipitation fallout further downstream. In statically unstable flows, the mechanical lift from orography may help to trigger convection and produce convective clouds and precipitation.

Microphysical time scales play a part in orographic precipitation amounts and geographic distribution (Houze, 2014). Particle growth processes and hydrometeor types are relevant in the way that cold cloud processes (deposition and riming) are more efficient at precipitating than warm cloud processes (collision-coalescence), and different hydrometeors have different fall velocities, which determine the amount of precipitation and the time for it to reach the ground, and hence the location of surface precipitation due to advection with the wind.

2.4.2 Moisture sources, sinks and transport

In a climate perspective it is important to understand the contribution to regional precipitation from local surface evaporation versus horizontal transport of moisture, which is tied to the underlying physical processes. In boreal winter, the 'recycling rato', defined as the fraction of precipitation resulting from local surface evaporation to total precipitation, is very small over Northern Europe, meaning that most of the regional precipitation is generated from moisture transported into the region (Trenberth, 1999). Most of this moisture is associated with extratropical cyclones within the storm tracks (Bjerknes, 1922), and up to 90% of the precipitation within these storm track regions is associated with warm and cold fronts (Catto et al., 2012). The most extreme precipitation events at mid-latitudes are often associated with atmospheric rivers (ARs) in combination with extratropical cyclones (Dacre et al., 2015; Dettinger et al., 2015; Sodemann et al., 2020), particularly when interacting with topography (Azad & Sorteberg, 2017; Lavers & Villarini, 2013; Ramos et al., 2016; Stohl et al., 2008). ARs transport more than 90% of the total midlatitude vertically integrated water vapor (Zhu & Newell, 1998), originating from regions of high SST in the subtropics (Knippertz & Wernli, 2010; Ramos et al., 2016). Stohl et al. (2008) found that (sub)tropical moisture sources can contribute significantly to precipitation in southwestern Norway.

In contrast to this long-range transport of moisture with relatively long residence time (4-5 days) (Sodemann, 2020), Papritz and Sodemann (2018) revealed that during situations of winter MCAOs, about one third of the moisture taken up from the Nordic seas' surface falls as local precipitation through convective overturning with about one day residence time. As the air mass of the MCAOs is advected over warmer waters in the Norwegian Sea, precipitation efficiency increases even further. Depending on the frequency and severity of MCAOs in the Nordic seas during a winter, this implies that local evaporation from the sea surface contribute to a considerable portion of the regional precipitation in winter than what was portrayed by Trenberth (1999). As Papritz and Sodemann (2018) state: 'During periods with the frequent passage of cyclones, precipitation in the Norwegian Sea and over Norway is […] characterized

by temporally highly variable moisture source regions and associated uptake conditions, moisture transport, and time scale from evaporation to precipitation'.

2.5 Atmospheric icing

2.5.1 Icing types

Rime ice

Liquid cloud droplets can exist in air of temperature below freezing, which is termed supercooling. However, when the droplets come in contact with an object, they instantaneously freeze, creating a layer of ice on the object. This ice is called rime ice, and the process of icing is also referred to as in-cloud icing. The presence of wind acts to increase the flux of cloud droplets colliding with the object, and the higher the wind speed, the denser the accumulated ice becomes. The wind direction has a large impact on the accumulated ice shape, as the collection of cloud droplets and hence the accretion of ice occurs at the windward side of the object. If the air temperature is above freezing, the ice growth becomes wet due to partial melting, and is referred to as glaze ice.

Rime ice is typically observed in mountainous areas, where terrain elevation is within cloud height, clouds are frequent, and air temperatures are frequently below freezing. In such areas the meteorological conditions often facilitate the accumulation of large and heavy ice loads, accumulated over several weeks. This can become problematic for infrastructures if they are not built to withstand the weight of the ice. Norway has experienced some of the highest recorded rime ice loads on overhead power lines, with a record-breaking event registered at Voss in the mountains of western Norway of 305 kg/m (see Figure 2.5) (Fikke et al., 2008).

Figure 2.5: Rime ice on a power line, 1410 m.a.s.l. at Voss, Norway, in April 1961. (Photo: Olav Wist. Rights: Kjeller Vindteknikk).

Wet snow ice

When snow is falling across the melting level, it begins to gradually melt, consisting of a mixture of liquid water and ice. In this state the snowflakes are sticky and can easily adhere to an object. When this happens a layer of ice might accumulate, then referred to as wet snow ice. The wet bulb temperature (T_w) contains information about air temperature (T), humidity and pressure, and precipitating particle surfaces have a temperature closer to T_w than T (Ding et al., 2014; Harder & Pomeroy, 2013). Snow can exist in its dry form when T > 0°C if relative humidity is below 100 % (sub-saturated conditions), because evaporation will occur on the snowflake surface, a process which removes heat from the snowflake and keeps it cool and dry (evaporative cooling) (Stewart, 1992). As such, the wet bulb temperature is a more accurate measure of the phase of the precipitation (Makkonen, 1989). The 'stickiness' of the snow depends on its liquid to solid ratio (or solid ratio, SR), which is a function of T_w and its size. When $0 > T_w > 1$°C conditions are typically ideal for wet snow ice formation, or when $0.5 < SR < 0.98$ (Nygaard et al., 2013).

Wind speed also contributes substantially to wet snow ice accretion, with higher wind speeds causing larger and more densely packed ice. If falling snow becomes dry following a period of wet snow ice accretion, this dry snow might also adhere to the wet and sticky surface of the accumulated ice, however this mostly occurrs in low-wind conditions.

Wet snow icing is typically associated with winter storm events, with high precipitation intensities and wind speeds. In 2005 a record breaking wet snow storm in Germany and neighboring countries caused damages to five lines and totally 83 steel lattice towers (Makkonen & Wichura, 2010) (see Figure 2.6). But damages might also be caused in calm wind conditions, when the contribution from dry snow might be substantial.

Figure 2.6: Wet snow ice on a cable in the Münsterland area, Germany, 2005. (Photo: Wichura and Kiessling (2009)).

2.5.2 Ice accretion modelling

The modelling of ice accretion has been standardized by accretion on a cylinder (of 1 m length and 3 mm diameter) (ISO, 2017). The expression is given by:

$$\frac{dM}{dt} = \alpha_1 \alpha_2 \alpha_3 w v A$$

where *dM* is the accumulated ice mass per unit length during the time step, *dt*, *w* is the mass concentration of the relevant hydrometeor, *v* is the wind speed, *A* the cross-sectional area of the object, and $\alpha_1, \alpha_2, \alpha_3$ the collision, sticking and accretion efficiency, respectively. The collision efficiency, α_1, is the ratio of the incoming flux density of the particles that hit the object (as opposed to being deflected around the object with the air flow) (Makkonen, 2000). Smaller droplets have a larger tendency to be deflected around, and hence have a smaller α_1. The sticking efficiency, α_2, is the ratio of the flux density of the particles that hit the object that sticks to the object, as particles may bounce off the object surface. The accretion efficiency, α_3, is the ratio of the rate of icing to the flux density of the particles that stick to the surface. This term represents a heat budget, and estimates if part of the sticking particles melt off (and hence is not relevant if the ambient temperature is below freezing). As the α's are ratios representing factors to reduce *dM/dt* from its maximum value, their values are between 0 and 1.

When considering wet snow icing, snow is the relevant hydrometeor, and as snowflakes are relatively large, all particles may be expected to hit the object, and α_1 = 1. Concerning rime icing, cloud droplets are small enough to be deflected, and so $\alpha_1 < 1$. As mentioned, the collision efficiency depends on the droplet sizes, as well as the wind speed and object dimension. Correct estimation of α_1 depends on complicated numerical solutions of airflow and droplet trajectories, but have been simplified for practical applications by assuming a cylindrical icing object and applying an analytical solution (Finstad et al., 1988):

$$\alpha_1 = A - 0.028 - C(B - 0.0454)$$

$$A = 1.066K^{-0.00616}e^{-1.103K^{-0.688}}$$

$$B = 3.641K^{-0.498}e^{-1.497K^{-0.694}}$$

$$C = 0.00637(\varphi - 100)^{0.381}$$

$$K = \frac{\rho_w d^2}{9\mu D}$$

$$\varphi = \frac{Re^2}{K}$$

$$Re = \frac{\rho_a d v}{\mu}$$

K is the droplet inertia parameter, *Re* the Reynolds number based on the free stream velocity, *v*, *d* the droplet diameter, *D* the cylinder diameter, ρ_w and ρ_a the density of water and air, and

μ the absolute viscosity of air. Cloud droplets exist in a wide range of different sizes, and the median volume diameter (MVD) of the droplet size spectrum is typically used as d in the calculations (Finstad et al., 1988). This simplification has however been shown to lead to underestimation of ice accretion, particularly for small values of K (Sokolov & Virk, 2019). Typical situations that yield small values of K are calm wind conditions and/or large cylinder diameters. Consequently, a better description of the droplet size spectrum, such as the full Langmuir D distribution, should yield more accurate predictions than the monodispersed droplet size distribution (MVD).

As for the sticking efficiency, cloud droplets do not tend to bounce off the object surface as they are purely liquid, and hence $\alpha_2 = 1$ for rime icing. Snowflakes, however, bounce off more easily, and $\alpha_2 < 1$ for wet snow icing. The most commonly used expression for α_2 is a simple inverse relation to the wind speed (Admirat, 2008; ISO, 2017) . However, Nygaard et al. (2013) found this to significantly underestimate accumulated wet snow loads, and proposed a new and improved expression, involving also SR to represent the stickiness of the snow:

$$\alpha_2 = \frac{1-\cos(9SR-4.5)}{2v^{0.4}} \quad \text{for } 0.5 < SR < 0.98,$$

$$\alpha_2 = 0 \text{ otherwise.}$$

Accretion efficiency, α_3, involves a heat balance equation:

$$Q_f + Q_v = Q_c + Q_e + Q_l + Q_s$$

where Q_f is the latent heat released during freezing, Q_v is the frictional heating of air, Q_c is the loss of sensible heat to air, Q_e is the heat loss due to evaporation, Q_l is the heat loss in warming the impinging supercooled water to the freezing temperature, and Q_s is the heat loss due to radiation. For the full equation of α_3 the reader is referred to Makkonen (2000). $0 < \alpha_3 < 1$ represents 'wet' ice growth due to presence of meltwater (the largest rime ice loads are typically accumulated in dry conditions). When $\alpha_3 < 0$ mass is overall removed due to melting or sublimation. Wet snow icing is always wet, however, α_3 is rarely calculated for wet snow accretion. This is because the melt water is soaked into the snow sleeve by capillary forces instead of dripping of, a process that is highly complex to model. This melt water may contribute to destroy the ice grains that hold together the snow sleeve (Colbeck & Ackley, 1982) and lead to shedding for a certain fraction of melt water. As explained in Makkonen (2000): "It is likely that the upper temperature limit of wet snow accretion is set by shedding caused by the collapse of the integrity of the snow deposits rather than by overall melting".

Studies have demonstrated successful usage of NWP model data to simulate realistic ice loads on power lines with the expressions given above (Elíasson et al., 2015; Haldar, 2016; Nygaard et al., 2017a; Nygaard et al., 2011; Nygaard et al., 2013; Thompson et al., 2009). Such modelling involves the utilization of the hydrometeor output from a sophisticated microphysics scheme.

Chapter 3 :Research Tools

3.1 WRF

The main tool used in the research of this thesis, contributing to the results of each paper, is The Weather Research and Forecast (WRF) model. The WRF model is a mesoscale, limited area NWP model system designed for both research and operational weather forecasting (Skamarock et al., 2019). It is developed by American research institutions, predominantly the National Center for Atmospheric Research (NCAR) and National Centers for Environmental Prediction (NCEP). WRF is used operationally at NCEP, for real-time forecasting at international universities, companies and science institutions, for research purposes worldwide, and has over 48 000 registered users in over 160 countries, and countless scientific publications based on its application.

WRF is a nonhydrostatic model with terrain-following hybrid sigma-pressure vertical coordinate. WRF can be run with input from operational analyses or reanalysis datasets (3D), or as idealized simulations in 1D, 2D or 3D, which is advantageous for research purposes. It is highly modular and comes with a myriad of options for configuration, including several different options for physical parameterization schemes, enabling optimal configurations for any application, as well as testing, tuning and comparisons of different options.

The WRF setup used in this thesis (parameterization choices are listed in Table 3.1) is optimally selected for the purpose of simulating atmospheric icing, and has been found through extensive research on the topic, including the PhD project of Bjørn Egil Nygaard (Nygaard, 2013), and the two research projects, FRonTLINES (Nygaard et al., 2017a) and IceBox. Most of this research focus has been with respect to microphysics due to the direct use of the microphysical fields in the icing calculations. WRF, with the Thompson microphysics scheme, has shown high performance for icing applications (Ingvaldsen et al., 2019; Nygaard et al., 2022; Nygaard et al., 2011; Nygaard et al., 2013; Podolskiy et al., 2012; Thompson et al., 2009; Thorsteins et al., 2022).

In the context of climate change and downscaling, WRF is applied as one of many regional models in the CORDEX experiments of the CMIP6, and there are many examples of its application to studies of future climate in the literature (e.g., El-Samra et al. (2017); Knist et al. (2020); Liu et al. (2017); Shepherd et al. (2022); Viceto et al. (2017)).

Table 3.1: Parameterization scheme choices for the WRF model configuration used in this thesis.

Type of scheme	Name	Reference
Microphysics	Thompson-Eidhammer aerosol-aware	Thompson and Eidhammer (2014)
Boundary layer	MYNN2	Nakanishi and Niino (2006)
Radiation	RRTMG	Iacono et al. (2008)
Land surface	Noah	Chen and Dudhia (2001)

3.1.1 The Thompson microphysics scheme

The Thompson microphysics scheme, provided as part of the WRF model, has been explicitly developed and extensively tested for forecasting winter precipitation and atmospheric icing (Thompson & Eidhammer, 2014; Thompson et al., 2008; Thompson et al., 2004). This, as well as its successful application for the simulation of ground-based icing, and overall well-documented high performance (Brown et al., 2016; Liu et al., 2011; Rögnvaldsson et al., 2011) are the reasons for choosing this specific microphysics option. The scheme is a partially double moment bulk scheme where each of its five hydrometeor species is represented by generalized gamma size distributions. Cloud water, cloud ice and rain are double moment, while snow and graupel are single moment. The scheme consists of physically based assumptions to force it to act similarly to a full double-moment scheme, making it suitable for real-time NWP due to the decreased computational cost compared to higher order schemes. There are two aspects that make this scheme unique: Its snow size distribution is described by a sum of exponential and gamma distributions, and snow assumes a non-spherical shape with a bulk density that varies inversely with diameter. Thompson and Eidhammer (2014) have also developed the scheme to be aerosol-aware, making use of prescribed aerosol concentrations, which is a unique option in WRF in addition to the original scheme. Details of the scheme relevant for the work carried out in Paper I can be found in the attached paper.

3.2 Selected global climate models

The data behind the research of Paper II and III is from a dynamical downscaling (using WRF) of two chosen global climate models, with experiments obtained from the historical simulations and the ScenarioMIP of the CMIP6. Following is a short description of the two models.

CESM2

The Community Earth System Model Version 2 (CESM2) is the latest generation of the open-source community coupled climate/Earth system models developed mainly at NCAR (US) (Danabasoglu et al., 2020). For the CMIP6 simulations the model uses a 1° horizontal grid resolution grid, 32 vertical levels, a top at 226 Pa, and a relatively coarsely resolved stratosphere (the 'low-top' model version). Research efforts have identified the model to be one of the most realistic climate models in the world (Knutti et al., 2013; Simpson, 2020). Simpson et al. (2020) showed that CESM2 is a top-ranking model among the CMIP6 models considering validation of current climate large-scale atmospheric circulation, and particularly for circulation features centered over the North Atlantic basin. CESM2 is better than most models in capturing the west – east tilt of the North Atlantic jet stream and its latitudinal position, and performs well in terms of representing the northern hemisphere storm tracks. In terms of capturing atmospheric blocking statistics, CESM2 is a top-ranking model, though with a reduced blocking frequency compared to observed, common to all CMIP6 models. Certainly, many model errors and biases are present, such as an incorrect separation and path of the Gulf Stream-North Atlantic Current system and accompanying large SST and surface salinity biases. Its equilibrium climate sensitivity (ECS; global surface warming response to a doubling of CO_2) is 5.3 °C (Danabasoglu et al., 2020).

MPI-ESM1.2-HR

The Max Planck Institute Earth System Model version 1.2 (MPI-ESM1.2) is the latest version Earth system model developed at the Max Planck Institute in Germany (Müller et al., 2018). The model exists in a high resolution (HR) version (MPI-ESM1.2-HR) (which is selected in this work) with horizontal grid resolution of ~0.8° and 0.25° in the atmosphere and ocean respectively. The number of vertical levels is 95 and the model top is at 0.01 Pa with a relatively highly resolved stratosphere. Compared to MPI-ESM1.2, the higher resolution of MPI-ESM1.2-HR affects regional atmospheric dynamics such as improved North Atlantic storm tracks. The mean ocean circulation, such as the Atlantic Meridional Overturning Circulation (AMOC), compares well to observed estimates. In the North Atlantic region, the model suffers from biases related to SST (warm bias), the North Atlantic Current (too zonal), and storm tracks (too zonal). The SST bias has implications, for example for the prediction of winter storm intensities over Europe (Kruschke et al., 2015), which is particularly relevant for this research. MPI-ESM1.2 is specifically tuned to the instrumental-record warming, and its ECS is about 3 °C (Müller et al., 2018).

3.3 Icing models

The icing models applied in Paper II are based on the basic concepts of ice accretion modeling presented in Chapter 2.5.2, with some modifications and extra components. In addition to simulating the temporally varying ice accretion, the purpose of the models is also to simulate ice melting, sublimation and mechanical fall off (shedding), to obtain a realistic temporal evolution of accumulated ice. In the following, the two icing models are described, one for rime ice and one for wet snow ice.

Rime ice

The key meteorological variables on which the rime ice model is based include temperature, wind speed, cloud water content and cloud droplet number concentration. Based on the research by Sokkolov and Virk (2019), presented in Chapter 2.3.1, the Langmuir D distribution is applied for the droplet size spectrum. This will yield improvement for large ice diameters, which is highly relevant at high altitudes where prolonged icing events may allow continuous ice growth over several months, which is typical in the Norwegian mountains. The rime ice accretion model also accounts for supercooled rain (although this is not very commonly observed in Norway).

With respect to removal of accumulated rime ice, the model includes both melting and sublimation processes. Additionally, partial ice shedding during melting and sublimation periods is accounted for by including empirical "shedding factors" derived from comparisons of modelled melting and sublimation rates to measurements at high altitude sites in Norway.

Wet snow ice

The key meteorological variables on which the wet snow icing model is based include temperature, air humidity, precipitation and wind speed. The calculations of wet snow accretion use the expression described in Nygaard et al. (2013) (see Chapter 2.5.2). However, the model has been updated in several areas based on recent research (Thorsteins et al., 2022). Comparisons of measured and simulated wet snow loads have shown that the model from Nygaard et al. (2013) generally overestimates the observed wet snow loads at high altitude sites as well as on mountain lee sides. Here wet snow accumulation rates seem to be significantly reduced compared to what is suggested by the precipitation rates and the assumption that the collision efficiency of wet snow particles peaks when precipitation particles have a liquid water fraction of ~15 %. During wet snow periods at altitudes exceeding the cloud base (very common at > 1000 m.a.s.l. in Norway), the flux of impinging water particles consists of a mix between wet snow and cloud droplets. In our updated wet snow model the calculation of the precipitation solid-to-liquid-ratio (SR) therefore includes cloud droplets, which often reduces the accretion efficiency to zero at high altitudes (i.e. the snow becomes too wet). Furthermore, the updated wet snow model does not allow initiation of wet snow accumulation when graupel (i.e. rimed snow particles) constitutes more than 10 % of the precipitation particles. This is because graupel particles tend to bounce off ice-free conductors more easily compared to wet

snow. If the icing object/conductor is already covered with ice, the wet snow accretion rate is also slightly reduced depending on the amount of graupel.

The model also allows for dry snow (SR = 1) to accumulate, provided that the icing object/conductor is already covered with a layer of wet snow. However, dry snow may only accumulate at wind speeds < 5 m/s in the current model and will typically shed quite fast once the wind speeds increase due to the relatively low density of accreted dry snow.

Due to the complexities of modelling the melt water contained within the wet snow sleeve when melting as mentioned in Chapter 2.5.2, a simplification has been made in our model so that all the wet snow ice sheds of if the wet bulb temperature exceeds 0.75 °C after precipitation has ended. The model also removes all accumulated wet snow if the wind speed exceeds 0.04ρ, where ρ is the density of the accumulated wet snow (only valid for $\rho < 400$ kg m-3).

3.4 OLYMPEX observational data

Observational data from the Olympic Mountain Experiment (OLYMPEX) campaign in Washington state, U.S. (Figure 3.1), was used to compare with output from WRF in Paper I. The (OLYMPEX) is a ground-based field campaign designed to study orographic effects of a coastal mountain on passing midlatitude storm precipitation (Houze et al., 2017). It provides comprehensive field measurements from a great number of instruments around the Olympic Mountain to help improve our understanding of orographic precipitation modulation. Another objective of the campaign was to assess and improve the ability of the Global Precipitation Measurement (GPM) satellite, launched in 2014. The setup of instruments was designed to make measurements above, within, and below the clouds of passing storms, on the windward and leeward slopes, and the high terrain. The instruments included different scanning dual-polarization Doppler radars, which were set up with a primary focus on observing the microphysical processes upwind of and over the mountain. Surface instruments were installed to measure precipitation rates as well as rain and snow particle sizes and fall speeds (e.g. rain gauges, Micro Rain Radars (MRRs), distrometers). This was of high value for the validation of precipitation fall speed and general signature through the melting layer needed for Paper I.

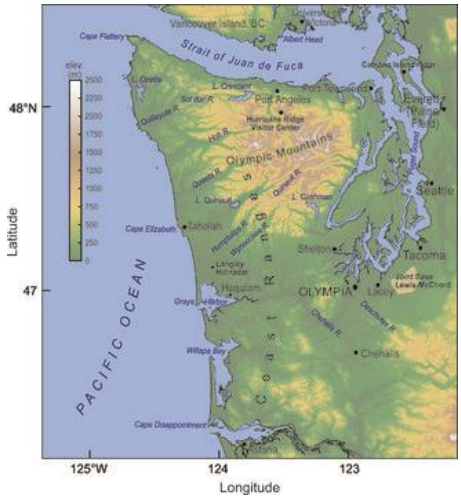

Figure 3.1: Map of the region where the OLYMPEX campaign occurred. From Houze et al. (2017).

Chapter 4 :Presentation of findings

This chapter presents summaries and main findings of the three papers enclosed in this thesis. Each paper presents its corresponding objective as presented in the introduction, and a main conclusion.

4.1 Paper I: Improvements to melting snow behavior in a bulk microphysics scheme

Emilie C. Iversen, Gregory Thompson, Bjørn Egil Nygaard

Manuscript published in Atmospheric Research, January 2021

Objective

The overall objective is to improve prediction of wet snow icing, which translates to improve predictions of precipitation phase and amount at the surface, using the WRF NWP model. The specific objective is to modify the Thompson microphysics scheme with respect to the representation of melting snow, without adding more model prognostic variables in order to maintain computational time for real-time operations.

Summary

This study presents improvements to the Thompson microphysics scheme, part of the Weather Research and Forecast (WRF) model, regarding the representation of melting snow. In reality, as snow is melting, the meltwater sticks to the snowflake so it becomes a mixture of ice and liquid water. Laboratory experiments have shown that the fall speed is a function of the liquid fraction, as well as the initial diameter of the dry snowflake. In the scheme, the melted water mass is immediately shed into the rain category, resulting in underrepresented snow sizes. Previously this led to underpredicted snow fall velocities, and to compensate for this, the velocity in the melting layer was firstly equaled to the maximum of the rain and snow velocity at the given model level, and in later versions, given as an inverse relation to temperature. This latter expression introduced a serious bug in the code, which was discovered during the work of this paper.

Here, a physically based expression for melting particle fall velocity as a function of snowflake melted fraction is implemented, where the melted fraction is approximated by the liquid precipitation mass ratio at the given model level. Also, improvements relate to the consistent use of wet-bulb temperature in various process rates and definition of melting level. Two events of frontal passages observed with multiple instruments during Dec 2015 by the Olympic Mountain Experiment (OLYMPEX) campaign are used to compare with the WRF model results.

Main findings

- The modified scheme is able to represent disdrometer (2DVD) observations of joint particle size and fall velocity during wet snow events, with a typical bimodal distribution.

- Particle fall velocity profiles through the melting layer derived from a vertically pointing radar (MRR) are well replicated by the scheme, and show a non-linear increase in fall velocity as snow is melting through the layer, in agreement with laboratory experiments (Mitra et al., 1990). The old scheme predicted too fast falling snow through the melting layer.

- The modified scheme shows a reduction in snow and an increase in rain accumulation in the melting zone around the Olympic Mountain as a result of slower falling snow during melting. Snow accumulation is particularly decreased in lee side areas, where the old scheme showed significant and unphysical accumulation due to too fast falling velocities.

Main conclusions

The fall velocity of melting snow has been improved in the Thompson microphysics scheme, demonstrated through comparisons with observations. The substantial impact of the modifications on accumulated precipitation over a mountain is shown. A lee-side precipitation overprediction problem related to the melting layer, also noted in previous research (Colle et al., 2005), is demonstrated to be improved. This should generally result in better predictions of precipitation phase and amount at the surface, also contributing to improved predictions of wet snow icing as well as hydrological modelling, however this remains to be validated.

Author contribution: *I have contributed to design the study. I have carried out all the analyses of this study, with guidance on WRF modelling and the microphysics scheme from Gregory Thompson, and supervision from Bjørn Egil Nygaard. I have written the article, with revision from the co-authors.*

4.2 Paper II: Future projections of atmospheric icing in Norway

Emilie C. Iversen, Bjørn Egil Nygaard, Øivind Hodnebrog, Maria Sand, Kristian Ingvaldsen

Manuscript submitted to Cold Region Science and Technology, March 2022

Objective

The overall objective is to project future occurrence of atmospheric icing in Norway, from the perspective of structural design, with a specific focus on overhead power lines. Extreme values of wet snow and rime ice loads are the focus of the study. Projection spreads are investigated as a measure of uncertainty, by using two differing climate models and three future climate scenarios in a downscaling framework.

Summary

In this paper we present estimated changes in calculated 10-year return period values of atmospheric ice loads (wet snow and rime ice) in Norway based on the downscaling of two climate models, CESM2 and MPI-ESM1-2-HR, to a horizontal resolution of 12 km, using the WRF model with the modifications presented in Paper I. Three future scenarios (socioeconomic pathways, SSPs) are downscaled (ssp126, ssp245, ssp370), and three future periods are investigated separately (2025-2049, 2050-2074, 2075-2099) (relative to the reference period 1990-2014). The results indicate that the North Atlantic warming hole (NAWH) exerts a strong influence on our results, by affecting regional temperature, precipitation and cloud water content change patterns. Furthermore, it is shown that the downscalings of our chosen models project a relatively large difference in atmospheric ice loads, hypothesized to be connected to their different signatures of the NAWH. The warming hole in CESM2 is strong (Meehl et al., 2020) and one of the strongest among the CMIP6 models, leading to a cooling of surface temperatures over the North Atlantic Ocean extending as far north as northern Norway.

Main findings

- Concerning rime ice, increased temperature leads to shorter duration icing episodes, implying less accumulated ice and lower loads, whereas increased cloud water content leads to increased ice loads. The moderate regional warming in the downscaling of CESM2 and the general increase in extreme values of cloud water content acts to pull the resulting change in 10-year rime ice loads in opposite directions (results show indications of decreases in the early period and increases in the latter). If the development of the NAWH will be as extreme as projected by CESM2, rime ice loads may increase by 20 – 100 % towards the end of the century (with higher confidence for moderate emission scenarios). If the NAWH strength and northerly extent is more moderate, as projected by MPI-ESM1-2-HR, regional warming will be stronger, and the temperature effect will dominate the change (over the cloud water effect) on extreme rime ice loads, causing significant decreases for all time periods (10 – 60 %).

- For wet snow, the projected changes by the two downscaled models are relatively similar: 10-year wet snow loads are generally decreasing in the lowlands (10 – 50 %) and increasing over higher terrain (10 – 100 %) due to a general increase in temperature and extreme daily precipitation. A reduction in extreme precipitation over parts of mid-Norway in the CESM2 downscaling, connected to the NAWH, could lead to reduced wet snow loads at all elevations in this area (roughly 40 %). The relatively large cold bias of the MPI downscaling most likely causes the areal extent of decreased wet snow loads in low-lying areas to be underestimated. There is no evident pattern in the time evolution of changes in wet snow loads.

Main conclusions

Results based on both climate models indicate that future 10-year return period of wet snow loads are generally decreasing in the lowlands and increasing at higher elevation for all three scenarios, linked to a general increase in temperature and extreme precipitation. There are also indications of decreasing wet snow loads in the CESM2 downscaling towards the end of the century due to decreasing precipitation extremes connected to the development of the NAWH. Results for future 10-year rime ice loads differ between the two downscaled models due to differences in regional warming levels and model biases. More research, possibly involving downscaling of more climate models, is needed to constrain the signal. However, large uncertainties in projections of large-scale oceanic and atmospheric circulation and regional climate response, as well as climate model biases, challenge the constraint.

Author contribution: *I have contributed to design the study. Øivind Hodnebrog and Maria Sand at CICERO have carried out the preliminary analyses of correlating icing occurrence with the NAO and performing EOF-analysis of a number of CMIP models. They have also performed the downscaling with WRF to generate the atmospheric data. I have run the icing models, mostly developed by Bjørn Egil Nygaard in his PhD thesis, with modifications by myself and Kristian Ingvaldsen over time, and I have calculated extreme values. I have performed the rest of the analyses and written the article, with revision from the co-authors.*

4.3 Paper III: Future winter precipitation decrease associated with an extreme North Atlantic warming hole and reduced convection

Emilie C. Iversen, Øivind Hodnebrog, Lise Seland Graff, Bjørn Egil Nygaard, Trond Iversen

Manuscript in preparation and planned for JGR Atmospheres

Objective

The main objective is to investigate and understand the physical mechanisms explaining the winter precipitation decrease in CESM2 and its downscaling with WRF, found over the northeastern North Atlantic region, and its connection to the NAWH. To fully understand the precipitation response, stratiform, convective and orographic precipitation is investigated separately.

Summary

The CESM2 global climate model projects one of the deepest and most spatially extensive NAWHs of the CMIP6 models, leading to a cooling of the ocean surface which extends to the Norwegian and North Sea. The model also projects winter precipitation decreases in the same region. To understand the physical mechanisms of this response, stratiform and convective precipitation is investigated separately, as they are generated by distinctly different mechanisms and hence respond differently to underlying SST changes. Orographic precipitation is also investigated separately, as the Scandinavian mountains contribute substantially to the precipitation received in the region through orographic effects. Given the large errors associated with convection schemes of global models, as well as the poorly resolved orography, the higher resolution model (WRF) without parameterized convection applied here should improve the details of the projections. Here we use the downscaled data from the WRF model and three future emission scenarios, to investigate the connection between the NAWH and changes in stratiform, convective and orographic precipitation in winter (Dec-Feb).

Main findings

- Stratiform precipitation decreases (10 – 30 %) north of 45ºN and increases (10 – 30 %) south of 45ºN (also valid for its frequency), which corresponds well with CESM2's projected changes in storm-track activity. The results show that prevailing wind directions change from westerly to south-westerly, indicating changes in the orientation of storm-tracks. A southwesterly path will detour the warming hole (to the south) to a larger degree than a westerly path, and hence pick up more moisture along the way.

- Convective precipitation decreases over the climatological area of occurrence (10 – 40 %), which constitutes major parts of the Norwegian Sea and Norway's west coast. The reduced SSTs of the NAWH lead to reduced evaporation and increased atmospheric static stability, which contributes to reduce available moisture, convective triggering, convective intensity, and hence convective precipitation amounts.

- Orographic precipitation shows a distinct pattern of decrease (10 – 30 %) above and increase (10 – 50 %) below roughly 500 m above sea level on the western slopes of the Scandinavian mountains. The results and literature indicate that this is related to 1) increased static stability, causing increased terrain flow blocking, which moves the zone of orographic lift upstream, 2) reduced cross-barrier wind speed, 3) the higher frequency of rain versus snow in a warmer climate (rain has a higher fall velocity which leads to a shorter horizontal advection distance, hence making the precipitation fall out further upstream than if it consisted predominantly of snow) (Colle, 2004; Pavelsky et al., 2012).

The precipitation signals are robust responses in the downscaling experiments of CESM2 across the three scenarios. The responses are also evident in the CESM2 fields directly, and are also robust across the range of scenarios and different ensemble members, although not with the same magnitude and level of detail as simulated with WRF.

Main conclusions

The results indicate that the anomalously cold SSTs of the NAWH as projected by CESM2 leads to a considerable decrease in winter convective precipitation in the region. The results further indicate that the local, direct negative surface heat and moisture flux impact of the NAWH on the convective precipitation dominates the impact of other global warming related aspects, including increased storm activity and increased stratiform precipitation south of 45°N. The upstream shift in orographic precipitation distribution seems also to be, at least partly, connected to the NAWH through the increased static stability, however research is needed to isolate the individual proposed mechanisms. It should be stressed that the experiments are based on an extreme projection of the NAWH from one climate model and an end of the century period, serving as an extreme scenario of precipitation changes in coastal Northern Europe. Given the significant societal impacts of such changes, this study demonstrates that more research is urgently needed to constrain future climate projections in the North Atlantic region.

Author contribution: *I have designed the study. The WRF data was generated in association with Paper II (by Øivind Hodnebrog and Maria Sand). Lise Seland Graff has carried out the analysis of storm track changes and created the figures based on CESM2 directly, while I have performed the rest of the analyses. I have written the article, with revision from the co-authors.*

Chapter 5 :Discussion, future outlook and concluding remarks

The main objective of this thesis is to improve predictions of atmospheric icing and winter precipitation, and project the future occurrence in Norway. Three sub-objectives emerged from this, which are each met in a paper:

1) Improve the Thompson microphysics scheme representation of melting snow behavior.
2) Project the future occurrence of extreme wet snow and rime ice loads in Norway, applying the improvements from 1).
3) Investigate and understand the physical mechanisms behind the winter precipitation response in the projections from one of the climate models applied in 2) (CESM2).

5.1 Summary, discussion and future work

In previous work the estimation of wet snow loads, particularly in the lee of mountains and hills, appeared unrealistically high, and it was hypothesized that this was connected to limitations and simplifications of the applied Thompson microphysics scheme in the WRF model used for generating the meteorological data, and more specifically the fall speed of snow. Similar results of accumulated precipitation were also noted by other authors (Colle et al., 2005). The work of Paper I identified a serious bug in the Thompson microphysics code related to the fall speed of melting snow, which substantially contributed to this leeside overprediction problem, as well as precipitation forecast errors not documented. This bug was part of the latest versions of the freely available model code, and hence its discovery was an important contribution. Paper I proposes a new expression for fall speed of snow in the melting layer, and demonstrates the improvement through comparisons with observations, as well as the more qualitatively physically correct accumulation of precipitation in leeside terrain. One figure also demonstrates the changes to the distribution of accumulated precipitation (snow and rain) over a mountain (Figure 13 in Paper I). A limitation of this work is the lack of validation of these resulting changes to precipitation phase reaching the ground and the associated spatial distribution, which are relatively large and would greatly affect precipitation forecasts as well as hydrological modeling. This could be carried out using networks of precipitation gauges, or satellite products, however, one needs to be aware of the biases and errors contained in such products, and particularly in mountainous areas.

To more closely connect the results of Paper I with the objective of this thesis, the introduced changes to the Thompson scheme should also be validated with respect to calculated wet snow loads, to evaluate whether it leads to improved wet snow ice predictions. Such work has been carried out within the Icebox project (Thorsteins et al., 2022), which indicates reasonably good

estimates of wet snow loads as compared to observations made in Iceland, and particularly related to the microphysics changes, leeside areas show good estimates and no apparent overprediction.

The microphysical modifications described in Paper I were applied in the downscaling of two global climate models and three future scenarios, applied for the projection of future atmospheric ice loads in Norway, described in Paper II. In this study a careful selection of a limited number of climate models had to be made, as dynamical downscaling is computationally demanding to perform. Three future scenarios were chosen, and consequently only two climate models could be selected due to time and budget constraints. The results of Paper II reveal substantial differences between the downscaled projections of the two climate models, hypothesized to be connected to the large difference in regional warming due to the NAWH. Also, projected ice loads are affected by substantial climate model biases. The differences between the downscaled scenarios are of smaller magnitude than the inter-model differences and generally show the same trends, but of different magnitude. This implies that the climate model physics and biases are spanning the largest uncertainty in this region. In hindsight we would therefore ideally choose more climate models to downscale over the chosen number of scenarios.

At the time of selection of climate models, we were not fully aware of the surface temperature cold bias of MPI-ESM1-2-HR in the region, which is substantially affecting the estimated ice loads. Nor were we aware of CESM2's extreme projection of warming deficit in the region (NAWH), which makes this downscaling an outlier scenario in this respect. As is described in Danabasoglu et al. (2020), CESM2 contains errors in the separation and path of the Gulf Stream-North Atlantic Current system, causing warm-cold SST bias dipoles in the North Atlantic as compared to observations. The NAWH in MPI-ESM1-2-HR is less pronounced than in CESM2 (see Figure S3 of the Supplement to Paper II), yet Müller et al. (2018) reveal that MPI-ESM1-2-HR also contains an SST bias in the North Atlantic similar to CESM2 with a dipole structure. It is not clear how this SST bias and associated model errors affect the projected formation of the NAWH and if the extreme NAWH in CEMS2 is a consequence of this. However, given the large climatic impact of North Atlantic SSTs, these projections should be treated with caution. In hindsight, climate model biases over this specific region of interest should have been thoroughly inspected before choosing models to downscale, possibly revealing other climate models to be better suited for this purpose. With that being said, all climate models contain substantial biases in some form, and it is not necessarily straight forward to evaluate the impact of such on the application of the model in advance. The selection of models for this study was supported by their overall high performance, and particularly in simulating important regional circulation features, as well as reasonable Arctic mean temperatures (Cai et al., 2021).

Paper II also discusses natural variability within the data, and the challenge of isolating the climate change signal with such a small model ensemble. To increase our understanding of future ice load changes, downscaling should ideally also be performed for several future realizations of the same climate model, to investigate the span in projected changes based solely on natural variability of the climate system. If this also turns out to be relatively small compared

to the inter-model spread, the focus could be more confidently directed towards including more climate models in the analysis. It is clear that in order to use these future ice load projections for practical application in structural design, more work is needed to better understand the span and uncertainties of climate projections in this region, possibly involving downscaling of more climate models.

The downscaling of the CESM2 climate model showed a surprising result; the projections of winter precipitation showed decreases over large parts of Norway and the Norwegian Sea, which is contradictory to the scientific consensus of 'wet regions get wetter' (Held & Soden, 2006) and the conclusions for future winter precipitation change for the region in the latest assessment report of the Intergovernmental Panel on Climate Change (IPCC) (Ranasinghe et al., 2021). Regional future precipitation change is of high societal importance to understand, and future wet snow ice occurrence for structural planning is just one reason. Paper III seeks to investigate and understand the physical mechanisms behind this precipitation response, with a particular focus on the connection with the extremely projected NAWH. As stratiform and convective precipitation is generated by different mechanisms, these precipitation types are separated to better understand the response. As orographic precipitation also contributes significantly to the precipitation received in this region, this type is also investigated separately.

A limitation of this study is the lack of a thorough validation of the models, simulated precipitation, as well as the precipitation separation method into stratiform, convective and orographic contributions. A qualitative validation of the separation was performed by visual inspection of the output, evaluated to be of desired quality, however, this could not be quantified. If a validation towards observations was to be performed, challenges would most likely arise related to the separation of the observational precipitation, and the detection of model errors related to the precipitation separation algorithm versus errors in the actual simulated precipitation types. The latter could also be related to both biases in the forcing global model and the regional model itself. The historical (1990-2014) precipitation was validated in Paper II, and it was revealed that the downscaling contains a substantial wet bias. As precipitation response mechanisms are highly nonlinear, it is also challenging to evaluate how this wet bias affects the projected changes. The aforementioned Gulf Stream-North Atlantic Current system and SST bias in the CESM2 model likely also affect our results, however it is difficult to estimate in what way.

Another potential weakness of this study, which is also valid for Paper II, is the use of a 12 km regional model without parameterized convection. This choice of 12 km grid resolution was made from the trade-off between number of scenarios, number of models, temporal extension and model resolution. The chosen grid spacing is however slightly larger than the 'convective gray zone' and no parameterization of convection was applied. A large number of studies have highlighted the significant improvement of using convection permitting models (grid spacing < 4 km) over convective parameterizations for studies of precipitation (e.g. Ban et al., 2021; Ban et al., 2014; Fosser et al., 2015; Hohenegger et al., 2008; Kendon et al., 2012; Meredith et al., 2015; Prein et al., 2015; Prein et al., 2020), also for winter precipitation (Kendon et al., 2020; Lind et al., 2020; Rasmussen et al., 2011). The added value has been mostly connected to deep convection, sub-daily precipitation characteristics and orographic precipitation. Also, of high

importance to this study, added value has been highlighted for ocean triggered convection advected over land in typical winter conditions, where convective parameterizations fail due to their lack of memory and hence ability to advect (Kendon et al., 2020). Relatively few studies focus on the added value of running a regional scale model (> 4 km) without parameterization of convection, however those that have generally also find improvements over convective parameterizations (Birch et al., 2015; Dirmeyer et al., 2012; Field et al., 2017; Hohenegger et al., 2015; Pearson et al., 2014; Stein et al., 2015; Vellinga et al., 2016; Vergara-Temprado et al., 2020). Field et al. (2017) found relatively small differences in accumulated rain between simulations with and without a convection scheme for resolutions of 2 – 16 km for an MCAO case north of Scotland. All the above support our choice of turning off the convection scheme at 12 km grid spacing. However, convection is far from accurately represented at 12 km – updrafts are too weak and precipitation is indicated to be underestimated (Field et al., 2017; Papritz & Sodemann, 2018; Tomassini et al., 2017). It would be interesting to quantify the precipitation bias associated with explicitly treated convection at 12 km grid spacing down to 'convection resolving scale' (~1 km) for ocean triggered winter convection, with identical WRF configurations and forcing data, which is a suggestion for future work. Given that the primary added value of higher resolution (in addition to better represented orography) is on the sub-daily time scale and not for mean values (Berthou et al., 2020; Chan et al., 2013), and that the most important average orographic effects are indicated to be sufficiently represented at this grid scale (Pavelsky et al., 2011; Rhoades et al., 2018), the applicability of this data is supported for the purpose of this study.

A rather simple approach was used to identify orographic precipitation in Paper III, with the aim of capturing 'pure' orographic precipitation (not orographically enhanced precipitation). This approach will also classify the back of a warm front, as well as convective cells generated over ocean, as orographic if they are advected over land and do not cover any area of the ocean at that time. This will lead to a misclassification, however, the visual inspection noted that this occurred relatively rarely and did not impact the results to a significant degree. The fact that the same orographic response is seen in the stratiform component of the results (orographically enhanced stratiform) supports the validity of the orographic component results. As was stated in the paper, it would be ideal to perform idealized simulations for orographic precipitation conditions, with the possibility to isolate the different proposed mechanisms to explain the orographic response (increased static stability, reduced cross-barrier wind speed, a shift from snow to rain). This could be performed using a pseudo global warming (PGW) study, where future thermodynamic changes are added to present day weather to mimic climate change, like for example performed in Liu et al. (2017), Sandvik et al. (2018), and Siller and Roe (2014). This method will allow for the comparison of the same weather and circulation regimes, but for the 'future' period, with changed temperatures and associated thermodynamic variables. This is suggested as future work.

The data behind the results of Paper III contains other aspects of climate change in addition to the reduced SSTs from the NAWH. Storm activity changes were analyzed in the paper using a bandpass filter on the 500 hPa geopotential height field, however this does not give quantitative information on the exact track, frequency and intensity of cyclones moving through the region. Nor was any other detailed analysis of changing dynamics included, which might also

contribute to the precipitation signal. For example, as noted in the paper, winter convective activity in the region is closely related to MCAOs. To increase confidence in the results, more detailed analyses of dynamics such as storm tracking or MCAO frequency/intensity estimates could be carried out. A PGW study could also help to isolate the thermodynamic effects of decreased SSTs on the precipitation in the region. This could for example be carried out for an MCAO event, where the water cycle has been shown to be highly confined with rapid overturning of moisture (Papritz and Sodemann 2018), enabling a close to complete isolation of the surface temperature change effect on convective precipitation amounts and the quantification of such. These are possibilities for future work. With that being said, the fact that the results are consistent between the three downscaled scenarios, despite varying storm activity changes, gives confidence that the results are robust and that they are related to the NAWH. The question is to what extent they are valid, given the extreme NAWH of CESM2 and the mentioned model biases. Nevertheless, this study demonstrates the significant impact local SST and surface temperature changes may have on regional precipitation, and the importance of therefore improving these biases in the models and constraining the signals of the relevant climate features in the North Atlantic region.

5.2 Concluding remarks

The work undertaken in these three papers meets the overall objective of this thesis. The work has contributed to discover and fix a serious bug in the code of a widely applied microphysics scheme, to improve its melting snow behavior and consequently improve the model's ability to realistically simulate the spatial distribution of precipitation in complex terrain, particularly in lee side areas. This will hopefully lead to improved precipitation forecasts and input to hydrological models, but the resulting changes to accumulated precipitation phase and its spatial distribution remains to be validated quantitatively. The implemented changes contribute to improved wet snow icing predictions in lee side terrain, and predictions in other areas have also shown to be of good quality, however this has not been directly tied to the changes made to the microphysics scheme.

The work has also created the first set of projections of atmospheric ice loads for Norway. This involves a comprehensive set of downscaled future climate data, of high relevance also for many other applications. Although the projections show large differences between the downscaled climate models, highlighting the large future climate uncertainty in this region, the data is still of value to structural planners as some areas show significant and robust changes. For example, Statnett might use this information to select potential critical areas to install monitoring equipment, to register loads over time and evaluate the necessity of upgrading existing lines. However, it has been made clear here that more work is needed to better understand model biases and uncertainties of climate projections in this region, and possibly to downscale more climate models.

The work of this thesis also contributes to improve our understanding of regional climate model responses, and particularly of precipitation. To the best of the author's knowledge, this work is

the first to associate the projected warming deficit in the North Atlantic (the NAWH) with changes in precipitation types such as a substantial reduction in convective precipitation, and to highlight the significant impact this has on winter total precipitation in northeastern Europe. These findings are based on an extreme model representation of the NAWH, however, still serves as a warning of potentially severe societal consequences for the region to be further investigated, and for the climate projections to be better constrained.

References

Admirat, P. (2008). Wet snow accretion on overhead lines. In *Atmospheric icing of power networks* (pp. 119-169). Springer.

Azad, R., & Sorteberg, A. (2017). Extreme daily precipitation in coastal western Norway and the link to atmospheric rivers. *J. Geophys. Res. Atmos.*, *122*, 2080-2095. https://doi.org/10.1002/2016jd025615

Ban, N., Caillaud, C., Coppola, E., Pichelli, E., Sobolowski, S., Adinolfi, M., Ahrens, B., Alias, A., Anders, I., Bastin, S., Belušić, D., Berthou, S., Brisson, E., Cardoso, R. M., Chan, S. C., Christensen, O. B., Fernández, J., Fita, L., Frisius, T., . . . Zander, M. J. (2021). The first multi-model ensemble of regional climate simulations at kilometer-scale resolution, part I: evaluation of precipitation. *Climate Dynamics*, *57*(1), 275-302. https://doi.org/10.1007/s00382-021-05708-w

Ban, N., Schmidli, J., & Schär, C. (2014). Evaluation of the convection-resolving regional climate modeling approach in decade-long simulations. *Journal of Geophysical Research: Atmospheres*, *119*(13), 7889-7907. https://doi.org/10.1002/2014JD021478

Barnett, T. P., Pierce, D. W., Hidalgo, H. G., Bonfils, C., Santer, B. D., Das, T., Bala, G., Wood, A. W., Nozawa, T., & Mirin, A. A. (2008). Human-induced changes in the hydrology of the western United States. *Science*, *319*(5866), 1080-1083.

Bauer, P., Thorpe, A., & Brunet, G. (2015). The quiet revolution of numerical weather prediction. *Nature*, *525*(7567), 47-55. https://doi.org/10.1038/nature14956

Benedict, J. J., Lee, S., & Feldstein, S. B. (2004). Synoptic View of the North Atlantic Oscillation. *Journal of the Atmospheric Sciences*, *61*(2), 121-144. https://doi.org/10.1175/1520-0469(2004)061<0121:Svotna>2.0.Co;2

Berthou, S., Kendon, E. J., Chan, S. C., Ban, N., Leutwyler, D., Schär, C., & Fosser, G. (2020). Pan-European climate at convection-permitting scale: a model intercomparison study. *Climate Dynamics*, *55*(1), 35-59.

Birch, C. E., Roberts, M. J., Garcia-Carreras, L., Ackerley, D., Reeder, M. J., Lock, A. P., & Schiemann, R. (2015). Sea-Breeze Dynamics and Convection Initiation: The Influence of Convective Parameterization in Weather and Climate Model Biases. *Journal of Climate*, *28*(20), 8093-8108. https://doi.org/10.1175/jcli-d-14-00850.1

Bjerknes, J. (1922). Life cycle of cyclones and the polar front theory of atmospheric circulation. *Geophys. Publik.*, *3*(1), 1-18.

Bjerknes, V. (1904). The problem of weather prediction, as seen from the standpoints of mechanics and physics. *Meteorologische Zeitschrif, 21, 1, 7*.

Brayshaw, D. J., Hoskins, B., & Blackburn, M. (2008). The Storm-Track Response to Idealized SST Perturbations in an Aquaplanet GCM. *Journal of the Atmospheric Sciences*, *65*(9), 2842-2860. https://doi.org/10.1175/2008jas2657.1

Bromwich, D. H. (2004). Polar Lows: Mesoscale Weather Systems in the Polar Regions. In: Wiley Online Library.

Brown, B. R., Bell, M. M., & Frambach, A. J. (2016). Validation of simulated hurricane drop size distributions using polarimetric radar. *Geophys. Res. Lett.*, *43*, 910-917.

Browning, K. A. (1990). Organization of clouds and precipitation in extratropical cyclones. In *Extratropical cyclones* (pp. 129-153). Springer.

Brümmer, B. (1997). Boundary layer mass, water, and heat budgets in wintertime cold-air outbreaks from the Arctic sea ice. *Mon. Wea. Rev.*, *125*, 1824-1837. https://doi.org/10.1175/1520-0493(1997)125<1824:Blmwah>2.0.Co;2

Brümmer, B. (1999). Roll and cell convection in wintertime Arctic cold-air outbreaks. *Journal of Atmospheric Sciences*, *56*, 2613-2636. https://doi.org/10.1175/1520-0469(1999)056<2613:Racciw>2.0.Co;2

Buckley, M. W., & Marshall, J. (2016). Observations, inferences, and mechanisms of the Atlantic Meridional Overturning Circulation: A review. *Reviews of Geophysics*, *54*(1), 5-63. https://doi.org/10.1002/2015RG000493

Bulygina, O. N., Arzhanova, N. M., & Groisman, P. Y. (2015). Icing conditions over Northern Eurasia in changing climate. *Environmental Research Letters*, *10*(2), 025003. https://doi.org/10.1088/1748-9326/10/2/025003

Caesar, L., Rahmstorf, S., Robinson, A., Feulner, G., & Saba, V. (2018). Observed fingerprint of a weakening Atlantic Ocean overturning circulation. *Nature*, *556*(7700), 191-196. https://doi.org/10.1038/s41586-018-0006-5

Cai, Z., You, Q., Wu, F., Chen, H. W., Chen, D., & Cohen, J. (2021). Arctic Warming Revealed by Multiple CMIP6 Models: Evaluation of Historical Simulations and Quantification of Future Projection Uncertainties. *Journal of Climate*, *34*(12), 4871-4892. https://doi.org/10.1175/jcli-d-20-0791.1

Catto, J. L., Jakob, C., Berry, G., & Nicholls, N. (2012). Relating global precipitation to atmospheric fronts. *Geophysical Research Letters*, *39*(10). https://doi.org/10.1029/2012GL051736

Chan, S. C., Kendon, E. J., Fowler, H. J., Blenkinsop, S., Ferro, C. A., & Stephenson, D. B. (2013). Does increasing the spatial resolution of a regional climate model improve the simulated daily precipitation? *Climate Dynamics*, *41*(5), 1475-1495.

Chang, S. E., McDaniels, T. L., Mikawoz, J., & Peterson, K. (2007). Infrastructure failure interdependencies in extreme events: power outage consequences in the 1998 Ice Storm. *Natural Hazards*, *41*(2), 337-358.

Charney, J. (1947). The Dynamics of Long Waves in a Baroclinic. *Westerly Current, J. Meteorol*, *4*.

Chen, F., & Dudhia, J. (2001). Coupling an Advanced Land Surface–Hydrology Model with the Penn State–NCAR MM5 Modeling System. Part I: Model Implementation and Sensitivity. *Monthly Weather Review*, *129*(4), 569-585. https://doi.org/10.1175/1520-0493(2001)129<0569:Caalsh>2.0.Co;2

Chiacchio, M., & Wild, M. (2010). Influence of NAO and clouds on long-term seasonal variations of surface solar radiation in Europe. *Journal of Geophysical Research: Atmospheres*, *115*(D10). https://doi.org/10.1029/2009JD012182

Coiffier, J. (2011). Half a century of numerical weather prediction. In J. Coiffier (Ed.), *Fundamentals of Numerical Weather Prediction* (pp. 1-14). Cambridge University Press. https://doi.org/DOI: 10.1017/CBO9780511734458.005

Colbeck, S., & Ackley, S. (1982). Mechanisms for ice bonding in wet snow accretions on power lines. Proceedings of the 1st International Workshop on Atmospheric Icing-IWAIS,

Colle, B. A., Garvert, M. F., Wolfe, J. B., & Mass, C. F. (2005). The 13–14 December 2001 IMPROVE-2 Event. Part III: Simulated Microphysical Budgets and Sensitivity Studies. *Journal of Atmospheric Sciences*, *62*, 3535–3558.

Dacre, H. F., Clark, P. A., Martinez-Alvarado, O., Stringer, M. A., & Lavers, D. A. (2015). How do atmospheric rivers form? *Bulletin of the American Meteorological Society*, *96*(8), 1243-1255.

Danabasoglu, G., Lamarque, J.-F., Bacmeister, J., Bailey, D. A., DuVivier, A. K., Edwards, J., Emmons, L. K., Fasullo, J., Garcia, R., Gettelman, A., Hannay, C., Holland, M. M., Large, W. G., Lauritzen, P. H., Lawrence, D. M., Lenaerts, J. T. M., Lindsay, K., Lipscomb, W. H., Mills, M. J., . . . Strand, W. G. (2020). The Community Earth System Model Version 2 (CESM2). *Journal of Advances in Modeling Earth Systems*, *12*(2), e2019MS001916. https://doi.org/10.1029/2019MS001916

Déqué, M., Rowell, D. P., Lüthi, D., Giorgi, F., Christensen, J. H., Rockel, B., Jacob, D., Kjellström, E., de Castro, M., & van den Hurk, B. (2007). An intercomparison of regional climate simulations for Europe: assessing uncertainties in model projections. *Climatic Change*, *81*(1), 53-70. https://doi.org/10.1007/s10584-006-9228-x

Dettinger, M., Udall, B., & Georgakakos, A. (2015). Western water and climate change. *Ecological Applications*, *25*(8), 2069-2093.

Ding, B., Yang, K., Qin, J., Wang, L., Chen, Y., & He, X. (2014). The dependence of precipitation types on surface elevation and meteorological conditions and its parameterization. *J. Hydrol.*, *513*, 154-163.

Dirmeyer, P. A., Cash, B. A., Kinter, J. L., Jung, T., Marx, L., Satoh, M., Stan, C., Tomita, H., Towers, P., Wedi, N., Achuthavarier, D., Adams, J. M., Altshuler, E. L., Huang, B., Jin, E. K., & Manganello, J. (2012). Simulating the diurnal cycle of rainfall in global climate models:

resolution versus parameterization. *Climate Dynamics*, *39*(1), 399-418. https://doi.org/10.1007/s00382-011-1127-9

Drijfhout, S., van Oldenborgh, G. J., & Cimatoribus, A. (2012). Is a decline of AMOC causing the warming hole above the North Atlantic in observed and modeled warming patterns? *J. Climate*, *29*, 2359–2373.

Eady, E. T. (1949). Long waves and cyclone waves. *Tellus*, *1*(3), 33-52.

El-Samra, R., Bou-Zeid, E., Bangalath, H. K., Stenchikov, G., & El-Fadel, M. (2017). Future intensification of hydro-meteorological extremes: downscaling using the weather research and forecasting model. *Climate Dynamics*, *49*(11), 3765-3785. https://doi.org/10.1007/s00382-017-3542-z

Elíasson, Á. J., Ísaksson, S. P., Ágústsson, H., & Thorsteins, E. (2015). Wet-snow icing: Comparing simulated accretion with observational experience. Int. Workshop on Atmospheric Icing of Structures, Uppsala.

Evans, J., Ji, F., Lee, C., Smith, P., Argüeso, D., & Fita, L. (2014). Design of a regional climate modelling projection ensemble experiment–NARCliM. *Geoscientific Model Development*, *7*(2), 621-629.

Eyring, V., Bony, S., Meehl, G. A., Senior, C. A., Stevens, B., Stouffer, R. J., & Taylor, K. E. (2016). Overview of the Coupled Model Intercomparison Project Phase 6 (CMIP6) experimental design and organization. *Geosci. Model Dev.*, *9*(5), 1937-1958. https://doi.org/10.5194/gmd-9-1937-2016

Fabry, F., & Zawadzki, I. (1995). Long-term radar observations of the melting layer of precipitation and their interpretation. *Journal of Atmospheric Sciences*, *52*, 838–851.

Faggian, P., Decimi, G., Ciapessoni, E., Marzullo, F., & Scavo, F. (2021, 4-8 Oct. 2021). Future projections and return levels of wet-snow load on overhead lines and heavy snowfalls. 2021 AEIT International Annual Conference (AEIT),

Field, P. R., Brožková, R., Chen, M., Dudhia, J., Lac, C., Hara, T., Honnert, R., Olson, J., Siebesma, P., & de Roode, S. (2017). Exploring the convective grey zone with regional simulations of a cold air outbreak. *Quarterly Journal of the Royal Meteorological Society*, *143*(707), 2537-2555.

Fikke, S. M., Kristjánsson, J. E., & Kringlebotn Nygaard, B. E. (2008). Modern Meteorology and Atmospheric Icing. In M. Farzaneh (Ed.), *Atmospheric Icing of Power Networks* (pp. 1-29). Springer Netherlands. https://doi.org/10.1007/978-1-4020-8531-4_1

Finstad, K. J., Lozowski, E. P., & Makkonen, L. (1988). On the Median Volume Diameter Approximation for Droplet Collision Efficiency. *Journal of Atmospheric Sciences*, *45*(24), 4008-4012. https://doi.org/10.1175/1520-0469(1988)045<4008:Otmvda>2.0.Co;2

Fosser, G., Khodayar, S., & Berg, P. (2015). Benefit of convection permitting climate model simulations in the representation of convective precipitation. *Climate Dynamics*, *44*(1), 45-60. https://doi.org/10.1007/s00382-014-2242-1

Fox-Kemper, B., H.T. Hewitt, C. Xiao, G. Aðalgeirsdóttir, S.S. Drijfhout, T.L. Edwards, N.R. Golledge, M. Hemer, R.E. Kopp, G. Krinner, A. Mix, D. Notz, S. Nowicki, I.S. Nurhati, L. Ruiz, J.-B. Sallée, A.B.A. Slangen, & Yu, Y. (2021). Ocean, Cryosphere and Sea Level Change. . In V. Masson-Delmotte, P. Zhai, A. Pirani, S.L. Connors, C. Péan, S. Berger, N. Caud, Y. Chen, L. Goldfarb, M.I. Gomis, M. Huang, K. Leitzell, E. Lonnoy, J.B.R. Matthews, T.K. Maycock, T. Waterfield, O. Yelekçi, R. Yu, & B. Zhou (Eds.), *Climate Change 2021: The Physical Science Basis. Contribution of Working Group I to the Sixth Assessment Report of the Intergovernmental Panel on Climate Change* (pp. pp. 1211–1362). Cambridge University Press. https://doi.org/10.1017/9781009157896.011.

Gervais, M., Shaman, J., & Kushnir, Y. (2019). Impacts of the North Atlantic Warming Hole in Future Climate Projections: Mean Atmospheric Circulation and the North Atlantic Jet. *Journal of Climate*, *32*(10), 2673-2689. https://doi.org/10.1175/jcli-d-18-0647.1

Gervais, M., Shaman, J., & Kushnir, Y. (2020). Impact of the North Atlantic Warming Hole on Sensible Weather. *Journal of Climate*, *33*(10), 4255-4271. https://doi.org/10.1175/jcli-d-19-0636.1

Ghil, M., & Malanotte-Rizzoli, P. (1991). Data Assimilation in Meteorology and Oceanography. In R. Dmowska & B. Saltzman (Eds.), *Advances in Geophysics* (Vol. 33, pp. 141-266). Elsevier. https://doi.org/10.1016/S0065-2687(08)60442-2

Giorgi, F., & Gutowski Jr, W. J. (2015). Regional dynamical downscaling and the CORDEX initiative. *Annual review of environment and resources*, *40*, 467-490.

Gutowski Jr, W. J., Giorgi, F., Timbal, B., Frigon, A., Jacob, D., Kang, H.-S., Raghavan, K., Lee, B., Lennard, C., & Nikulin, G. (2016). WCRP coordinated regional downscaling experiment (CORDEX): a diagnostic MIP for CMIP6. *Geoscientific Model Development*, *9*(11), 4087-4095.

Haldar, A. (2016). *Rime Icing Model Validation Using WRF and Full Scale Field Icing Data*.

Hall, R., Erdélyi, R., Hanna, E., Jones, J. M., & Scaife, A. A. (2015). Drivers of North Atlantic Polar Front jet stream variability. *International Journal of Climatology*, *35*(8), 1697-1720. https://doi.org/https://doi.org/10.1002/joc.4121

Hand, R., Keenlyside, N. S., Omrani, N.-E., Bader, J., & Greatbatch, R. J. (2019). The role of local sea surface temperature pattern changes in shaping climate change in the North Atlantic sector. *Climate Dynamics*, *52*(1), 417-438.

Harder, P., & Pomeroy, J. (2013). Estimating precipitation phase using a psychrometric energy balance method. *Hydrol. Process.*, *27*, 1901-1914.

Held, I. M., & Soden, B. J. (2006). Robust responses of the hydrological cycle to global warming. *Journal of Climate*, *19*(21), 5686-5699.

Hersbach, H., de Rosnay, P., Bell, B., Schepers, D., Simmons, A. J., Willett, K. M., Jones, P. D., Thorne, P. W., Dee, D. P., Soci, C., Abdalla, S., Alonso-Balmaseda, M. B., G. , Bechtold, P., Berrisford, P., Bidlot, J.-R., de Boisséson, E., Bonavita, M., Browne, P., Buizza, R., . . . Zuo, H. (2018). *Operational global reanalysis: progress, future directions and synergies with NWP*. https://www.ecmwf.int/node/18765

Hewitt, C., & Griggs, D. (2004). Ensembles-based predictions of climate changes and their impacts (ENSEMBLES). *EOS*, *85*, 566. https://doi.org/10.1029/2004EO520005

Hohenegger, C., Brockhaus, P., & Schar, C. (2008). Towards climate simulations at cloud-resolving scales. *Meteorologische Zeitschrift*, *17*(4), 383-394.

Hohenegger, C., Schlemmer, L., & Silvers, L. (2015). Coupling of convection and circulation at various resolutions. *Tellus A: Dynamic Meteorology and Oceanography*, *67*(1), 26678. https://doi.org/10.3402/tellusa.v67.26678

Hoskins, B. J., James, I. N., & White, G. H. (1983). The shape, propagation and mean-flow interaction of large-scale weather systems. *Journal of Atmospheric Sciences*, *40*(7), 1595-1612.

Hoskins, B. J., & Valdes, P. J. (1990). On the existence of storm-tracks. *Journal of Atmospheric Sciences*, *47*(15), 1854-1864.

Houze Jr., R. A. (1981). Structures of atmospheric precipitation systems: A global survey. *Radio Science*, *16*(5), 671-689. https://doi.org/10.1029/RS016i005p00671

Houze Jr., R. A. (1993). *Cloud Dynamics*. Academic Press.

Houze, R. A. (2014). Chapter 6 - Nimbostratus and the Separation of Convective and Stratiform Precipitation. In R. A. Houze (Ed.), *International Geophysics* (Vol. 104, pp. 141-163). Academic Press. https://doi.org/10.1016/B978-0-12-374266-7.00006-8

Houze, R. A., McMurdie, L. A., Peterson, W. A., Schwaller, M. R., Baccus, W., Lundquist, J. D., Mass, C. F., Nijssen, B., Rutledge, S. A., Hudak, D. R., Tanelli, S., Mace, G. G., Poellot, M. R., Lettenmaier, D. P., Zagrodnik, J. P., Rowe, A. K., DeHart, J. C., Madaus, L. E., Barnes, H. C., & Chandrasekar, V. (2017). The Olympic Mountains Experiment (OLYMPEX). *Bull. Amer. Meteor. Soc.*, *98*, 2167-2188.

Hurrell, J. W., Kushnir, Y., Ottersen, G., & Visbeck, M. (2003). An Overview of the North Atlantic Oscillation. In *The North Atlantic Oscillation: Climatic Significance and Environmental Impact* (pp. 1-35). https://doi.org/10.1029/134GM01

Iacono, M. J., Delamere, J. S., Mlawer, E. J., Shephard, M. W., Clough, S. A., & Collins, W. D. (2008). Radiative forcing by long-lived greenhouse gases: Calculations with the AER radiative transfer models. *Journal of Geophysical Research*, *113*(D13103).

Inatsu, M., Mukougawa, H., & Xie, S.-P. (2003). Atmospheric response to zonal variations in midlatitude SST: Transient and stationary eddies and their feedback. *Journal of Climate*, *16*(20), 3314-3329.

Ingvaldsen, K., Nygaard, B. E., Byrkjedal, Ø., & Iversen, E. C. (2019, June 23-28). *Validation of Modelled In-cloud Ice Accretion on Overhead Power Lines at Exposed High Altitude Sites in Norway* Int. Workshop on Atmospheric Icing of Structures, Reykjavik, Iceland.

Isachsen, P., Drivdal, M., Eastwood, S., Gusdal, Y., Noer, G., & Saetra, Ø. (2013). Observations of the ocean response to cold air outbreaks and polar lows over the Nordic Seas. *Geophysical Research Letters*, *40*(14), 3667-3671.

ISO. (2017). Atmospheric icing on structures In (Vol. 12494).

Iversen, E. C., & Burningham, H. (2015). Relationship between NAO and wind climate over Norway. *Clim. Res.*, *63*, 115-134.

Jackson, L. C., Peterson, K. A., Roberts, C. D., & Wood, R. A. (2016). Recent slowing of Atlantic overturning circulation as a recovery from earlier strengthening. *Nature Geoscience*, *9*(7), 518-522. https://doi.org/10.1038/ngeo2715

Jeong, D. I., Cannon, A. J., & Zhang, X. (2019). Projected changes to extreme freezing precipitation and design ice loads over North America based on a large ensemble of Canadian regional climate model simulations. *Nat. Hazards Earth Syst. Sci.*, *19*(4), 857-872. https://doi.org/10.5194/nhess-19-857-2019

Keil, P., Mauritsen, T., Jungclaus, J., Hedemann, C., Olonscheck, D., & Ghosh, R. (2020). Multiple drivers of the North Atlantic warming hole. *Nature Climate Change*, *10*(7), 667-671. https://doi.org/10.1038/s41558-020-0819-8

Kendon, E. J., Roberts, N. M., Fosser, G., Martin, G. M., Lock, A. P., Murphy, J. M., Senior, C. A., & Tucker, S. O. (2020). Greater Future U.K. Winter Precipitation Increase in New Convection-Permitting Scenarios. *Journal of Climate*, *33*(17), 7303-7318. https://doi.org/10.1175/jcli-d-20-0089.1

Kendon, E. J., Roberts, N. M., Senior, C. A., & Roberts, M. J. (2012). Realism of Rainfall in a Very High-Resolution Regional Climate Model. *Journal of Climate*, *25*(17), 5791-5806. https://doi.org/10.1175/jcli-d-11-00562.1

Kendon, E. J., Stratton, R. A., Tucker, S., Marsham, J. H., Berthou, S., Rowell, D. P., & Senior, C. A. (2019). Enhanced future changes in wet and dry extremes over Africa at convection-permitting scale. *Nature communications*, *10*(1), 1-14.

Kessler, E. (1969). On the distribution and continuity of water substance in atmospheric circulations. In *On the distribution and continuity of water substance in atmospheric circulations* (pp. 1-84). Springer.

Kirshbaum, D. J., Adler, B., Kalthoff, N., Barthlott, C., & Serafin, S. (2018). Moist orographic convection: Physical mechanisms and links to surface-exchange processes. *Atmosphere*, *9*(3), 80.

Kleppe, L. (1984). *Description of icing cases leading to tower collapse on the 300 kV electric power line Dale - Fana* Int. Workshop on Atmospheric Icing of Structures, Trondheim, Norway.

Knippertz, P., & Wernli, H. (2010). A Lagrangian climatology of tropical moisture exports to the Northern Hemispheric extratropics. *Journal of Climate*, *23*(4), 987-1003.

Knist, S., Goergen, K., & Simmer, C. (2020). Evaluation and projected changes of precipitation statistics in convection-permitting WRF climate simulations over Central Europe. *Climate Dynamics*, *55*(1), 325-341.

Knutti, R., Masson, D., & Gettelman, A. (2013). Climate model genealogy: Generation CMIP5 and how we got there. *Geophysical Research Letters*, *40*(6), 1194-1199.

Kolstad, E. W. (2017). Higher ocean wind speeds during marine cold air outbreaks. *Quarterly Journal of the Royal Meteorological Society*, *143*(706), 2084-2092.

Kolstad, E. W., Bracegirdle, T. J., & Seierstad, I. A. (2009). Marine cold-air outbreaks in the North Atlantic: temporal distribution and associations with large-scale atmospheric circulation. *Climate Dynamics*, *33*(2), 187-197. https://doi.org/10.1007/s00382-008-0431-5

Kruschke, T., Rust, H. W., Kadow, C., Müller, W. A., Pohlmann, H., Leckebusch, G. C., & Ulbrich, U. (2015). Probabilistic evaluation of decadal prediction skill regarding Northern Hemisphere winter storms.

Kuettner, J. (1959). The Band Structure of the Atmosphere. *Tellus*, *11*(3), 267-294. https://doi.org/10.3402/tellusa.v11i3.9319

Lavers, D. A., & Villarini, G. (2013). The nexus between atmospheric rivers and extreme precipitation across Europe. *Geophysical Research Letters*, *40*(12), 3259-3264. https://doi.org/10.1002/grl.50636

Leutwyler, D., Fuhrer, O., Lapillonne, X., Lüthi, D., & Schär, C. (2016). Towards European-scale convection-resolving climate simulations with GPUs: A study with COSMO 4.19. *Geoscientific Model Development*, *9*(9), 3393-3412.

Li, Q., Fan, Z., Wu, Q., Gao, J., Su, Z., & Zhou, W.-j. (2008). Investigation of ice-covered transmission lines and analysis on transmission line failures caused by ice-coating in China. *Power System Technology*, *32*(9), 33-36.

Li, Y., Li, Z., Zhang, Z., Chen, L., Kurkute, S., Scaff, L., & Pan, X. (2019). High-resolution regional climate modeling and projection over western Canada using a weather research forecastingmodel with a pseudo-global warming approach. *Hydrol. Earth Syst. Sci.*, *23*, 4635–4659.

Lind, P., Belušić, D., Christensen, O. B., Dobler, A., Kjellström, E., Landgren, O., Lindstedt, D., Matte, D., Pedersen, R. A., Toivonen, E., & Wang, F. (2020). Benefits and added value of convection-permitting climate modeling over Fenno-Scandinavia. *Climate Dynamics*, *55*(7), 1893-1912. https://doi.org/10.1007/s00382-020-05359-3

Liu, C., Ikeda, K., Rasmussen, R., Barlage, M., Newman, A. J., Prein, A. F., Chen, F., Chen, L., Clark, M., Dai, A., Dudhia, J., Eidhammer, T., Gochis, D., Gutmann, E., Kurkute, S., Li, Y., Thompson, G., & Yates, D. (2017). Continental-scale convection-permitting modeling of the current and future climate of North America. *Clim. Dyn.*, *49*, 71–95.

Liu, C., Ikeda, K., Thompson, G., Rasmussen, R., & Dudhia, J. (2011). High-resolution simulations of wintertime precipitation in the Colorado Headwaters region: Sensitivity to physics parameterizations. *Monthly Weather Review*, *139*(11), 3533-3553.

Liu, W., Fedorov, A. V., Xie, S.-P., & Hu, S. (2020). Climate impacts of a weakened Atlantic Meridional Overturning Circulation in a warming climate. *Science Advances*, *6*(26), eaaz4876. https://doi.org/doi:10.1126/sciadv.aaz4876

Makkonen, L. (1989). Estimation of wet snow accreation on structures. *Cold Reg. Sci. Tech.*, *17*, 83-88.

Makkonen, L. (2000). Models for the growth of rime, glaze, icicles and wet snow on structures. *Philosophical Transactions of the Royal Society of London. Series A: Mathematical, Physical and Engineering Sciences*, *358*(1776), 2913-2939.

Makkonen, L., & Wichura, B. (2010). Simulating wet snow loads on power line cables by a simple model. *Cold Regions Science and Technology*, *61*(2-3), 73-81.

Mansfield, D. (1974). Polar lows: The development of baroclinic disturbances in cold air outbreaks. *Quarterly Journal of the Royal Meteorological Society*, *100*(426), 541-554.

Mearns, L. O., Gutowski, W., Jones, R., Leung, R., McGinnis, S., Nunes, A., & Qian, Y. (2009). A Regional Climate Change Assessment Program for North America. *Eos, Transactions American Geophysical Union*, *90*(36), 311-311. https://doi.org/10.1029/2009EO360002

Meredith, E. P., Maraun, D., Semenov, V. A., & Park, W. (2015). Evidence for added value of convection-permitting models for studying changes in extreme precipitation. *Journal of Geophysical Research: Atmospheres*, *120*(24), 12500-12513. https://doi.org/10.1002/2015JD024238

Milbrandt, J. A., & Yau, M. K. (2005). A multi-moment bulk microphysics parameterization. Part II: A proposed three-moment closure and scheme description. *J. Atmos. Sci.*, *62*, 3065-3081.

Morrison, H., & Milbrandt, A. (2015). Parameterization of cloud microphysics based on the prediction of the bulk ice particle properties. Part I: Scheme description and idealized tests. *Journal of Atmospheric Sciences*, *72*, 287-311.

Murphy, J., Sexton, D., Jenkins, G., Boorman, P., Booth, B., Brown, K., Clark, R., Collins, M., Harris, G., Kendon, E., Betts, R., Brown, S., Hinton, T., Howard, T., McDonald, R., McCarthy, M., Wood, R., Humphrey, K., Stephens, A., & Wilby, R. (2010). Climate Change Projections for the UK (UKCP09). *AGU Fall Meeting Abstracts*.

Müller, W. A., Jungclaus, J. H., Mauritsen, T., Baehr, J., Bittner, M., Budich, R., Bunzel, F., Esch, M., Ghosh, R., Haak, H., Ilyina, T., Kleine, T., Kornblueh, L., Li, H., Modali, K., Notz, D., Pohlmann, H., Roeckner, E., Stemmler, I., . . . Marotzke, J. (2018). A Higher-resolution Version of the Max Planck Institute Earth System Model (MPI-ESM1.2-HR). *Journal of Advances in Modeling Earth Systems*, *10*(7), 1383-1413. https://doi.org/10.1029/2017ms001217

Nakamura, H., Sampe, T., Tanimoto, Y., & Shimpo, A. (2004). Observed associations among storm tracks, jet streams and midlatitude oceanic fronts. *Earth's Climate: The Ocean–Atmosphere Interaction, Geophys. Monogr*, *147*, 329-345.

Nakanishi, M., & Niino, H. (2006). An Improved Mellor–Yamada Level-3 Model: Its Numerical Stability and Application to a Regional Prediction of Advection Fog. *Boundary-Layer Meteorol.*, *119*(2), 397-407.

Nygaard, B. E., Byrkjedal, Ø., Iversen, E., Fredbo, M., Ágústsson, H., & Welgaard, Ø. (2017a). *Development of a reliable modeling system for the calculation of rime ice loads on overhead transmission lines* Int. Workshop on Atmospheric Icing of Structures,

Nygaard, B. E., Fikke, S. M., & Makkonen, L. (2017b). *State of the art report on designing transmission lines for wet snow accumulation*.

Nygaard, B. E., Ingvaldsen, K., & Welgaard, Ø. (2022, June 19-23). *Development of Ice Load Maps for Structural Design* Int. Workshop on Atmospheric Icing of Structures, Montreal, Canada.

Nygaard, B. E., Kristjánsson, J. E., & Makkonen, L. (2011). Prediction of In-Cloud Icing Conditions at Ground Level Using the WRF Model. *J. Appl. Meteor. Climatol.*, *50*, 2445-2459.

Nygaard, B. E. K. (2013). *Modelling atmospheric icing of structures using high resolution numerical weather prediction models* University of Oslo].

Nygaard, B. E. K., Ágústsson, H., & Somfalvi-Tóth, K. (2013). Modeling wet snow accretion on power lines: improvements to previous methods using 50 years of observations. *J. Appl. Meteor. and Climatol.*, *52*, 2189-2203.

O'Neill, B. C., Tebaldi, C., van Vuuren, D. P., Eyring, V., Friedlingstein, P., Hurtt, G., Knutti, R., Kriegler, E., Lamarque, J. F., Lowe, J., Meehl, G. A., Moss, R., Riahi, K., & Sanderson, B. M. (2016). The Scenario Model Intercomparison Project (ScenarioMIP) for CMIP6. *Geosci. Model Dev.*, *9*(9), 3461-3482. https://doi.org/10.5194/gmd-9-3461-2016

Ohba, M., & Sugimoto, S. (2020). Impacts of climate change on heavy wet snowfall in Japan. *Climate Dynamics*, *54*(5), 3151-3164. https://doi.org/10.1007/s00382-020-05163-z

Papritz, L., & Grams, C. M. (2018). Linking Low-Frequency Large-Scale Circulation Patterns to Cold Air Outbreak Formation in the Northeastern North Atlantic. *Geophysical Research Letters*, *45*(5), 2542-2553. https://doi.org/10.1002/2017GL076921

Papritz, L., & Sodemann, H. (2018). Characterizing the Local and Intense Water Cycle during a Cold Air Outbreak in the Nordic Seas. *Monthly Weather Review*, *146*(11), 3567-3588. https://doi.org/10.1175/mwr-d-18-0172.1

Papritz, L., & Spengler, T. (2017). A Lagrangian climatology of wintertime cold air outbreaks in the Irminger and Nordic seas and their role in shaping air–sea heat fluxes. *J. Climate*, *30*, 2717-2737. https://doi.org/10.1175/jcli-d-16-0605.1

Pavelsky, T. M., Kapnick, S., & Hall, A. (2011). Accumulation and melt dynamics of snowpack from a multiresolution regional climate model in the central Sierra Nevada, California. *Journal of Geophysical Research*, *116*, D16115. https://doi.org/10.1029/2010jd015479

Pearson, K. J., Lister, G. M. S., Birch, C. E., Allan, R. P., Hogan, R. J., & Woolnough, S. J. (2014). Modelling the diurnal cycle of tropical convection across the 'grey zone'. *Quarterly Journal of the Royal Meteorological Society*, *140*(679), 491-499. https://doi.org/10.1002/qj.2145

Podolskiy, E. A., Nygaard, B. E. K., Nishimura, K., Makkonen, L., & Lozowski, E. P. (2012). Study of unusual atmospheric icing at Mount Zao, Japan, using the Weather Research and Forecasting model. *Journal of Geophysical Research: Atmospheres*, *117*(D12).

Prein, A. F., Langhans, W., Fosser, G., Ferrone, A., Ban, N., Goergen, K., Keller, M., Tölle, M., Gutjahr, O., Feser, F., Brisson, E., Kollet, S., Schmidli, J., van Lipzig, N. P. M., & Leung, R. (2015). A review on regional convection-permitting climate modeling: Demonstrations, prospects, and challenges. *Reviews of Geophysics*, *53*(2), 323-361. https://doi.org/10.1002/2014RG000475

Prein, A. F., Liu, C., Ikeda, K., Bullock, R., Rasmussen, R. M., Holland, G. J., & Clark, M. (2020). Simulating North American mesoscale convective systems with a convection-permitting climate model. *Climate Dynamics*, *55*(1), 95-110. https://doi.org/10.1007/s00382-017-3993-2

Pruppacher, H. R., & Klett, J. D. (1997). *Microphysics of Clouds and Precipitation*. Kluwer Academic Publishers.

Rahmstorf, S. (1995). Bifurcations of the Atlantic thermohaline circulation in response to changes in the hydrological cycle. *Nature*, *378*(6553), 145-149. https://doi.org/10.1038/378145a0

Rahmstorf, S., Box, J. E., Feulner, G., Mann, M. E., Robinson, A., Rutherford, S., & Schaffernicht, E. J. (2015). Exceptional twentieth-century slowdown in Atlantic Ocean overturning circulation. *Nature Climate Change*, *5*(5), 475-480. https://doi.org/10.1038/nclimate2554

Ramos, A. M., Nieto, R., Tomé, R., Gimeno, L., Trigo, R. M., Liberato, M. L. R., & Lavers, D. A. (2016). Atmospheric rivers moisture sources from a Lagrangian perspective. *Earth Syst. Dynam.*, *7*(2), 371-384. https://doi.org/10.5194/esd-7-371-2016

Ranasinghe, R., Ruane, A. C., Vautard, R., Arnell, N., Coppola, E., Cruz, F. A., Dessai, S., Islam, A. S., Rahimi, M., Ruiz Carrascal, D., Sillmann, J., Sylla, M. B., Tebaldi, C., Wang, W., & Zaaboul, R. (2021). *Climate Change Information for Regional Impact and for Risk Assessment Supplementary Material* (Climate Change 2021: The Physical Science Basis. Contribution of Working Group I to the Sixth Assessment Report of the Intergovernmental Panel on Climate Change, Issue. IPCC. http://www.ipcc.ch

Rasmussen, R., Liu, C., Ikeda, K., Gochis, D., Yates, D., Chen, F., Tewari, M., Barlage, M., Dudhia, J., Yu, W., Miller, K., Arsenault, K., Grubisic, V., Thompson, G., & Gutmann, E. (2011). High-Resolution Coupled Climate Runoff Simulations of Seasonal Snowfall over Colorado: A Process Study of Current and Warmer Climate. *J. Climate*, *24*, 3015–3048.

Rhoades, A. M., Ullrich, P. A., Zarzycki, C. M., Johansen, H., Margulis, S. A., Morrison, H., Xu, Z., & Collins, W. D. (2018). Sensitivity of Mountain Hydroclimate Simulations in Variable-Resolution CESM to Microphysics and Horizontal Resolution. *Journal of Advances in Modeling Earth Systems*, *10*(6), 1357-1380. https://doi.org/10.1029/2018MS001326

Riahi, K., & al., e. (2017). The Shared Socioeconomic Pathways and their energy, land use, and greenhouse gas emissions implications: An overview. *Glob. Env. Change*, *42*, 153-168.

Rögnvaldsson, Ó., Bao, J. W., Ágústsson, H., & Ólafsson, H. (2011). Downslope windstorm in Iceland – WRF/MM5 model comparison. *Atmos. Chem. Phys.*, *11*(1), 103-120. https://doi.org/10.5194/acp-11-103-2011

Rögnvaldsson, Ó., & Ólafsson, H. (2005). OROGRAPHIC IMPACT ON THE PREDICTED CHANGE IN THE FREQUENCY OF CONDITIONS FOR WET SNOW ICING IN FUTURE CLIMATE. *Hrvatski meteorološki časopis*, *40*(40), 713-716.

Sakamoto, Y. (2000). Snow accretion on overhead wires. *Philosophical Transactions of the Royal Society of London. Series A: Mathematical, Physical and Engineering Sciences*, *358*(1776), 2941-2970.

Sandvik, I. M., Sorteberg, A., & Rasmussen, R. (2018). Sensitivity of historical orographically enhanced extreme precipitation events to idealized temperature perturbations. *Clim. Dyn.*, *50*, 143-157.

Schmittner, A., Chiang, J. C. H., & Hemming, S. R. (2007). Introduction: The Ocean's Meridional Overturning Circulation. In *Ocean Circulation: Mechanisms and Impacts—Past and Future Changes of Meridional Overturning* (pp. 1-4). https://doi.org/10.1029/173GM02

Shepherd, T., Coburn, J. J., Barthelmie, R. J., & Pryor, S. C. (2022). Exploring ENSO-Induced Anomalies over North America in Historical and Future Climate Simulations That Use HadGEM2-ESM Output to Drive WRF. *Climate*, *10*(8), 117.

Siller, N., & Roe, G. (2014). How will orographic precipitation respond to surface warming? An idealized thermodynamic perspective. *Geophysical Research Letters*, *41*, 2606–2613.

Simpson, I. R., Bacmeister, J., Neale, R. B., Hannay, C., Gettelman, A., Garcia, R. R., Lauritzen, P. H., Marsh, D. R., Mills, M. J., Medeiros, B., Richter, J. H. (2020). An Evaluation of the Large-Scale Atmospheric Circulation and Its Variability in CESM2 and Other CMIP Models. *J. Geophys. Res.: Atmos.*, *125*, e2020JD032835.

Skamarock, W. C., Klemp, J. B., Dudhia, J., Gill, D. O., Liu, Z., Berner, J., Wang, W., Powers, J. G., Duda, M. G., Barker, D. M., & Huang, X.-Y. (2019). *A Description of the Advanced Research WRF Version 4*.

Sodemann, H. (2020). Beyond Turnover Time: Constraining the Lifetime Distribution of Water Vapor from Simple and Complex Approaches. *Journal of the Atmospheric Sciences*, *77*(2), 413-433. https://doi.org/10.1175/jas-d-18-0336.1

Sodemann, H., Wernli, H., Knippertz, P., Cordeira, J. M., Dominguez, F., Guan, B., Hu, H., Ralph, F. M., & Stohl, A. (2020). Structure, Process, and Mechanism. In F. M. Ralph, M. D. Dettinger, J. J. Rutz, & D. E. Waliser (Eds.), *Atmospheric Rivers* (pp. 15-43). Springer International Publishing. https://doi.org/10.1007/978-3-030-28906-5_2

Sokolov, P., & Virk, M. S. (2019). Droplet distribution spectrum effects on dry ice growth on cylinders. *Cold Regions Science and Technology*, *160*, 80-88. https://doi.org/10.1016/j.coldregions.2019.01.002

Stein, T. H., Parker, D. J., Hogan, R. J., Birch, C. E., Holloway, C. E., Lister, G. M., Marsham, J. H., & Woolnough, S. J. (2015). The representation of the West African monsoon vertical cloud structure in the Met Office Unified Model: An evaluation with CloudSat. *Quarterly Journal of the Royal Meteorological Society*, *141*(693), 3312-3324.

Stensrud, D. (2007). Convective parameterizations. In D. J. Stensrud (Ed.), *Parameterization Schemes: Keys to Understanding Numerical Weather Prediction Models* (pp. 185-259). Cambridge University Press. https://doi.org/DOI: 10.1017/CBO9780511812590.007

Stewart, R. E. (1992). Precipitation Types in the Transition Region of Winter Storms. *Bull. Amer. Meteor. Soc., 73*, 287-296.

Stocker, T. F., & Wright, D. G. (1991). Rapid transitions of the ocean's deep circulation induced by changes in surface water fluxes. *Nature*, *351*(6329), 729-732. https://doi.org/10.1038/351729a0

Stohl, A., Forster, C., & Sodemann, H. (2008). Remote sources of water vapor forming precipitation on the Norwegian west coast at 60°N–a tale of hurricanes and an atmospheric river. *Journal of Geophysical Research: Atmospheres*, *113*(D5). https://doi.org/10.1029/2007JD009006

Tang, S., Gleckler, P., Xie, S., Lee, J., Ahn, M.-S., Covey, C., & Zhang, C. (2021). Evaluating the Diurnal and Semidiurnal Cycle of Precipitation in CMIP6 Models Using Satellite- and Ground-Based Observations. *Journal of Climate*, *34*(8), 3189-3210. https://doi.org/10.1175/jcli-d-20-0639.1

Thompson, G., & Eidhammer, T. (2014). A Study of Aerosol Impacts on Clouds and Precipitation Development in a Large Winter Cyclone. *J. Atmos. Sci., 71*, 3636-3658.

Thompson, G., Field, P. R., Rasmussen, R. M., & Hall, W. D. (2008). Explicit Forecasts of Winter Precipitation Using an Improved Bulk Microphysics Scheme. Part II: Implementation of a New Snow Parameterization. *Mon. Wea. Rev., 136*, 5095-5115.

Thompson, G., Nygaard, B. E., Makkonen, L., & Dierer, S. (2009). Using the weather research and forecasting (WRF) model to predict ground/structural icing. Int. Workshop on Atmospheric Icing of Structures, Andermatt.

Thompson, G., Rasmussen, R. M., & Manning, K. (2004). Explicit Forecasts of Winter Precipitation Using an Improved Bulk Microphysics Scheme. Part I: Description and Sensitivity Analysis. *Mon. Wea. Rev., 132*, 519-542.

Thorsteins, E., Nygaard, B. E., Ingvaldsen, K., & Elíasson, Á. J. (2022). *Wet snow icing modeling and comparison with field data* Int. Workshop on Atmospheric Icing of Structures, Montreal, Canada.

Tomassini, L., Field, P. R., Honnert, R., Malardel, S., McTaggart-Cowan, R., Saitou, K., Noda, A. T., & Seifert, A. (2017). The “Grey Zone” cold air outbreak global model intercomparison: A cross evaluation using large-eddy simulations. *Journal of Advances in Modeling Earth Systems*, *9*(1), 39-64. https://doi.org/10.1002/2016MS000822

Trenberth, K. E. (1999). Atmospheric Moisture Recycling: Role of Advection and Local Evaporation. *Journal of Climate*, *12*(5), 1368-1381. https://doi.org/10.1175/1520-0442(1999)012<1368:Amrroa>2.0.Co;2

Trenberth, K. E., Dai, A., Rasmussen, R. M., & Parsons, D. B. (2003). The Changing Character of Precipitation. *Bulletin of the American Meteorological Society*, *84*(9), 1205-1218. https://doi.org/10.1175/bams-84-9-1205

Uvo, C. B. (2003). Analysis and regionalization of northern European winter precipitation based on its relationship with the North Atlantic oscillation. *Int. J. Climatol.*, *23*(10), 1185-1194.

Vallis, G. K., & Gerber, E. P. (2008). Local and hemispheric dynamics of the North Atlantic Oscillation, annular patterns and the zonal index. *Dynamics of atmospheres and oceans*, *44*(3-4), 184-212.

Vellinga, M., Roberts, M., Vidale, P. L., Mizielinski, M. S., Demory, M.-E., Schiemann, R., Strachan, J., & Bain, C. (2016). Sahel decadal rainfall variability and the role of model horizontal resolution. *Geophysical Research Letters*, *43*(1), 326-333. https://doi.org/10.1002/2015GL066690

Vergara-Temprado, J., Ban, N., Panosetti, D., Schlemmer, L., & Schär, C. (2020). Climate models permit convection at much coarser resolutions than previously considered. *Journal of Climate*, *33*(5), 1915-1933.

Viceto, C., Marta-Almeida, M., & Rocha, A. (2017). Future climate change of stability indices for the Iberian Peninsula. *International Journal of Climatology*, *37*(12), 4390-4408. https://doi.org/10.1002/joc.5094

Walko, R. L., Cotton, W. R., Meyers, M., & Harrington, J. (1995). New RAMS cloud microphysics parameterization part I: the single-moment scheme. *Atmospheric Research*, *38*(1-4), 29-62.

Warner, T. (2010a). Climate modeling and downscaling. In T. T. Warner (Ed.), *Numerical Weather and Climate Prediction* (pp. 407-455). Cambridge University Press. https://doi.org/10.1017/CBO9780511763243.017

Warner, T. (2010b). Physical-process parameterizations. In T. T. Warner (Ed.), *Numerical Weather and Climate Prediction* (pp. 119-170). Cambridge University Press. https://doi.org/10.1017/CBO9780511763243.005

Wibig, J. (1999). Precipitation in Europe in relation to circulation patterns at the 500 hPa level. *International Journal of Climatology*, *19*(3), 253-269. https://doi.org/10.1002/(SICI)1097-0088(19990315)19:3<253::AID-JOC366>3.0.CO;2-0

Wichura, B., & Kiessling, F. (2009). Ice loads on overhead lines, meteorologial forecastings and observations on lines. Preparing an ice load region map; Eislasten an Freileitungen, meteorologische Vorhersagen und Beobachtungen an Leitungen. Erstellen einer Eislastzonenkarte. *EW*, *108*.

Wilcox, E. M., & Donner, L. J. (2007). The Frequency of Extreme Rain Events in Satellite Rain-Rate Estimates and an Atmospheric General Circulation Model. *Journal of Climate*, *20*(1), 53-69. https://doi.org/10.1175/jcli3987.1

Wilson, C., Sinha, B., & Williams, R. G. (2009). The Effect of Ocean Dynamics and Orography on Atmospheric Storm Tracks. *Journal of Climate*, *22*(13), 3689-3702. https://doi.org/10.1175/2009jcli2651.1

Woollings, T., Gregory, J., Pinto, J., Reyers, M., & Brayshaw, D. (2012). Response of the North Atlantic storm track to climate change shaped by ocean–atmosphere coupling. *Nat. Geosci.*, *5*, 313-317.

Zhu, Y., & Newell, R. E. (1998). A proposed algorithm for moisture fluxes from atmospheric rivers. *Monthly Weather Review*, *126*(3), 725-735.

Part II :Papers

Paper I

:Improvements to melting snow behavior in a bulk microphysics scheme

Emilie C. Iversen, Gregory Thompson, Bjørn Egil Nygaard

Atmospheric Research, 2021

Atmospheric Research 253 (2021) 105471

Contents lists available at ScienceDirect

Atmospheric Research

journal homepage: www.elsevier.com/locate/atmosres

Improvements to melting snow behavior in a bulk microphysics scheme

Emilie C. Iversen [a,b,*], Gregory Thompson [c], Bjørn Egil Nygaard [a]

[a] Kjeller Vindteknikk, Norconsult, Lillestrøm, Norway
[b] University of Oslo, Oslo, Norway
[c] National Center for Atmospheric Research, Boulder, CO, United States

ARTICLE INFO

Keywords:
Precipitation
Melting snow
Fall velocity
Microphysics
NWP
Winter storms

ABSTRACT

Snow falling into a melting layer will eventually consist of a fraction of meltwater and hence change its characteristics in terms of size, shape, density and fall speed. Most microphysical parameterizations in numerical weather prediction models typically only represent purely solid or liquid hydrometeors. Generally, this has been an acceptable compromise since the melting layer is typically very shallow and adding a mixed solid/liquid particle type would result in increased computational time. This research shows how improvements were made to the treatment of melting snow in a microphysical parameterization within the Weather Research and Forecasting (WRF) model by implementing an approximation of snowflake melted fraction together with a physically-based expression for melting particle terminal velocity. In addition, the more appropriate definition of melting level defined by the wet-bulb temperature was consistently used in various process rates, all while not adding additional prognostic variables that would add computational cost. Multiple events observed during the 2015–2016 Olympic Mountain Experiment (OLYMPEX) were used to compare with the WRF model results. The modified scheme is able to represent disdrometer observations of joint particle size and fall velocity during wet snow events, as well as fall velocity profiles through the melting layer derived from a vertically-pointing radar. The improved scheme removes 'bulls' eyes' of snow accumulation in lee-side areas within the melting zone, and should result in better predictions of surface precipitation phase and amount.

1. Introduction

Precise prediction of precipitation phase and amount is highly important for its many socio-economic impacts. For example, in hydrological modelling, precipitation phase at the surface is a first-order driver of hydrological processes in a water shed (McNamara, 2017). Also, melting snow exerts a possible threat to critical infrastructure because the wet, sticky snow may adhere to the structures and form heavy ice sleeves (Makkonen, 1989). Wet snow icing has shown to be particularly problematic for overhead transmission lines, with events causing tower collapses and power outages in all continents of the northern hemisphere, as well as in New Zealand and South Africa (Nygaard et al., 2017). In 2005, a record-breaking wet snowstorm in Germany and neighboring countries caused significant damage to five lines in addition to 83 steel lattice towers. Such damages are extremely costly and power outages for long periods of time have severe consequences for society.

Modern numerical weather prediction (NWP) models typically use a "bulk" microphysical parameterization where cloud and precipitation particles are explicitly predicted using many assumptions about their size distribution, particle shape, density, etc. (Milbrandt and Yau, 2005; Morrison and Milbrandt, 2015; Thompson and Eidhammer, 2014, etc.) The more hydrometeor categories used, the higher the complexity and computational cost; therefore most schemes use various simplifications and approximations to permit usage in real time for operational weather forecasts. One example is the treatment of melting snow, where the melted water mass typically is immediately "shed" into the rain category. In reality, the meltwater sticks to the snowflake until fully melting into a rain drop. As such, the model's resulting snow particle size is too small and fall too slowly along with coexisting rain, in contrast to a unified particle of mixed phase.

Research has shown that surface precipitation as predicted by a microphysical scheme is very sensitive to the snow size distribution and fall speed (Colle and Mass, 2000; Colle and Zeng, 2004; Thériault et al., 2012). Using the Reisner-2 microphysics scheme (Reisner et al., 1998) as part of the Pennsylvania State University / National Center for

* Corresponding author at: Kjeller Vindteknikk, Norconsult, Tærudgata 16, 2004 Lillestrøm, and University of Oslo, Department of Meteorology and Oceanography, Oslo, Norway.
E-mail address: emilieci@geo.uio.no (E.C. Iversen).

https://doi.org/10.1016/j.atmosres.2021.105471
Received 4 March 2020; Received in revised form 30 September 2020; Accepted 10 January 2021
Available online 19 January 2021

Atmospheric Research mesoscale model version 5 (MM5), Colle et al. (2005) found an overprediction of snow in lee slopes of the Cascades, associated with localized areas of melting. This has also been found by the current authors using the Weather Research and Forecasting (WRF) model and the Thompson microphysics (Thompson et al., 2008) when simulating regions of the Pacific Northwest USA in addition to Iceland and Norway.

There is generally a lack of high quality, quantitative ground-based measurements of natural, melting snowflakes due to their irregular shapes, densities, degree of melting, and the practical difficulties in distinguishing between coexisting rain and snow (Yuter et al., 2006; Skofronick-Jackson et al., 2015; McNamara, 2017). One study that most modelling efforts to incorporate melting snow characteristics are based on is the laboratory experiment by Mitra et al. (1990) (hereafter M90). M90 used a vertical wind tunnel to study the behavior of dendritic snow crystals falling through a melting layer. They also emphasize that melting behavior depends on the shape of the snow crystals so that the results likely would be different for snow crystals other than dendrites. Photographs from the wind tunnel revealed that the melt water was contained within the crystal, so that a "ragged" surface of a crystal was maintained for some time, up until the water overtook the crystal to form a water droplet. This is supported by other studies (Knight, 1979; Matsuo and Sasyo, 1981a; Fujioshi, 1986). Measuring the fall velocity of the flakes they found that during the initial stage of melting, fall velocities varied very little, but then began to increase rapidly after about 70% of the original mass was melted, at about the time the waterdrop overtook the crystal, resulting in a non-linear dependence of the fall speed on the snowflake melted fraction (Fig. 1 in M90). Using a simple model, they studied the vertical distance different sized snowflakes in different relative humidities (RH) and temperature gradients travelled before completely melting. The results showed that, logically, larger particles travel longer than smaller particles before melting completely under the same humidity and temperature conditions. If RH was less than 100% the particles travelled some distance before melting began due to evaporative cooling, and the melt distance was increased.

The importance of RH on melting level and precipitation phase has been stressed by many other authors (Matsuo and Sasyo, 1981b; Makkonen, 1989; Gedzelman and Arnold, 1993; Marks et al., 1999; Harder and Pomeroy, 2013; Ding et al., 2014; McNamara, 2017). The wet bulb temperature, T_w, contains information about air temperature (T_a), humidity and pressure, and precipitating particle surfaces have a temperature closer to T_w than T_a (Harder and Pomeroy, 2013; Ding et al., 2014). Given that snow can exist in its dry form in sub-saturated conditions when $T_a > 0$ °C, $T_w > 0$ °C is a better criterion for melting level (Makkonen, 1989).

Yuter et al. (2006) investigated size and fall speed of melting snow using a Particle Size and Velocity disdrometer (PARSILEV). In contrast to rain and dry snow, their observations revealed a large standard deviation in wet snow fall speed, poorly correlated with particle diameter, in agreement with Matsuo and Sasyo (1981a). In wet snow conditions (temperature between 0 and 0.5 °C) the relationship between particle size and fall speed measured with the PARSIVEL showed a bimodal distribution, with distinct populations of rain and snow. This suggests that once melting has progressed sufficiently, wet snow particles make a quick transition to rain and do not linger in an intermediate state for long, which agrees well with the experiment of M90.

Szyrmer and Zawadzki (1999) (hereafter SZ99) developed a bulk parameterization scheme specifically for modelling of the melting layer. They introduced melting snow as a unique species and utilized the expression of fall speed for melting snowflakes defined by M90 by also introducing a snowflake melted fraction: f = mw/m, where mw is the melted mass and m is the total mass. Their model fit perfectly with the experimental results of M90. As the ventilation coefficients depend on particle size and physical characteristics of the particle, the authors also introduced a new expression for the ventilation coefficient of melting snow as a function of the degree of melting. The minimum diameter of snowflakes not completely melted was introduced as a diagnostic variable related to the heat exchange and melting fraction, which determined the cutoff diameter for the melting snow size distribution. This represented the effect that smaller snowflakes melt into rain first.

Based on the multi-moment bulk microphysics scheme developed by Milbrandt and Yau (2005), Thériault and Stewart (2010) proposed a modified scheme with improvements in predicting winter precipitation types associated with temperatures around 0 °C, though noting that it is not aimed for real-time NWP. They introduced wet snow and slush (among three others) as new hydrometeor species, and adopted the wet snow terminal velocity equation and the calculation of the liquid fraction from SZ99, based on the observations by M90. In the scheme snow starts to melt when $T_w > 0$ °C. Also based on M90 and SZ99, Frick et al. (2013) implemented a new snow melting parameterization for the COSMO ("consortium for small-scale modelling") model (Doms and Schättler, 2002), and Cholette et al. (2019) modified the relatively new Predicted Particle Properties (P3) scheme (Morrison and Milbrandt, 2015; Milbrandt and Morrison, 2016) to allow for the representation of wet snow and ice pellets, both by predicting the ice bulk liquid fraction.

The Thompson-Eidhammer microphysics scheme (an aerosol aware Thompson scheme), provided as part of the WRF model, has been explicitly developed and extensively tested for forecasting winter precipitation (Thompson et al., 2008; Thompson and Eidhammer, 2014). The scheme is partially double moment and consists of physically based assumptions to force it to act more like a full double-moment scheme, suitable for real-time NWP due to the decreased computational cost compared to higher order schemes. As Thompson et al. (2008) though points out, a potential improvement to the scheme is an explicit treatment for melting snow to produce the correct terminal velocities in the melting layer.

The objective of this research is to improve the Thompson-Eidhammer microphysics scheme with respect to the representation of melting snow based on M90 and SZ99, without adding more model prognostic variables in order to maintain computational time for real-time operations. To validate the introduced changes, multiple model case studies were performed to compare with in-situ measurements of hydrometeor size and fall speed from a disdrometer and a vertically pointing Doppler radar observed during the 2015–2016 Olympic Mountain Experiment (OLYMPEX). To the best of our knowledge, this study is the first to compare real-case 3D NWP model simulations of melting snow fall velocity with in-situ observations. Other modelling studies comparing reflectivity or fall speed profiles either use idealized simulations or overlook the melting layer. The overall objective here is to improve prediction of precipitation phase and amount at the surface using the WRF model with the Thompson-Eidhammer microphysics.

The paper is structured as follows: Section 2 introduces the relevant portions of the current scheme, including the improved aspects with respect to melting snow. Section 3 describes data and methods, including the specific weather events and observational data, model configuration, as well as the methods to compare model to observations. The results are presented in Section 4 and conclusions follow in Section 5.

2. The microphysics scheme

The Thompson-Eidhammer microphysics scheme is a partially double moment bulk scheme where each of its five hydrometeor species is represented by generalized gamma size distributions. Cloud water, cloud ice and rain are double moment (both number concentration and mass mixing ratios are predicted), while snow and graupel are single moment (only mass mixing ratios are predicted). There are two aspects that make this scheme unique compared to most other similar schemes: its snow size distribution is described by a sum of exponential and gamma distributions, and snow assumes a non-spherical shape with a bulk density that varies inversely with diameter (Thompson et al., 2008). More details are described in Thompson et al. (2004, 2008) and

Thompson and Eidhammer (2014). Here we only discuss the details of the scheme relevant for melting snow behavior.

2.1. Relevant details of the current scheme

All species use the relatively standard power-law form to describe their mass as function of diameter:

$$m(D) = aD^b \tag{1}$$

The velocity relation follows Ferrier (1994) using an exponential to handle the large particles better than the regular power law:

$$v(D) = \alpha D^{\beta} e^{-fD} \tag{2}$$

The constants are for rain: $a_r = \pi\rho_w/6$, $b_r = 3$, $\alpha_r = 4854\ s^{-1}$, $\beta_r = 1$ and $f_r = 195$, where ρ_w is the density of water, while for snow: $a_s = 0.069$ kg/m^{-2}, $b_s = 2$, $\alpha_s = 40\ m^{0.45}s^{-1}$, $\beta_s = 0.55$ and $f_s = 125$ (the constants for all hydrometeors are given in Table A1 of Thompson et al. (2008)). Together with these equations and constants, each species' mass and number-weighted terminal velocities are properly computed. For snow, a "boosting" factor (F_{boost}) is also applied to the fall velocity calculation, to take into account the increased density and associated fall speed of rimed snow. F_{boost} is found by exploiting the riming to depositional growth ratio, and is linearly increased from 10% to 50% between ratios 5:1 to 30:1, building on observations by Locatelli and Hobbs (1974). All calculated fall velocities are also density corrected to take into account the varying atmospheric density with height.

The melting of snow is calculated through a thermodynamic heat balance, ensuring that melting only occurs when $T_w > 0$ °C (following immediately from Pruppacher and Klett (1997) as it was also applied by Reisner et al. (1998); Eq. A.37). If RH < 100% sublimation of snow is calculated, treated nearly the same as rain evaporation following Srivastava and Coen (1992) (see Appendix A of Thompson et al. (2008)). Melting rate is increased when snow is actively collecting rain and/or cloud water (as was done in (Rutledge and Hobbs (1983)). The resulting melted snow mass is removed from the snow and added to the rain category. This redistribution of mass would obviously decrease the mass-weighted mean diameter (MWMD) of snow and increase that of rain below the melting level, potentially causing snow to fall too slowly through the melting layer. This technique is nearly always used for one and two-moment parameterizations whereas real snow does not experience this slowing since the melting particles are a mixture of liquid and ice.

To combat this problem of melting snow falling too slowly, in WRF code versions preceding v3.8, terminal velocity of snow below melting level, defined where $T_a > 0$ °C, was the maximum of the velocity of rain and snow at the given level. It was later noted that this caused melting snow to fall too fast due to obtaining rain velocities, and a temperature dependent function was added in v3.8. However, a serious bug was mistakenly introduced which led the fall velocity to increase asymptotically as T_a approached 0 °C, opposite of what was probably intended. Therefore, throughout the rest of this paper, the "old" method for calculating fall velocity of melting snow refers to the code preceding WRF v3.8.

2.2. Changes performed to the scheme

First, given the emphasis on the dependence of melting level and precipitation type on RH and the use of T_w to describe hydrometeor surface temperature in the literature, the definition of melting level in the scheme is changed to $T_w > 0$ °C. In the scheme there is also an expression of the production of rain number concentration due to melting of snow where the use of T_w makes more physical sense:

$$\left[\frac{dn_r}{dt}\right]_{sml} = \frac{M_0 10^{mT_a}}{q_s \rho}\left[\frac{dq_r}{dt}\right]_{sml} \tag{4}$$

where *sml* indicates process rates due to melting of snow, n_r, q_r, and q_s are the number concentration and mixing ratio of rain, and the mixing ratio of snow, ρ is the moist air density, M_0 is the zeroth moment of the snow size distribution, and m is a tunable constant (set to −0.2 following WRF version 3.8.1 (Brown et al., 2017)). Because snow is a single moment species, the value 10^{mT_a} is an artificial way of reducing the snow number concentration during melting to account for the decreasing number of very tiny snow particles as temperature increases. Changing this to using T_w instead ensures that snow number concentration is only reduced if there is actually melting occurring and will specifically contribute to improve predictions in typical dry regions of wintertime storm systems.

Second, given the findings by M90, the fall speed of melting snow should be expressed as a function of its melted fraction. To maintain the current computational cost of running the scheme, the introduction of an additional prognostic variable such as the melted mass fraction is undesirable. If we assume that most of the rain particles present in the melting layer are generated from the melting of snow, we can utilize the ratio of rain mass to total mass of rain and snow at a given level (the "liquid ratio", LR) as the melted fraction:

$$LR = \frac{q_r}{q_r + q_s} \tag{5}$$

This could introduce errors in some cases because 1) rain could be produced from strong lifting of air within the melting layer, and 2) rain falls faster than snow, so at any level most of the rain has originated from a level above (Milbrandt et al., 2012). Anyhow, the use of LR can give a physically based approximation of the average melted fraction in the melting layer, without the addition of an extra prognostic variable.

M90 presented the following expression for the fall speed of melting snow:

$$V_m = f(V_r - V_s) + V_s \tag{6}$$

where V_m, V_s and V_r define the velocities of melting, dry and completely melted snowflakes (rain), respectively, and f is the snowflake melted fraction. In order to get the exponential relationship found by M90, SZ99 manipulated this expression and introduced the function $g(f)$:

$$V_m(D_w, f) \approx \frac{1}{g(f)} V_r(D_w) \tag{7}$$

$$g(f) \approx \frac{a}{\alpha} - c_g f - c_g f^2 \tag{8}$$

D_w is the melted diameter (the diameter equivalent to the snowflake being completely melted), $a = 1690\ cm^{0.4}\ s^{-1}$, $\alpha = 366\ cm^{0.39}\ s^{-1}$ and $c_g = 0.5[(a/\alpha) - 1] = 1.8$. The constants resulted from the original power law expressions for fall velocity using the melted diameter found in Langleben (1954) and Sekhon and Srivastava (1971). Here we adopt this expression with a few modifications to fit with the velocity expressions of the Thompson-Eidhammer scheme. For simplicity, this calculation is performed for the mass weighted mean diameter (MWMD), and not integrated over the whole distribution, which is a close approximation. At the melting level the following steps are performed to obtain $V_r(D_w)$:

The melted snow equivalent water drop diameter, D_w, can be found by rearranging the mass expression for rain given in (1) and substituting with the mass of snow:

$$D_w = \left(\frac{m_s}{a_r}\right)^{\frac{1}{b_r}} \tag{9}$$

Then, inserting into (2) gives:

$$V_r(D_w) = \alpha_r D_w^{\beta_r} e^{-f_r D_w} \tag{10}$$

The melting snow velocity expression in (7) and (8) ensures that:

$$V_m = \begin{cases} \frac{a}{\alpha} V_r(D_w) = V_s, f = 0 \\ V_r(D_w), f = 1 \end{cases} \quad (11)$$

The given relationship between $V_r(D_w)$ and V_s for $f = 0$ is not valid using the velocity expressions of the Thompson-Eidhammer scheme. The correct relationship is found by dividing (2) given for dry snow by (10). Because (2) is expressed by the dry snow diameter, (10) needs some manipulation. Substituting (1) (given for dry snow) into (9), for so into (10), will give $V_r(D_{s*})$, where D_{s*} is the dry snow MWMD. After some algebraic manipulation the resulting relationship is:

$$\frac{V_r(D_w)}{V_s} = A = 6.176 D_{s*}^{0.116} e^{\left(-9.925 D_{s*}^{0.666} + 100 D_{s*}\right)} \quad (12)$$

If the snow is rimed when crossing the melting level, then its velocity is increased by the boosting factor, F_{boost},

$$A_{rimed} = \frac{A}{F_{boost}} \quad (13)$$

Using our approximation for the melted fraction given in (5), the fall velocity of melting snow is thereby:

$$V_m(D_s, LR) = \frac{V_r(D_w)}{A - 0.5(A-1)LR - 0.5(A-1)LR^2} \quad (14)$$

where D_s is the dry snow MWMD at melting level height, and LR is found for the relevant model level. This expression is shown graphically in Fig. 1 for variable D_s and LR.

Thirdly, as the ventilation coefficients also depend on particle fall speed, additional changes were made accordingly, using the following coefficients from Pruppacher and Klett (1997) of rain and snow:

$$F_r(D_r) = 0.78 + 0.308 S_c^{1/3} R_e^{1/2} \quad (15)$$

$$F_s(D_s) = 0.86 + 0.28 S_c^{1/3} R_e^{1/2} \quad (16)$$

where $R_e = v(D)D\rho_a/\upsilon$ is the Reynolds number, ρ_a the air density, υ the dynamic viscosity of air, and $S_c = \upsilon_a/D_v$ is the Schmidt number, υ_a the kinematic viscosity of air, D_v the diffusion coefficient. To maintain code structure as is, the ventilation factor for melting snow is expressed by:

$$F_m(D_s, LR) = Y(D_s, LR) F_s(D_s) \quad (17)$$

Hence, $Y(D_s, LR)$ is found by $F_m(D_s, LR)/F_s(D_s)$, where $F_m(D_s, LR)$ is (16) but substituted with the velocity of melting snow in (14). After some approximation and algebraic manipulation, the resulting factor, Y, is:

$$Y(D_s, LR) = \sqrt{\frac{A}{A - 0.5(A-1)LR - 0.5(A-1)LR^2}} \quad (18)$$

The ventilation factor for melting snow is shown graphically in Fig. 2 for variable D_s and LR. As can be seen the ventilation factor for snow is not large enough for high LR values when compared to that of rain, which is due to the differing factors in (15) and (16), but is an improvement over using the ventilation factor for dry snow which would be too small.

3. Data and methods

3.1. Observational data

Observational data are freely available from the Olympic Mountains experiment (OLYMPEX), which was a comprehensive field campaign held on the Olympic Peninsula in Washington, USA, during winter 2015–2016, to study orographic modification of frontal precipitation processes (Houze et al., 2017). Data are available from Two-Dimensional Video Disdrometers (2DVD), Micro Rain Radars (MRR), tipping bucket rain gauges and radiosondes (among other instruments). The 2DVD is an optical disdrometer that uses orthogonal image projections to measure the size, shape and velocity of falling hydrometeors (Kruger and Krajewski, 2002). The quality-controlled dataset provided is described in Petersen et al. (2017a), where all drops less than 10 mm in diameter are included in this study. It should be noted that strong winds absolutely influence data quality. The MRR is a vertically pointing, dual-polarization Doppler radar that measures signal backscatter from which Doppler spectra, radar reflectivity and Doppler velocity are derived (Peters et al., 2002). The quality-controlled dataset provided is described in Petersen and Gatlin (2017), where the processed

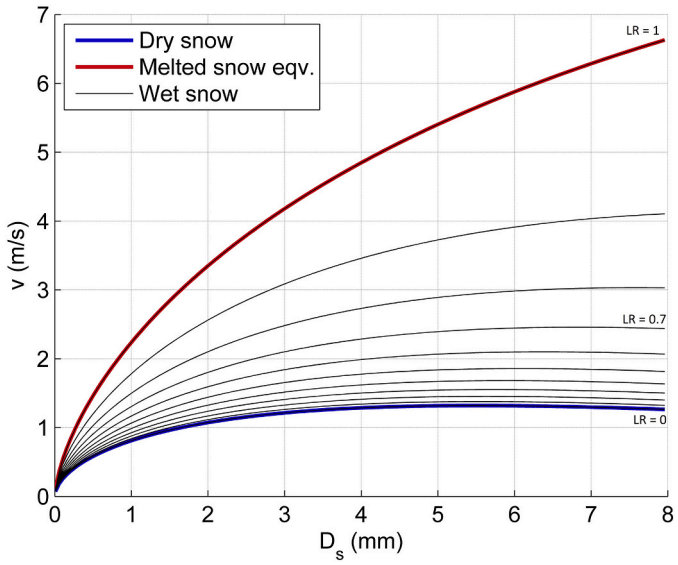

Fig. 1. The expression for fall velocity of melting snow (14) as function of dry snow diameter (D_s) and LR from 0 to 1 in intervals of 0.1 given by the different black lines. The expression for dry snow velocity (2) is shown in blue, and for melted snow equivalent velocity (10) (but here given for D_s) in red. (For interpretation of the references to colour in this figure legend, the reader is referred to the web version of this article.)

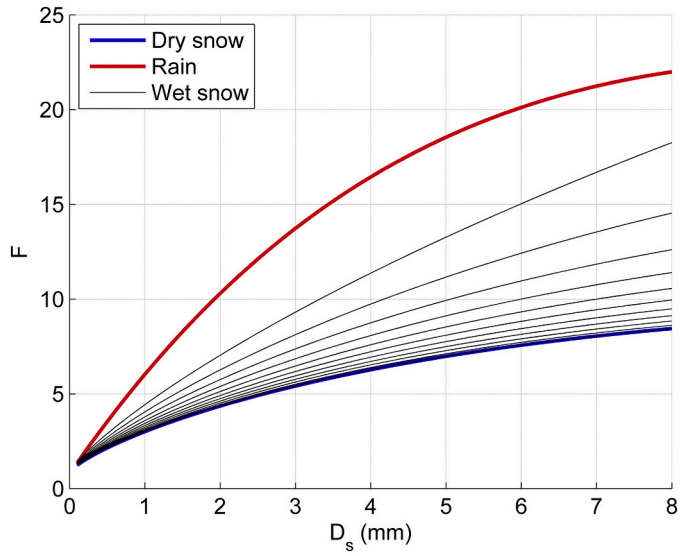

Fig. 2. The expression for ventilation factor (F) for melting snow (in (17) and (18)) as function of dry snow diameter (D_s) and LR from 0 to 1 in intervals of 0.1 given by the different black lines. The expression for dry snow (16) is shown in blue, and for rain (15) (but here given for D_s) in red. (For interpretation of the references to colour in this figure legend, the reader is referred to the web version of this article.)

instantaneous data are used here. As they describe, at higher measurement frequencies there can be signal attenuation effects, but these are generally weak enough to be corrected for. Though, in strong vertical winds the instrument can overestimate the amount of attenuation which reduces measuring accuracy (Tridon et al., 2011). Therefore, one should be cautious using the data measured during strong-wind situations. Data from the rain gauges are described in Petersen et al. (2017b), where the cubic spline interpolated 1-h rain rates (mm/h) at 1 min time steps are used here (Wang et al., 2008). As Wang et al. (2008) point out, the error of using this method increases as the averaging time step decreases. At 1 min time steps the errors are relatively large and are bounded by a linear line for precipitation rates <10 mm/h, whereas cluster around certain values for rates >10 mm/h (see their Fig. 5). It should also be noted that the gauges were not wind shielded, which could affect their measuring accuracy in windy conditions. Data from the radiosondes are described in Rutledge et al. (2018), where the Level 4 data are used here (soundings visually inspected with QC flags; hi-res data interpolated to uniform 5 hPa intervals).

Data are available from several instrumentation sites across the Olympic peninsula. The sites and instruments used in this study are listed in Table 1 and displayed in Fig. 4. Of the total four sites instrumented with a 2DVD, three were located below 100 m and recorded mostly rain throughout the winter season. The Neilton Point site is located substantially higher, at 657 m and recorded mixed precipitation on some days during the winter. This site is located on an exposed ridge and so was affected by strong winds at times, typically coinciding with the timing of mixed precipitation, as both were associated with the passage of frontal systems. Given that this site is the only one available with prolonged records of mixed precipitation from a 2DVD disdrometer, the data are still used for model validation in this study, but with caution. A station in the lowland, Fish Hatchery, is used to investigate MRR data due to less exposure for the strongest winds as well as good data coverage through the winter. Tahola is one of two sites where ground radiosondes were launched, and the one closest to the other data resources used here.

3.2. Weather events

The Pacific mid-latitude storm tracks typically pass across the region of the Olympic peninsula, causing a succession of low-pressure systems to bring abundant precipitation to the area throughout winter. The presence of the Olympic Mountain causes a precipitation intensification when the frontal systems move from the Pacific Ocean and into the mountainous terrain. As Houze et al. (2017) described, after 10 December 2015, the weather turned colder and the mean flow was west-northwesterly with anomalous trough conditions over the Northwest, a regime featuring frontal systems dominated by more ice-phase microphysics.

Two different weather events are chosen to study here due to the obvious mixed phase precipitation signal recorded at the sites listen in Table 1. The first event occurred 12–13 Dec. In the morning (UTC time) of 12 Dec stratiform pre-frontal precipitation moved into the area. Precipitation gradually intensified in the course of the afternoon before the front passed and moved out of the area by midnight, seen in the satellite imagery in Fig. 3 (left). Post-frontal rain showers persisted into 13 Dec. The second event occurred 19–21 Dec. Cold temperatures persisted, with relatively low melting level. The event was characterized by a cold front passing between two periods of post-frontal convection, with the bulk of the frontal precipitation falling between 0500 and 1400 UTC 20 Dec. The frontal passage can be seen in Fig. 3 (right).

3.3. Model configuration

The WRF model version 4.0.3 was set up with two nested domains, the outer with a horizontal resolution of 6 km and the inner of 3 km (Fig. 4), with 72 vertical levels. ERA-interim reanalysis data were used for initial and boundary conditions. Model parameterization choices are listed in Table 2 along with the Thompson and Eidhammer (2014) aerosol-aware microphysics scheme, with the modifications presented in Section 2.2 (termed the new method). For comparison, simulations were also carried out with the old method for defining melting level and melting snow fall speed (see Section 2.1).

3.4. Comparison of modelled and observed parameters

The 2DVD measures hydrometeor size and fall speed close to the ground. We output the MWMD and associated fall speed of rain and snow from the model at every model timestep. As mentioned in Section 2.1, when snow is melting in the microphysics scheme, the meltwater is transferred over to the rain category. This causes the snow MWMD to shrink. According to observations, as discussed in the introduction, the meltwater stays on the snowflake, and the diameter changes due to the collapse of the snowflake into a raindrop when starting to reach 70% melted fraction. There exists no simple, theoretical expression to present the change in diameter of a melting snowflake (D_m). As such, in order to compare with the observed snow fall speed as function of its diameter, we add the MWMD of simulated snow and rain in an attempt to better represent D_m (and limit upwards to not exceed D_s):

$$D_m = min(D_s, D_{s*} + D_r) \tag{19}$$

where D_{s*} is the dry snow MWMD at the relevant model level (not to be confused with D_s which is the dry snow MWMD at the top of the melting layer before melting begins). This results in a D_m that starts to decrease after the snow has fell some distance down the melting layer, until reaching D_r at the bottom.

As mentioned above, the Doppler velocity can be derived from the MRR instrument, which is the first moment of the Doppler spectrum. Doppler velocity is weighted by the reflectivity factor, Z:

$$Z = \int \sigma(D) n(D) dD \tag{20}$$

$$V_{dop} = \frac{\int V(D) Z(D) dD}{\int Z(D) dD} + w \tag{21}$$

where $\sigma(D)$ is the hydrometeor backscattering cross section, $n(D)$ is the droplet size distribution and w is vertical air motion. For rain, σ depends on D^6, and for the non-spherical shape of snow, σ depends on D^4, and so Doppler velocity qualitatively represents the velocity of larger drops. In order to compare this with simulated fall velocities, the reflectivity weighted velocity needs to be calculated. This was done by for example Han et al. (2013) and Molthan et al. (2016), and a detailed outline of the calculation of reflectivity factor and reflectivity weighted fall velocity of rain and snow based on the Thompson scheme can be found in the Appendix of Han et al. (2013). Simply stated, the simulated reflectivity weighted fall velocity to be compared with the Doppler velocity is:

Table 1
Overview of the OLYMPEX campaign sites and instruments used in this study.

Site	Location	Elevation	Radiosonde	Rain gauge	2DVD	MRR
Taholah	47.35°N, 124.29°W	4 m	x			
Fish Hatchery	47.36°N, 123.99°W	52 m		x		x
Neilton Point	47.39°N, 123.87°W	657 m		x	x	

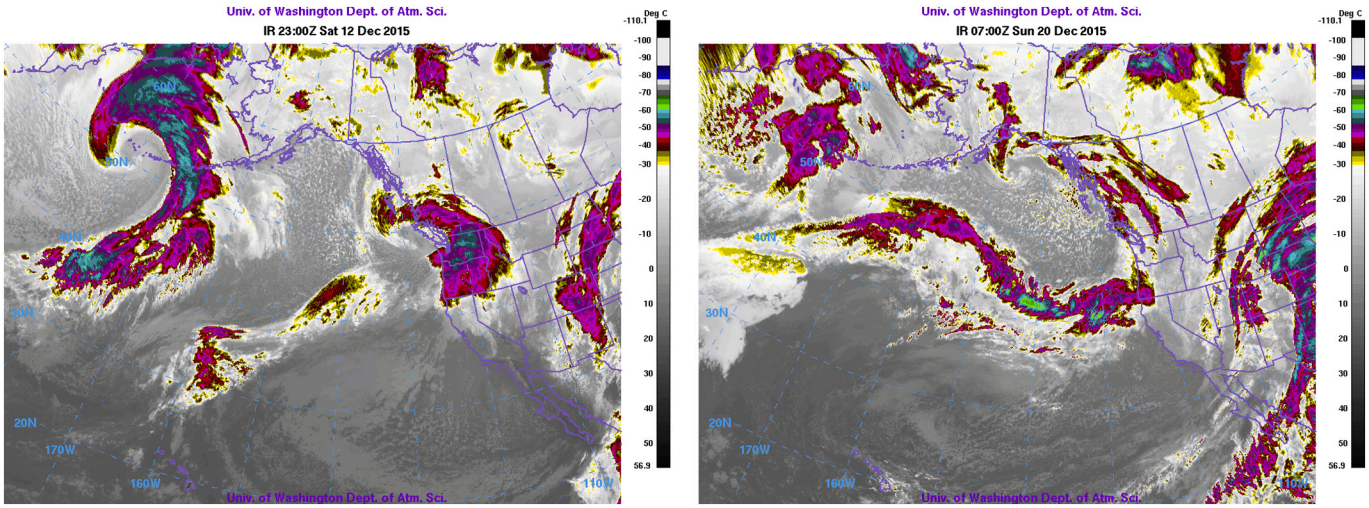

Fig. 3. Infrared satellite imagery of cloud top temperature over the Pacific Northwest at 2300 UTC 12 Dec 2015 (left) and 0700 UTC 20 Dec 2015 (right). Created by University of Washington Department of Atmospheric Sciences, available through the OLYMPEX web page (NASA and Uni. Washington, 2020).

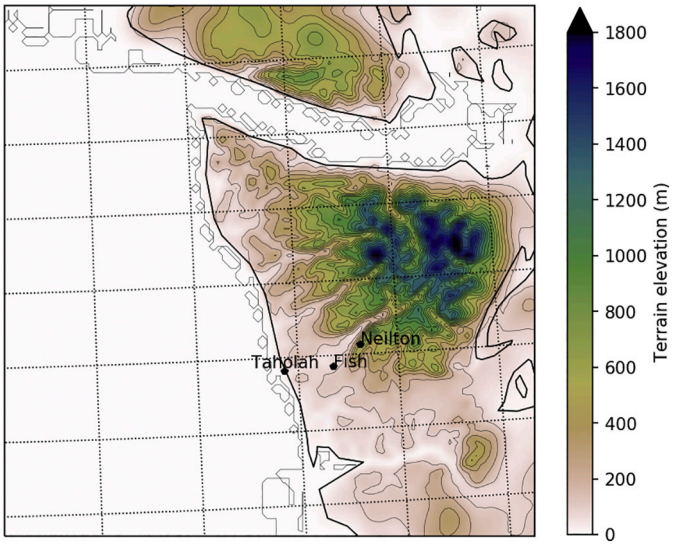

Fig. 4. Terrain elevation of WRF inner domain of 3 km resolution, including the instrumentation sites listed in Table 1.

Table 2
Parameterization scheme choices for the WRF model configuration.

Type of scheme	Name	Reference
Microphysics	Thompson-Eidhammer aerosol-aware	Thompson and Eidhammer (2014)
Boundary layer	MYNN 2.5 level TKE	Nakanishi and Niino (2006)
Radiation	RRTMG	Iacono et al. (2008)
Land surface	Noah	Mitchell (2005)

$$V_{z,tot} = \frac{\sum_{x=1}^{n} \int V_x(D)\sigma_x(D)n_x(D)dD}{\sum_{x=1}^{n} \int \sigma_x(D)n_x(D)dD} \tag{22}$$

where x denotes the different types of hydrometeors present and n the total number of hydrometeors. Above melting level, the reflectivity from dry snow will dominate, whereas at the bottom of the melting layer, the reflectivity from rain will dominate, which all are found through (20). Inside the melting layer, the characteristics of snow will change including its scattering properties. It is well known that melting snow particles cause an area of enhanced reflectivity seen by radars, called the bright band (Fabry and Zawadzki, 1995). This reflectivity is not immediately found through a moment of the size distribution, like for snow and rain.

To be able to compare the developed meteorological model of the melting layer in SZ99 with observations, Fabry and Szyrmer (1999) implemented a scattering model to generate the reflectivity field associated with the hydrometeors. They tested several scattering models consisting of differing snowflake morphology of varying complexity, in terms of the position of the meltwater and air bubbles relative to the ice. The simplest model assumes that the meltwater forms a film around the ice structure, but as they state, is also the least physically feasible. However, when comparing reflectivity weighted fall velocity based on these differing scattering models, they appeared very similar, and compared well to radar derived Doppler velocity. Implementing such a scattering model is complex and outside the scope of this study, but we can utilize the concept of the simplest scattering model to obtain V_Z in the melting layer based on the available parameterizations:

By doing some empirical fitting on the model output we find the approximate linear relationship:

$$\frac{V_{Z,r}}{V_r} = -0.2D_r + 1.74 \tag{23}$$

where $V_{Z,r}$ is rain reflectivity weighted fall velocity. If we assume that the melting snow will reflect as a large raindrop using the simplest scattering model, then

$$V_{Z,m} = (-0.2D_m + 1.74)V_m \tag{24}$$

where $V_{Z,m}$ is melting snow reflectivity weighted fall velocity. Because V_m is only calculated for MWMD instead of being integrated over the whole distribution, this method is a slight over-simplification. Furthermore, particle fall velocity output from the model does not incorporate vertical air motion. Given that vertical air motion is implicit in Doppler velocity, the comparison between MRR and model should be treated with caution in windy conditions, also due to the errors this might pose on the measurements (see Chapter 3.1).

4. Results

Results from the simulations using the old and the new method are shown in Fig. 5. The non-linear increase in fall speed with LR seen in observations is evident using the new method (bottom left), while there

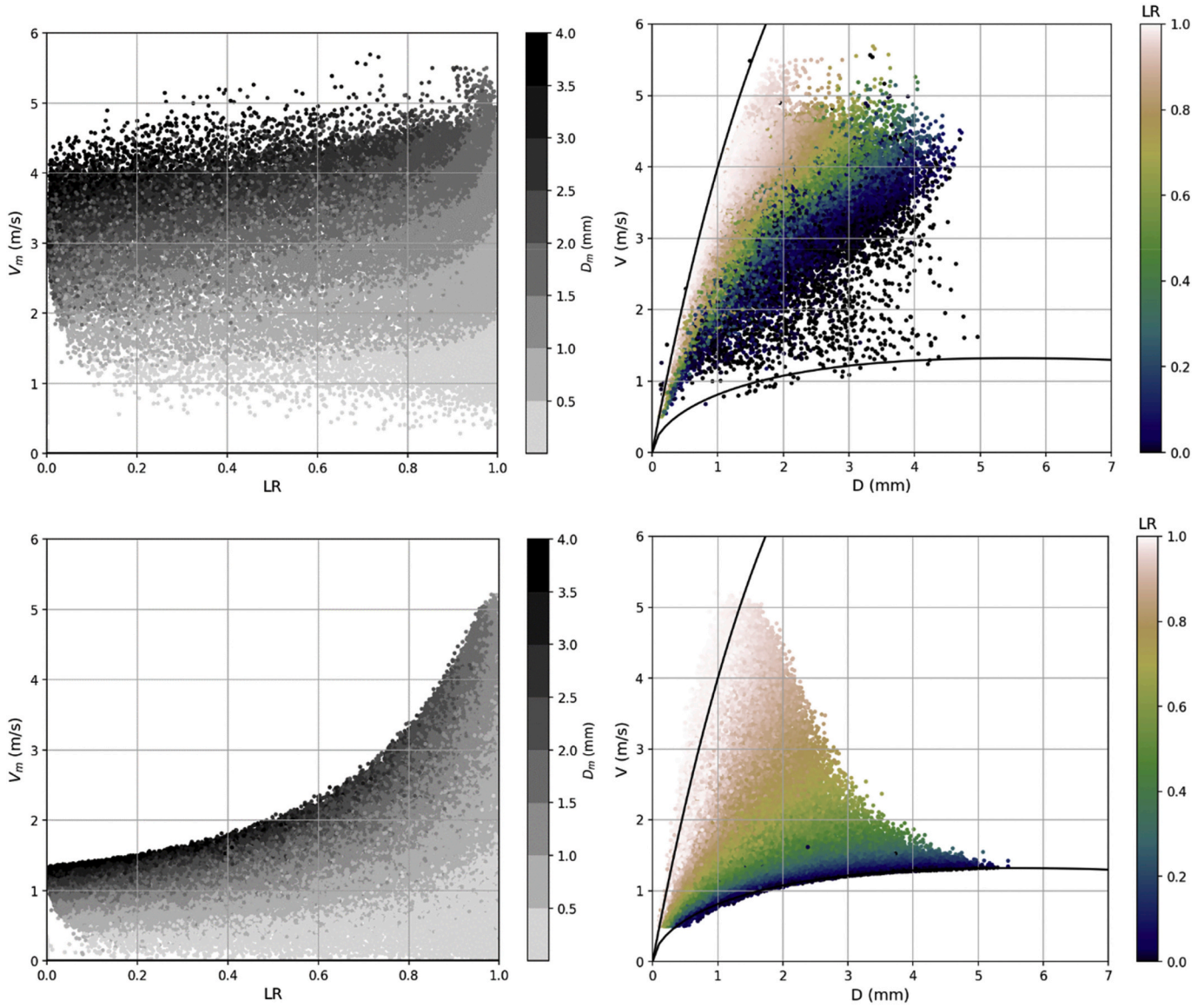

Fig. 5. Simulation output from all grid points and model level 2. Top: The old method, Bottom: The new method. Left: Fall velocity of melting snow versus LR. The color scale denotes melting snow diameter (D_m). Right: Fall velocity versus diameter for melting snow in colors (color scale denotes LR, diameter is D_m). The fall speed expression for dry snow and rain (given in (2)) are plotted in black. (For interpretation of the references to colour in this figure legend, the reader is referred to the web version of this article.)

is no relationship with liquid ratio using the old method (top left). Fall speeds associated with different snow diameters show a spread between the fall speed relations of dry snow and rain using the new method, while also clearly showing the non-linear increase with LR (bottom right). This distribution resembles the disdrometer measurements from melting snow situations plotted in Fig. 3 of Yuter et al. (2006). The new method is clearly better at presenting a more physical nature of partly melted snow.

4.1. Comparison with MRR data

During the event of 12–13 Dec, the MRR at Fishery showed a clear bright band signature in reflectivity and melting layer signature in terms of increased Doppler velocity, especially for the stratiform precipitation occurring before the passage of the front. As such, this provides a good case for validation of the vertical profile of fall velocity through the melting layer, although it is important that temperature, precipitation rate, and particle sizes firstly validate well between observations and model. Three soundings were launched at Taholah on 12 Dec, shown in Fig. 6. At 1500 UTC the sounding indicated a nearly saturated layer over the lowest 300 m, followed by a subsaturated layer and another nearly saturated layer at and above 1100 m. The WRF simulation has somewhat too warm air below and too cool air above the melting level, no near-surface saturated layer and cloud base too low. At 1914 UTC, the WRF-simulated profile corresponds relatively well with observed, except for a slight temperature offset of about +1.5 °C. At 2135 UTC the warm sector moved over the area, noticed in a rise of melting level of about 850 m in both sounding and model. Model ground temperature is overestimated by about 5 °C at this time.

In addition to the rain gauge, rain rate is also shown as derived from the 2DVD (see Tokay et al. (2001) for methodology) (Fig. 7). The model captures one of the intermittent showers and misses most others between about 1115 and 1440 UTC 12 Dec, and captures relatively well the longer period of steady stratiform rain between 1500 and 2000 UTC. Clearly the model then predicts the frontal passage with a strong intensification of precipitation rate, which in reality occurred about an

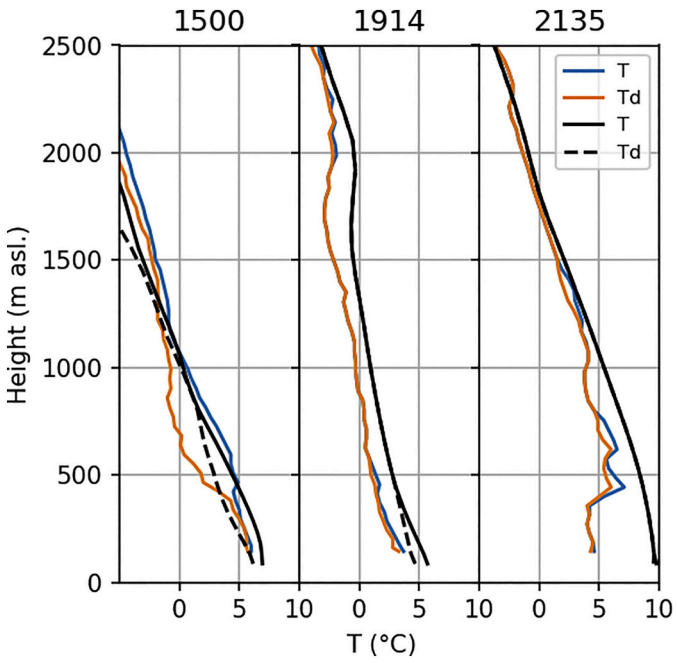

Fig. 6. Soundings of air temperature (T, blue) and dew point temperature (T_d, orange) from the Taholah site launched at three different times (UTC) during 12 Dec. Simulated air temperature and dew point temperature (dashed) in black from the Fishery site. (For interpretation of the references to colour in this figure legend, the reader is referred to the web version of this article.)

hour later (an early arrival of the front and warm sector also explains the near-ground warming seen at 2135 UTC in Fig. 6). Quite strong winds were associated with this frontal passage with near-surface wind speeds of about 9–11 m s^{-1} and upper-level wind speeds reaching 30 m s^{-1} as the front passed. This could have affected both the observed precipitation rate and MRR measurements. Because of this and the timing issue, the validation against MRR is limited to 1100–1900 UTC. Wind speeds were lower (3–8 m s^{-1}) for this period, serving for a more accurate comparison between observations and model.

The droplet size distribution measured by the 2DVD shown in Fig. 8a shows relatively larger particles associated with the peaks in precipitation rate, up to 4 mm in diameter. Given the temperature profiles, the precipitation was most likely rain at the surface, where the 2DVD was measuring, also supported by the close match in measured precipitation rate by the gauge and 2DVD. The MWMD (Fig. 8b) was 0.5–2 mm during the first few showers and was relatively steady at about 1–1.4 mm during the stratiform period. WRF is able to predict relatively well the evolution of MWMD, though with less variability and a slight underestimation (corresponding with the underestimation of rain rate). The peaks in precipitation size, corresponding with peaks in precipitation rate, is also evident in the vertical structure from the model (Fig. 8c). The rain MWMDs at the surface correspond to snow MWMDs of about 3–4 mm at the top of the melting layer in the model. Doppler velocity from the MRR is shown in (Fig. 8d), and the melting layer associated with the increase in velocity is evident between 1300 and 500 m. Above the melting level, Doppler velocity was 1–2 m s^{-1} associated with dry snow. As the snow fell across melting level its velocity increased to 5.5–7.5 m s^{-1} as the flakes had completely melted into rain. This is relatively well replicated by the model (Fig. 8e). The peaks in velocity of 2–3 m s^{-1} above melting level are associated with rimed snowflakes which has a boosted fall velocity. Such peaks are also evident in the MRR Doppler velocity. Results from the post frontal convective period following the frontal passage into 13 Dec are shown in Appendix.

Velocity profiles from the shower which occurred 1200–1300 UTC and during the stratiform period at 1700 UTC are shown in Fig. 9. No sounding is available for the timing of the shower, but by visual inspection of the time-height plots it seems that model melting level is about 100 m too low and hence the profiles are lifted 100 m in the plot. The sounding at 1500 UTC (Fig. 6) indicates that melting level is about 100 m too high in the model. Assuming this is also the case for 1700 UTC, the model profiles are lowered 100 m. By slightly shifting the model melting level height in this way, the timing of melting between observations and model agrees well and allows for a better comparison. The vertical velocity profiles are in good agreement through the melting layer, resulting in similar velocities of rain reaching the ground. It is evident how the old method increases snow fall velocity immediately after crossing the melting level, and that the velocity is overestimated throughout the melting layer.

4.2. Comparison with disdrometer data

During the event 19–21 Dec, the 2DVD at Neilton Point showed a mixture of rain and snow. There are only two soundings available from the Tahola site for this period in the morning of 19 Dec, shown in Fig. 10. At 0215 UTC the sounding shows subsaturated conditions through the column, while the model shows an obvious cloud base corresponding almost exactly with melting level at about 1000 m (above mean sea level hereafter) such that melting level is about 200 m too high. At 0517 UTC the temperature profiles at Neilton Point (black) corresponds very well to the observations at Tahola, and melting level is at the same height. A clear over-estimate of model surface temperature at Tahola (gray) is seen at both times, though if one can assume a uniform temperature structure between Tahola and Neilton Point, surface temperature at Neilton Point matches very well the temperature at 650 m at Tahola at both times of about 2.5 °C. Model surface temperature (Fig. 11) varies between 0 and 2.5 °C through the period, except for when the warm sector was over the area from about 0500–1500 UTC 20 Dec when it increases to 5 °C.

The frontal passage also brought stratiform precipitation, somewhat

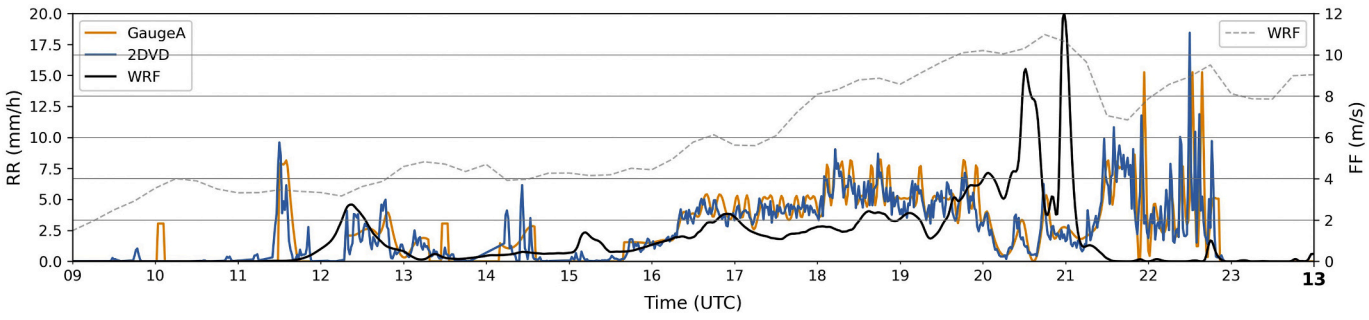

Fig. 7. Precipitation rate (RR) at Fishery measured by the rain gauge (orange), derived from the 2DVD (blue) and simulated by WRF (black), and simulated wind speed (FF, dashed gray), 12 Dec. (For interpretation of the references to colour in this figure legend, the reader is referred to the web version of this article.)

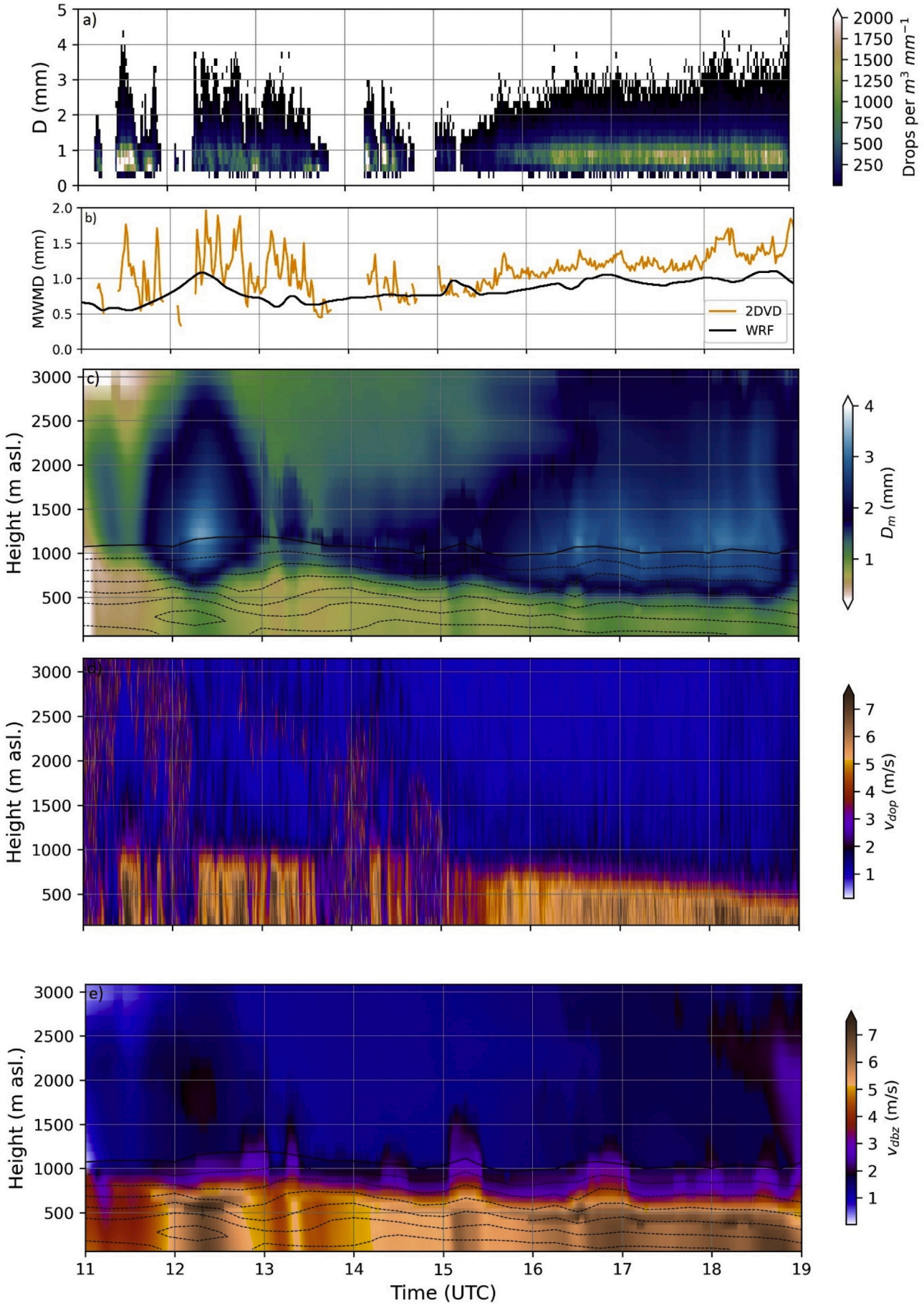

(caption on next page)

Fig. 8. Observed and simulated variables during 11–19 UTC 12 Dec at Fishery. a) Droplet size distribution from 2DVD, colors display number of drops per. m^3 mm^{-1}. b) Mass weighted mean diameter (MWMD) from 2DVD and WRF (model level 1). c) Time – height plot of particle size (D_m, see (19)) from the model. d) Time – height plot of Doppler velocity (V_{dop}) from MRR. e) Time – height plot of reflectivity weighted fall velocity (V_{dbz}) from the model, derived through the methodology outlined in Section 3.4. Black lines are wet bulb temp. starting at 0 °C (solid) increasing in intervals of 1 °C.

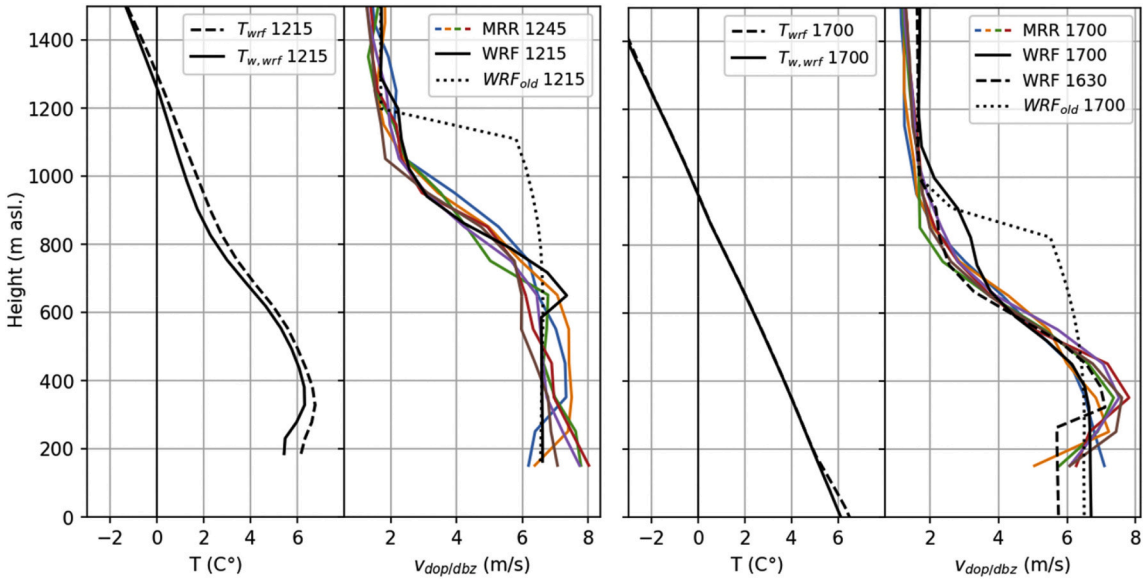

Fig. 9. Vertical profiles of temperature from WRF (black) (left panels of figures), and Doppler velocity (V_{dop}) (MRR, colors) and reflectivity weighted fall velocity (V_{dbz}) (old WRF; dotted black, new WRF; solid black) (right panels of figures) for the specified times (UTC) during 12 Dec. Points in time from WRF are chosen based on based match in precipitation rate. 1630 UTC from WRF is also chosen due to the possible influence of riming at 1700 UTC.

over-predicted by the model (Fig. 11). The post-frontal convective rain showers dominated the rest of the period and are more difficult for the model to predict correctly due to their relatively small horizontal extent. WRF does predict a few such showers at Neilton point, but not necessarily at the right time or magnitude. During most of this period the gauge time series appears quantized. This is most likely due to the short averaging time step used to create this series, causing bounded and clustered errors as described briefly in Chapter 3.1 (see Wang et al., 2008 for more detail). No wind observations are available at the site during the event, but WRF indicates wind speeds in the range 1–5 m s^{-1} mostly associated with the post frontal convective periods, and an increase as the front approached late 19 Dec, with wind speeds up to 10 m s^{-1} midday 20 Dec. A peak in wind speed was also noticed 1700 UTC 21 Dec. Strong winds did most likely influence the measurements and might play a part in the discrepancy between the model, the gauge, and the 2DVD derived rain rates. As the gauge was not wind shielded, the amount collected was most likely lower than the truth. Rain rate derived from the 2DVD is an integral rain parameter calculated based on the measured droplet size distribution, and if these measurements contain errors due to strong winds, the resulting rain rate will also be affected.

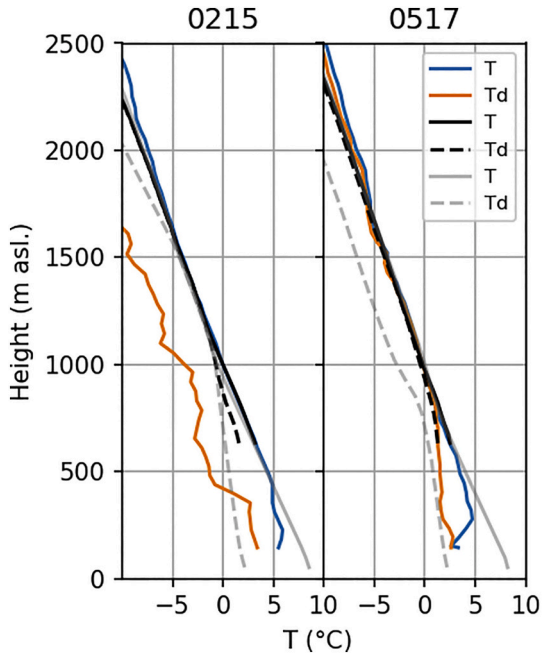

Fig. 10. Soundings of air temperature (T, blue) and dew point temperature (T_d, orange) from the Taholah site launched at two different times (UTC) during 19 December. Simulated air temperature and dew point temperature (dashed) at Tahola are shown in gray, and at Neilton Point in black. (For interpretation of the references to colour in this figure legend, the reader is referred to the web version of this article.)

Excluding the warmer and windy period of the frontal passage, which resulted in mostly rain at ground level at Neilton Point (not shown), and the windy period at the end of 21 Dec, disdrometer data is compared with model results in Fig. 12 for this event. The disdrometer measurements (left) show a bimodal distribution of the diameter – fall speed pairs, following the D – v relations for dry snow and rain, typical for mixed precipitation (Yuter et al., 2006). Particles also occurred in between, indicative of melting snow. Particles which occurred outside are outliers, as described in Kruger and Krajewski (2002), most likely due to droplet splashing or particles crossing the light sheets outside the virtual measuring area. Prior to the frontal passage (top) the 2DVD recorded mostly rain, but do also show dry and melting snow particles. After the frontal passage (bottom) the 2DVD shows an even mixture of rain, wet snow and dry snow, where relatively small particles were most frequent. The model also clearly shows a mixture of rain, snow and melting particles (right). In agreement with the observations, the model displays mostly rain prior to the frontal passage, but a lower frequency of the dry snow. The soundings in Fig. 10 did point to the model being

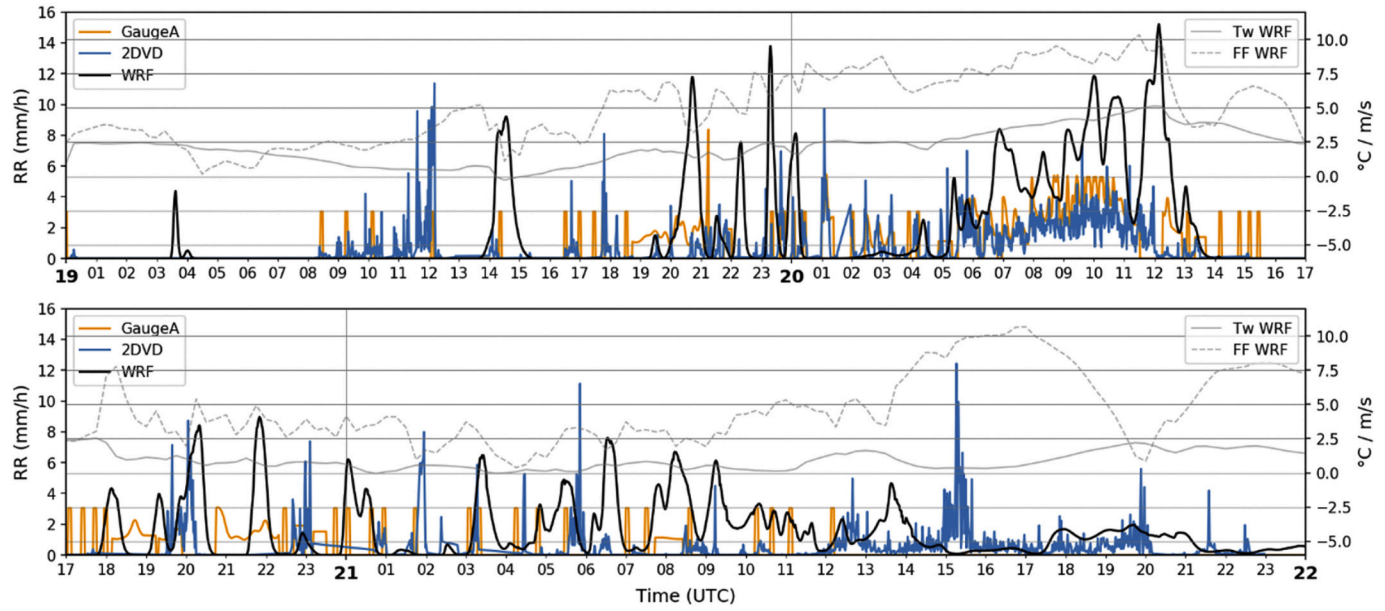

Fig. 11. Precipitation rate (RR) at Neilton Point measured by the rain gauge (orange), derived from the 2DVD (blue) and simulated by WRF (black), and simulated wet bulb temperature (T_w, gray) and wind speed (FF, dashed gray), 19–21 December. (For interpretation of the references to colour in this figure legend, the reader is referred to the web version of this article.)

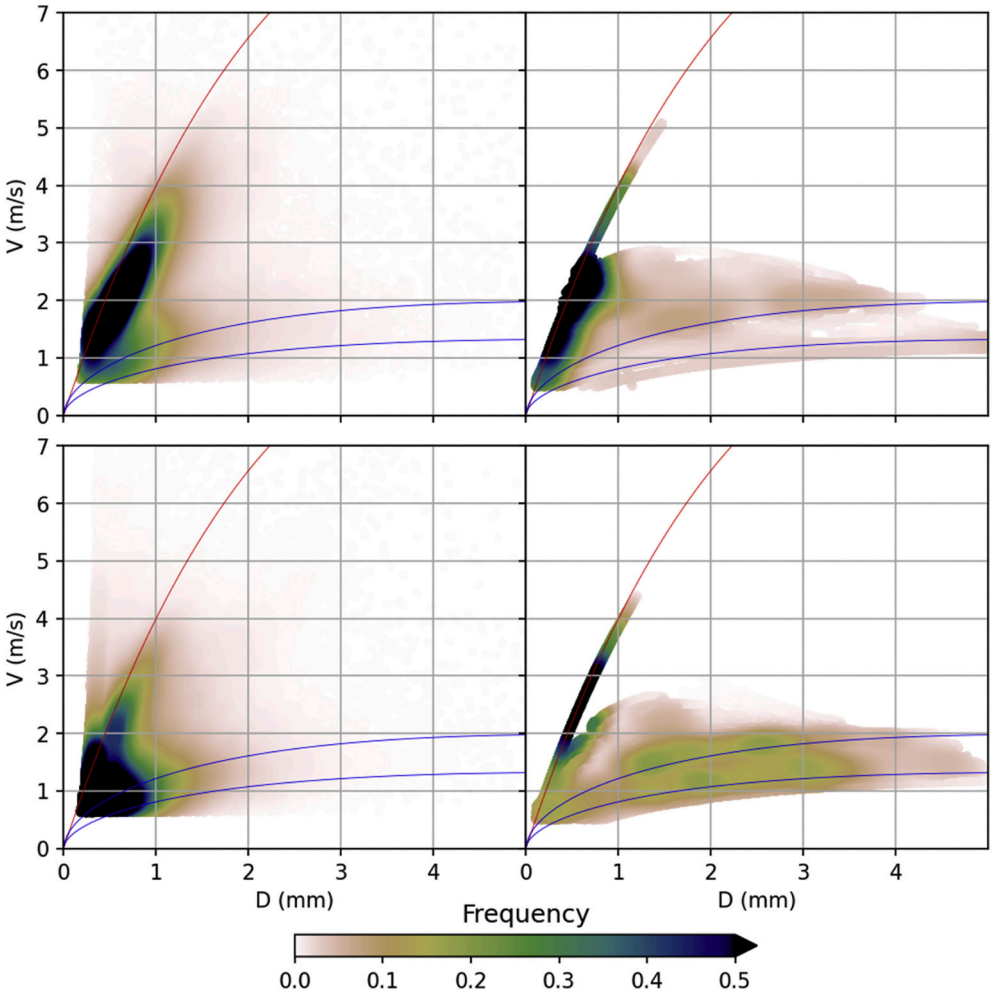

Fig. 12. Precipitation fall velocity (v) and diameter (D) measured by the 2DVD (left) and simulated by WRF (right) at Neilton Point, for 0800 19 Dec – 0500 20 Dec (top, pre-frontal) and 1800 20 Dec – 1400 21 Dec (bottom, post-frontal). The color scale denotes frequency of diameter-velocity pairs. The red line is the fall velocity relation for rain and the lower blue line for dry snow, from (2). The upper blue line is the dry snow velocity relation including a maximum boosting factor (50%) for rimed snow. (For interpretation of the references to colour in this figure legend, the reader is referred to the web version of this article.)

slightly too warm. The model is not as good at replicating the disdrometer pattern of the post-frontal period. Rain is also dominating in this period, but there is also a relatively high frequency of dry and semi-dry snow of larger diameters, in contrast to the observations. As mentioned, small scale convective showers are more difficult for the model to predict well. As there are no observations of temperature available, it might be that model temperature is slightly too cold. Model temperature is close to 0 °C, when strong aggregation takes place (Fabry and Zawadzki, 1995), potentially explaining the large snow particles. The large snow could also be rimed snow, often occurring in such convective cells. Nevertheless, these results show that the model is able to reproduce a melting snow signature seen in disdrometer observations.

4.3. Precipitation accumulation

The change in fall velocity expression impacts the predicted precipitation phase and amount reaching the surface in the model. Fig. 13 reveals a clear trend in the change of accumulated precipitation around the Olympic Mountain (accumulation is for 24 h from 1800 UTC 19 Dec when warmer temperatures persisted. The dashed line shows the upper limit of the zero-degree isotherm at 1245 UTC 20 Dec and how the melting zone moved up and into the northern valley as the warm sector

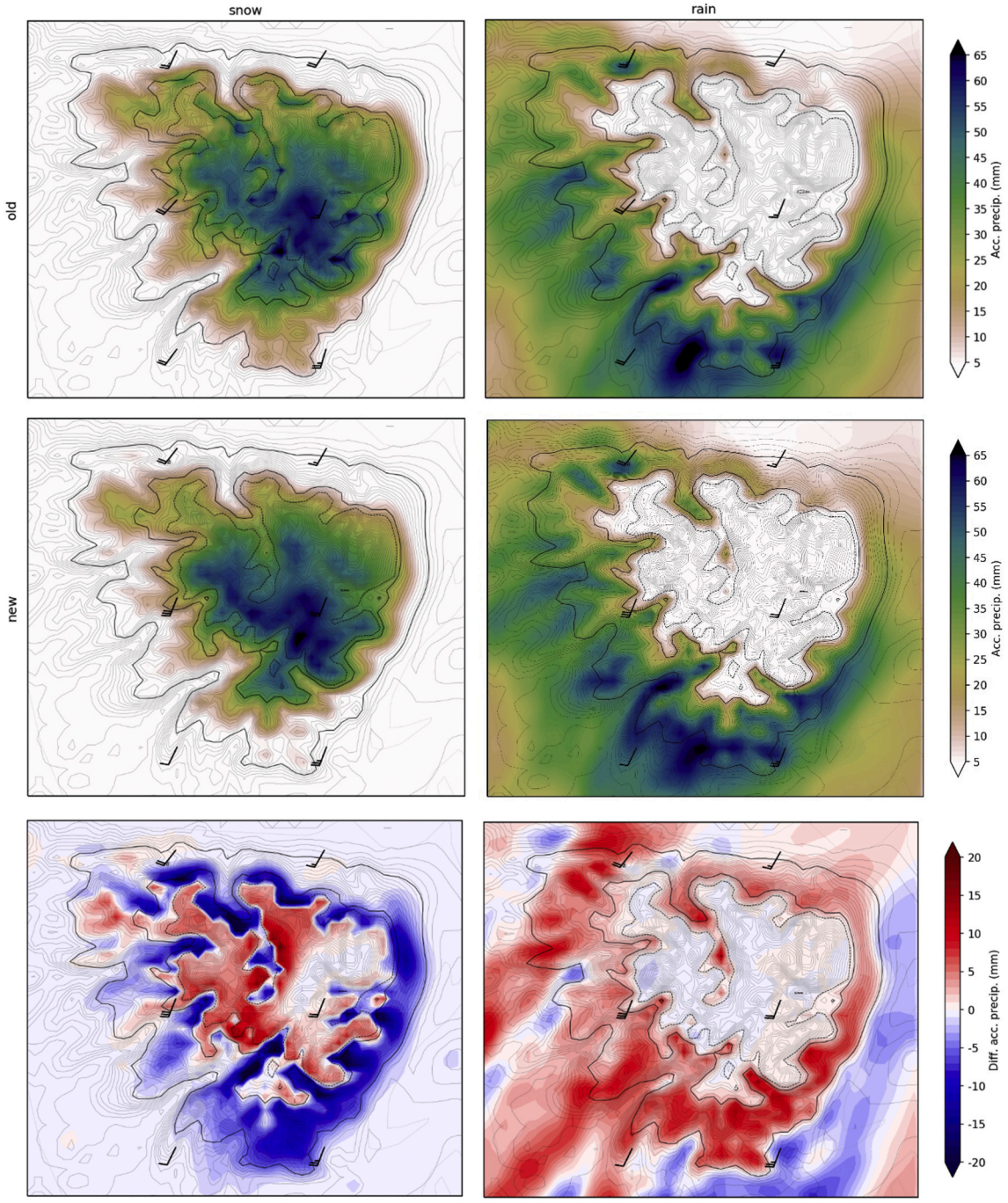

Fig. 13. 24-h accumulated snow (left) and rain (right) using the old (top) and the new (middle) method, and the difference between the new and old methods (bottom), starting 1800 UTC 19 Dec. Solid lines display mean 0 °C (upper) and 3 °C (lower) isotherms, the dashed line the upper limit of the 0 °C isotherm, and wind barbs prevailing wind direction, during the 24 h.

passed). Using the new method, snow accumulation decreases and rain accumulation increases within the melting zone (bottom). At higher elevations where negative temperatures persisted through the period, snow increases. Wind direction during the period was relatively steady from southwest, and it is evident how snow accumulates in lee side terrain within the melting zone using the old method, and for some grid points concentrated as bulls' eyes, as was also noted by Colle et al. (2005) (top right). These bulls' eyes are no longer present using the new method (middle right), resulting in a large negative difference in snow accumulation in these areas (more than −20 mm water equivalent over 24 h; roughly a 30–45% reduction). As was evident in the vertical profiles in Fig. 9, snow fall speed increases instantly after crossing the melting level and falls too fast through the layer with the old method. In lee side terrain, where there typically is a relatively high flux of dry snow crossing the 0° isotherm, this results in unrealistically large snow accumulations. The bull's eyes are likely caused by specific grid points obtaining the optimal conditions most often through the 24 h, which are right downstream of the melting level in lee side terrain. They move in space and time due to changing temperature and wind direction and are unphysical in nature. This is improved with the new method, where snow now has a realistic fall velocity through the melting layer. Slower falling velocity means that the snow spends a longer time within the melting layer, causing more of the precipitation to melt completely and hence reach the ground as rain instead of snow (partly explaining the decrease in snow and increase in rain within the melting zone). Slower falling velocity also means more time for horizontal advection to transport the snow away from these areas, and in this case into higher terrain, close to the 0° isotherm (where there is an increase of up to 20 mm snow water equivalent (up to 60%) over the 24 h in some areas). Unfortunately, getting highly detailed and accurate snow measurements in such challenging terrain under such wind conditions is nearly impossible. Perhaps only post snowstorm remotely sensed (from aircraft) snow depth measurements could help validate this model outcome.

5. Conclusions

This study presents improvements to the Thompson-Eidhammer microphysics scheme, part of the Weather Research and Forecast (WRF) model, regarding the representation of melting of snow. In reality, as snow is melting, the meltwater sticks to the snowflake so it becomes a mixture of ice and liquid water. Laboratory experiments have shown that the fall speed is a function of the liquid fraction, as well as the initial diameter of the dry snowflake. In the model, the melted water mass is immediately shed into the rain category, resulting in underrepresented snow sizes. Previously this led to underpredicted snow fall velocities, and to compensate for this, the velocity in the melting layer was equaled to the maximum of the rain and snow velocity at the given model level.

Here, a physically based expression for melting particle fall velocity as function of snowflake melted fraction is implemented, where the melted fraction is approximated by the liquid precipitation mass ratio at the given model level. Also, improvements relate to the consistent use of wet-bulb temperature in various process rates and definition of melting level. Two events of frontal passages observed during Dec 2015 by the Olympic Mountain Experiment (OLYMPEX) are used to compare with the WRF model. The results are summarized as follows:

- The modified scheme is able to represent disdrometer (2DVD) observations of joint particle size and fall velocity during wet snow events, with a typical bimodal distribution.
- Particle fall velocity profiles through the melting layer derived from a vertically pointing radar (MRR) are well replicated by the model, and show a non-linear increase in fall velocity as snow is melting through the layer, in agreement with Mitra et al. (1990). The old scheme predicted too fast falling snow through the melting layer.
- The modified scheme shows a reduction in snow and an increase in rain accumulation in the melting zone around Olympic Mountain as a result of slower falling snow during melting. Snow accumulation is particularly decreased in lee side areas, where the old scheme showed significant and unphysical accumulation due to too fast falling velocities. This should result in better predictions of precipitation phase and amount reaching the surface.

The lee-side snow overprediction problem has been noted by previous authors (Colle et al., 2005), and this research suggests a rather simple and physically based solution to remove the so-called 'bull's eyes' of spurious lee-side snow accumulation within the melting zone. This study demonstrates the better representation of melting snow fall velocity, and presents the significant differences this exerts on accumulated precipitation, but a validation of predicted ground precipitation phase and amount using precipitation measurements unaffected by wind is still needed. As a melting layer can also exist above a re-freezing layer, these results will also affect the prediction of ice pellets and freezing rain.

Data availability

Observational data from the OLYMPEX campaign is available through three different access options here: https://ghrc.nsstc.nasa.gov/home/field-campaigns/olympex/data_access. The code modifications to the Thompson-Eidhammer scheme will be part of an official WRF version in a future release.

Declaration of Competing Interest

The authors declare that they have no known competing financial interests or personal relationships that could have appeared to influence the work reported in this paper.

Acknowledgments

The authors would like to thank The Norwegian Research Council and Statnett (the Norwegian transmission line grid operator) for funding this work, including the corresponding author's (E.C.I.) doctorate degree, through the research project ICEBOX. E.C.I. would also like to thank her main supervisor at the University of Oslo, Dr. Trude Storelvmo, for following up research progress. The authors are grateful for the readily available and well documented observational data from the OLYMPEX campaign provided by the University of Washington and NASA.

Appendix A. Appendix

Comparison of simulated and observed variables from the Fishery site 13 December is shown in Fig. A.1. The MRR signal prior to 1230 and after 2030 UTC is of less interest due to scattered and short-lived showers which are hard to distinguish from the noise, and therefore the comparison is limited to the time window shown. Available soundings from the Tahola site are compared with temperature profiles from WRF at Fishery in Fig. A.2.

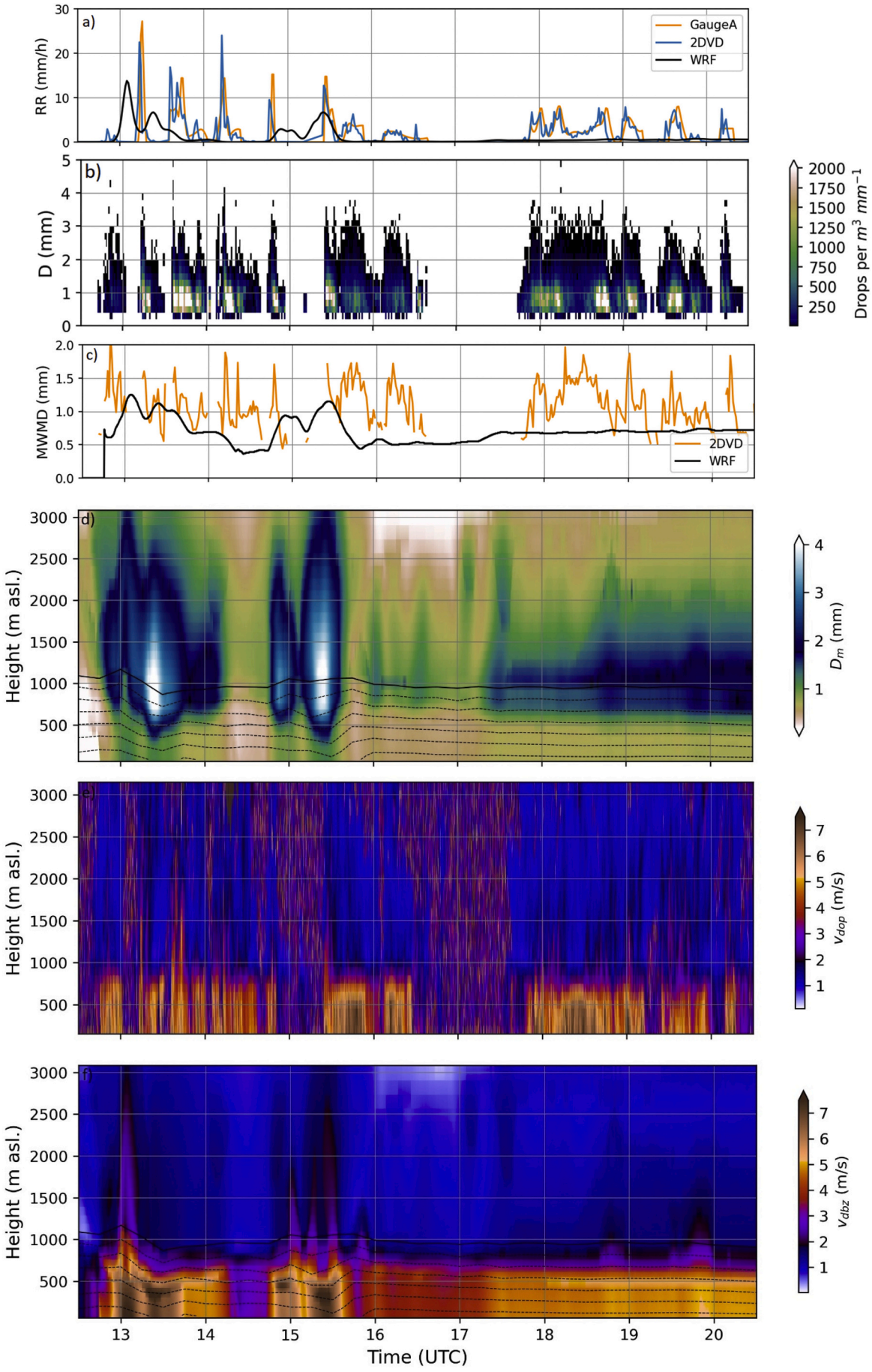

(caption on next page)

Fig. A.1. Observed and simulated variables during 1230–2030 UTC 13 Dec at Fishery. a) Precipitation rate (RR) measured by the rain gauge (orange), derived from the 2DVD (blue) and simulated by WRF (black). b) Droplet size distribution from 2DVD, colors display number of drops per m3 mm-1. c) Mass weighted mean diameter (MWMD) from 2DVD and WRF (model level 1). d) Time – height plot of particle size (D_m, see (19)) from the model. e) Time – height plot of Doppler velocity (V_{dop}) from MRR. f) Time – height plot of reflectivity weighted fall velocity (V_{dbz}) from the model, derived through the methodology outlined in Section 3.4. Black lines are wet bulb temp. starting at 0 °C (solid) increasing in intervals of 1 °C. (For interpretation of the references to color in this figure legend, the reader is referred to the web version of this article.)

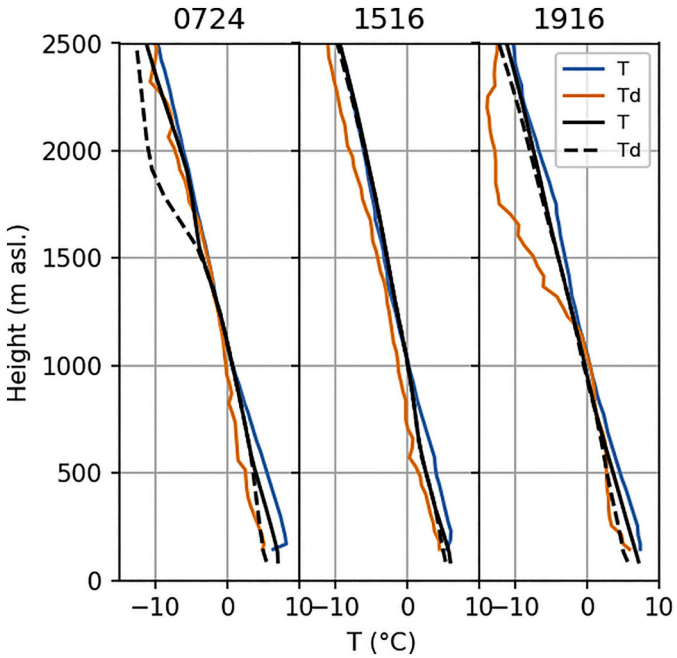

Fig. A2. Soundings of air temperature (T, blue) and dew point temperature (Td, orange) from the Taholah site launched at three different times (UTC) during 13 Dec. Simulated air temperature and dew point temperature (dashed) in black from the Fishery site. (For interpretation of the references to color in this figure legend, the reader is referred to the web version of this article.)SoSSS

References

Brown, B.R., Bell, M.M., Thompson, G., 2017. Improvements to the snow melting process in a partially double moment microphysics parameterization. J. Adv. Model. Earth Syst. 9, 1150–1166.

Cholette, M., Morrison, H., Milbrandt, J.A., Thériault, J.M., 2019. Parameterization of the bulk liquid fraction on mixed-phase particles in the predicted particle properties (P3) scheme: description and idealized simulations. J. Atmos. Sci. 76, 561–582.

Colle, B.A., Mass, C.F., 2000. The 5–9 February 1996 flooding event over the Pacific Northwest: Sensitivity studies and evaluation of the MM5 precipitation forecasts. Mon. Weather Rev. 128, 593–617.

Colle, B.A., Zeng, Y., 2004. Bulk microphysical sensitivities and pathways within the MM5 for orographic precipitation. Part I: the Sierra 1986 event. Mon. Weather Rev. 132, 2780–2801.

Colle, B.A., Garvert, M.F., Wolfe, J.B., Mass, C.F., 2005. The 13–14 December 2001 IMPROVE-2 event. Part III: Simulated microphysical budgets and sensitivity studies. J. Atmos. Sci. 62, 3535–3558.

Ding, B., Yang, K., Qin, J., Wang, L., Chen, Y., He, X., 2014. The dependence of precipitation types on surface elevation and meteorological conditions and its parameterization. J. Hydrol. 513, 154–163.

Doms, G., Schättler, U., 2002. A description of the nonhydrostatic regional model LM—Part I: Dynamics and numerics. Deutscher Wetterdienst Tech. Rep. 134.

Fabry, F., Szyrmer, W., 1999. Modeling of the Melting Layer. Part II: Electromagnetic. J. Atmos. Sci. 56, 3593–3600.

Fabry, F., Zawadzki, I., 1995. Long-term radar observations of the melting layer of precipitation and their interpretation. J. Atmos. Sci. 52, 838–851.

Ferrier, B.S., 1994. A double-moment multiple-phase four-class bulk ice scheme. Part I: Description. J. Atmos. Sci. 51, 249–280.

Frick, C., Seifert, A., Wernli, H., 2013. A bulk parametrization of melting snowflakes with explicit liquid water fraction for the COSMO model. Geosci. Model Dev. 6, 1925–1939.

Fujioshi, Y., 1986. Melting snow flakes. J. Atmos. Sci. 43, 307–311.

Gedzelman, S.D., Arnold, R., 1993. The form of cyclonic precipitation and its thermal impact. Mon. Weather Rev. 121, 1957–1978.

Han, M., Braun, S.A., Matsui, T., Williams, C.R., 2013. Evaluation of cloud microphysics schemes in simulations of a winter storm using radar and radiometer measurements. J. Geophys. Res. Atmos. 118, 1401–1419.

Harder, P., Pomeroy, J., 2013. Estimating precipitation phase using a psychrometric energy balance method. Hydrol. Process. 27, 1901–1914.

Houze, R.A., McMurdie, L.A., Peterson, W.A., Schwaller, M.R., Baccus, W., Lundquist, J. D., Mass, C.F., Nijssen, B., Rutledge, S.A., Hudak, D.R., Tanelli, S., Mace, G.G., Poellot, M.R., Lettenmaier, D.P., Zagrodnik, J.P., Rowe, A.K., DeHart, J.C., Madaus, L.E., Barnes, H.C., Chandrasekar, V., 2017. The olympic mountains experiment (OLYMPEX). Bull. Amer. Meteor. Soc. 98, 2167–2188.

Iacono, M.J., Delamere, J.S., Mlawer, E.J., Shephard, M.W., Clough, S.A., Collins, W.D., 2008. Radiative forcing by long-lived greenhouse gases: Calculations with the AER radiative transfer models. J. Geophys. Res. 113, D13103.

Knight, C.A., 1979. Observations of the morphology of melting snow. J. Atmos. Sci. 36, 1123–1130.

Kruger, A., Krajewski, W.F., 2002. Two-dimensional video disdrometer: a description. J. Atmos. Ocean. Technol. 19, 602–617.

Langleben, M.P., 1954. The terminal velocity of snowflakes. Quart. J. Roy. Meteor. Soc. 80, 174–181.

Locatelli, J.D., Hobbs, P.V., 1974. Fall speeds and masses of solid precipitation particles. J. Geophys. Res. 79, 2185–2197.

Makkonen, L., 1989. Estimation of wet snow accreation on structures. Cold Reg. Sci. Technol. 17, 83–88.

Marks, D., Domingo, J., Susong, D., Link, T., Garen, D., 1999. A spatially distributed energy balance snowmelt model for application in mountain basins. Hydrol. Process. 13, 1935–1959.

Matsuo, T., Sasyo, Y., 1981a. Empirical formula for the melting rates of snow flakes. J. Meteor. Soc. Japan 59, 1–8.

Matsuo, T., Sasyo, Y., 1981b. Melting of snowflakes below freezing level in the atmosphere. J. Meteorol. Soc. Jpn. 59 (1), 10–24.

McNamara, J.P., 2017. Rain or snow: hydrologic processes, observations, prediction, and research needs. Hydrol. Earth Syst. Sci. 21 (1), 1–22.

Milbrandt, J.A., Morrison, H., 2016. Parameterization of cloud microphysics based on the prediction of bulk ice particle properties. Part III: Introduction of multiple free categories. J. Atmos. Sci. 73, 975–995.

Milbrandt, J.A., Yau, M.K., 2005. A multi-moment bulk microphysics parameterization. Part II: A proposed three-moment closure and scheme description. J. Atmos. Sci. 62, 3065–3081.

Milbrandt, J.A., Glazer, A., Jacob, D., 2012. Predicting the snow-to-liquid ratio of surface precipitation using a bulk microphysics scheme. Mon. Weather Rev. 140, 2461–2476.

Mitchell, K., 2005. NCAR: Unified Noah LSM. https://ral.ucar.edu/sites/default/files/public/product-tool/unified-noah-lsm/Noah_LSM_USERGUIDE_2.7.1.pdf (accessed 12 February 2020).

Mitra, S.K., Vohl, O., Ahr, M., Pruppacher, H.R., 1990. A wind tunnel and theoretical study of the melting behavior of atmospheric ice particles. IV: Experiment and theory for snow flakes. J. Atmos. Sci. 47, 584–591.

Molthan, A.L., Colle, B.A., Yuter, S.E., Stark, D., 2016. Comparisons of modeled and observed reflectivities and fall speeds for snowfall of varied riming degrees during winter storms on Long Island, New York. Mon. Weather Rev. 144, 4327–4347.

Morrison, H., Milbrandt, A., 2015. Parameterization of cloud microphysics based on the prediction of the bulk ice particle properties. Part I: Scheme description and idealized tests. J. Atmos. Sci. 72, 287–311.

Nakanishi, M., Niino, H., 2006. An improved Mellor–Yamada Level-3 Model: its numerical stability and application to a regional prediction of advection fog. Boundary-Layer Meteorol. 119 (2), 397–407.

NASA and Uni. Washington, 2020. OLYMPEX: A NASA/GPM Ground Validation Field Campaign in the Pacific Northwest. http://olympex.atmos.washington.edu/.

Nygaard, B., Fikke, S.M., Makkonen, L., 2017. State of the art Report on Designing Transmission Lines for Wet Snow Accumulation, s.l.: CEATI.

Peters, G., Fischer, B., Andersson, T., 2002. Rain observations with a vertically looking Micro rain Radar (MRR). Boreal Environ. Res. 7, 353–362.

Petersen, W., Gatlin, P., 2017. GPM Ground Validation Micro Rain Radar (MRR). Dataset Available Online from the NASA Global Hydrology Resource Center DAAC. Huntsville, Alabama, U.S.A.. https://ghrc.nsstc.nasa.gov/hydro/details/gpmmrrolyx

Petersen, W., David, A., Wolff, B., Wang, J., Tokay, A., 2017b. GPM Ground Validation Met One Rain Gauge Pairs OLYMPEX. Dataset Available Online from the NASA Global Hydrology Resource Center DAAC. Huntsville, Alabama, U.S.A.. https://ghrc.nsstc.nasa.gov/hydro/details/gpmrgnaolyx

Petersen, W.A., Wolff, D.B., Wingo, M., Tokay, A., 2017a. GPM Ground Validation Two-Dimensional Video Disdrometer (2DVD) OLYMPEX. Dataset Available Online from the NASA Global Hydrology Resource Center DAAC. Huntsville, Alabama, U.S.A.. https://ghrc.nsstc.nasa.gov/hydro/details/gpm2dvdolyx (Accessed 11 December 2018).

Pruppacher, H.R., Klett, J.D., 1997. Microphysics of Clouds and Precipitation, 2. ed. Kluwer Academic Publishers, Dordrecht.

Reisner, J., Rasmussen, R.M., Bruintjes, R.T., 1998. Explicitforecasting of supercooled liquid water in winter storms usingthe MM5 mesoscale model. Quart. J. Roy. Meteor. Soc. 124, 1071–1107.

Rutledge, S.A., Hobbs, P., 1983. The mesoscale and microscale structure and organization of clouds and precipitation in midlatitude cyclones. VIII: A model for the "Seeder-Feeder" process in warm-frontal rainbands. J. Atmos. Sci. 40 (5), 1185–1206.

Rutledge, S.A., Young, K., Voemel, H.D., 2018. GPM Ground Validation Upper Air Radiosonde OLYMPEX. Dataset Available Online from the NASA Global Hydrology Resource Center DAAC. Huntsville, Alabama, U.S.A.. https://ghrc.nsstc.nasa.gov/hydro/details/gpmsondeolyx

Sekhon, R.S., Srivastava, R.C., 1971. Doppler radar observations of drop-size distributions in a thunderstorm. J. Atmos. Sci. 28, 983–994.

Skofronick-Jackson, G., Hudak, D., Petersen, W., Nesbitt, S.W., Chandrasekar, V., Durden, S., Gleicher, K.J., Huang, G., Joe, P., Kollias, P., Reed, K.A., Schwaller, M.R., Stewart, R., Tanelli, S., Tokay, A., Wang, J.R., Wolde, M., 2015. Global precipitation measurement cold season precipitation experiment (GCPEX): for measurement's sake, let it snow. Bull. Amer.Meteor. 96, 1719–1741.

Srivastava, R.C., Coen, J.L., 1992. New explicit equations for the accurate calculation of the growth and evaporation of hydrometeors by the diffusion of water vapor. J. Atmos. Sci. 47 (17), 1643–1651.

Szyrmer, W., Zawadzki, I., 1999. Modeling of the melting layer. Part I: Dynamics and microphysics. J. Atmos.Sci. 56, 3573–3592.

Thériault, J.M., Stewart, R.E., 2010. A parameterization of the microphysical processes forming many types of winter precipitation. J. Atmos. Sci. 67, 1492–1508.

Thériault, J.M., Stewart, R.E., Henson, W., 2012. Impacts of terminal velocity on the trajectory of winter precipitation types. Atmos. Res. 116, 116–129.

Thompson, G., Eidhammer, T., 2014. A study of aerosol impacts on clouds and precipitation development in a large winter cyclone. J. Atmos. Sci. 71, 3636–3658.

Thompson, G., Rasmussen, R.M., Manning, K., 2004. Explicit forecasts of winter precipitation using an improved bulk microphysics scheme. Part I: Description and sensitivity analysis. Mon. Weather Rev. 132, 519–542.

Thompson, G., Field, P.R., Rasmussen, R.M., Hall, W.D., 2008. Explicit forecasts of winter precipitation using an improved bulk microphysics scheme. Part II: Implementation of a new snow parameterization. Mon. Weather Rev. 136, 5095–5115.

Tokay, A., Kruger, A., Krajewski, W.F., 2001. Comparison of drop size distribution measurements by impact and optical disdrometers. J. Appl. Meteorol. 40, 2083–2097.

Tridon, F., Van Baelen, J., Pointin, Y., 2011. Aliasing in Micro rain Radar data due to strong vertical winds. Geophys. Res. Lett. 38.

Wang, J., Fisher, B.L., Wolff, D.B., 2008. Estimating rain rates from tippingbucket rain gauge measurements. J. Atmos. Ocean. Technol. 25, 43–56.

Yuter, S.E., Kingsmill, D.E., Nance, L.B., Löffler-Mang, M., 2006. Observations of precipitation size and fall speed characteristics within coexisting. J. Appl. Meteorol. Climatol. 45, 1450–1464.